Constrained Trajectory Optimization of a Soft Lunar Landing from a Parking Orbit

by

Alisa Michelle Hawkins

B.S., Georgia Institute of Technology (2003)

Submitted to the Department of Aeronautics and Astronautics
in partial fulfillment of the requirements for the degree of
Master of Science in Aeronautics and Astronautics
at the
MASSACHUSETTS INSTITUTE OF TECHNOLOGY
June 2005

Author: _____
Department of Aeronautics and Astronautics
May 20, 2005

Certified by: _____
Thomas J. Fill
Principle Member of the Technical Staff, Draper Laboratory
Thesis Supervisor

Certified by: _____
Ronald J. Proulx
Principle Member of the Technical Staff, Draper Laboratory
Thesis Supervisor

Certified by: _____
Eric M. Feron
Associate Professor of Aeronautics and Astronautics, M.I.T.
Thesis Supervisor

Accepted by: _____
Jaime Peraire
Professor of Aeronautics and Astronautics, M.I.T.
Chair, Committee on Graduate Students

[This page intentionally left blank.]

Constrained Trajectory Optimization of a Soft Lunar Landing from a Parking Orbit

by

Alisa Michelle Hawkins

Submitted to the Department of Aeronautics and Astronautics
on May 20, 2005, in partial fulfillment of the
requirements for the degree of
Master of Science in Aeronautics and Astronautics

Abstract

A trajectory optimization study for a soft landing on the Moon, which analyzed the effects of adding operationally based constraints on the behavior of the minimum fuel trajectory, has been completed. Metrics of trajectory evaluation included fuel expenditure, terminal attitude, thrust histories, etc.. The vehicle was initialized in a circular parking orbit and the trajectory divided into three distinct phases: de-orbit, descent, and braking. Analysis was initially performed with two-dimensional translational motion, and the minimally constrained optimal trajectory was found to be operationally infeasible. Operational constraints, such as a positive descent orbit perilune height and a vertical terminal velocity, were imposed to obtain a viable trajectory, but the final vehicle attitude and landing approach angle remained largely horizontal. This motivated inclusion of attitude kinematics and constraints to the system. With rotational motion included, the optimal solution was feasible, but the trajectory still had undesirable characteristics. Constraining the throttle to maximum during braking produced a steeper approach, but used the most fuel. The results suggested a terminal vertical descent was a desirable fourth segment of the trajectory, which was imposed by first flying to an offset point and then enforcing a vertical descent, and provided extra safely margin prior to landing. In this research, the relative effects of adding operational constraints were documented and can be used as a baseline study for further detailed trajectory optimization.

Thesis Supervisor: Thomas J. Fill
Title: Principle Member of the Technical Staff, Draper Laboratory

Thesis Supervisor: Ronald J. Proulx
Title: Principle Member of the Technical Staff, Draper Laboratory

Thesis Supervisor: Eric M. Feron
Title: Associate Professor of Aeronautics and Astronautics, M.I.T.

[This page intentionally left blank.]

Acknowledgments

During my time at MIT and Draper Laboratory, I have worked with some amazing people who have helped me grow, on both intellectual and personal levels. This work would not have been possible if not for the guidance and support of Thomas Fill and Ronald Proulx, who gave freely of their time to support this research. Tom, thank you for your never-ending support, patience, attention to detail, and amazing wealth of knowledge. I have learned a great deal from you, which I hope to carry with me in my professional career. Ron, thank you for your vision and for always pushing the project forward. I admire your passion and dedication. Much gratitude is given to Eric Feron for being a constant source of enthusiasm and for having a desire to think out-of-the-box. I also would like to thank David Geller, Michael Luniewicz, Linda Fuhrman, and Lee Norris whom I had the pleasure of working with for brief periods of time, and Michael Ross for providing insight into your DIDO package. Special thanks to Anil Rao and Peter Neirinckx for checking in on me from time to time. I would also like to thank the Draper library staff for ordering an endless stream of literature for me. Rachel, thanks for being a great officemate. And special thanks to the roommates of 268 Broadway: Geoff, Megan, and Steve. Above all, I would like to thank my family, who's love and support has gotten me to where I am today. And to Noël, my love, thank you for everything. This adventure would not have been complete without you. Thank you for sharing this experience with me.

This thesis is dedicated to my grandparents:

Roland P. and Odette M. Jotterand & Joseph F. and Sophronia V. Hawkins, Sr.

This thesis was prepared at the Charles Stark Draper Laboratory, Inc., under Internal Research and Development Project 12601-001, GCDLF Support.

Publication of this thesis does not constitute approval by Draper or the sponsoring agency of the findings or conclusions contained herein. It is published for the exchange and stimulation of ideas.

Alisa M. Hawkins

[This page intentionally left blank.]

Contents

List of Figures

[This page intentionally left blank.]

List of Tables

[This page intentionally left blank.]

Chapter 1

Introduction

Trajectory design is a crucial process during the planning phase of a spacecraft landing mission. The trajectory must meet all mission objectives, while complying with vehicle limitations and capabilities. The common approach to designing a spacecraft landing trajectory is to first focus on the translational motion, while treating the vehicle as a point mass. Trajectory planners concentrate on the overall shape of the trajectory before attitude dynamics are considered. Once a trajectory is determined, guidance algorithms are created to guide the vehicle along the given trajectory. Because fuel mass is a major driver of the total vehicle mass, and thus mission cost, the objective of most guidance algorithms is to minimize the required fuel consumption. Most of the existing algorithms are termed as "near-optimal" in terms of fuel expenditure.

The question arises as to how close to optimal are these guidance algorithms. To answer this question, numerical trajectory optimization techniques are often required. One such technique is applied in the current research to find these minimum fuel optimal trajectories. In most cases, attitude dynamics are not considered in exploring these "minimum fuel" trajectories. The contribution of this thesis is to included attitude dynamics in the optimization problem and assess the effect of these dynamics on the optimal trajectory.

Recently, renewed interest in returning to the lunar surface has been expressed[1]. The

[1] "The Vision for Space Exploration", NASA, February 2004, http://www.nasa.gov/missions/solarsystem/explore_main.html

Moon has been proposed as a base for extended missions. During a landing on the Moon, there is no atmospheric drag to slow the vehicle from orbital velocities to near-zero at the surface. Instead, an onboard propulsion system is required for this purpose. The vehicle must be capable of sensing the surface and landing at an attitude which places all landing gears simultaneously and squarely on the ground. This thesis considers the optimal fuel requirements to efficiently satisfy the trajectory and attitude requirements simultaneously in the landing problem.

1.1 Review of Previous Work

Previous work that relates to the current research falls into the two categories of guidance algorithms and trajectory optimization for lunar landings. A guidance algorithm is used to fly the vehicle during the actual mission. Trajectory optimization techniques are used to verify that the guidance algorithms produce the most efficient or near-efficient trajectories for the vehicle to follow. Previous work performed in these areas are presented next.

The race for the Moon in the 1960's generated a large impetus for the research and development of guidance algorithms for the soft landing of vehicles on the lunar surface. The majority of lunar landing research was performed during the Apollo era in the 1960's. Studies were performed to develop guidance algorithms, descent trajectories, transfer orbit properties, etc.. These studies included a detailed parametric study by Akridge and Harlin [1], who varied parameters such as initial parking orbit altitudes, thrust-to-weight ratio, and the specific impulse of the engine. A study of lunar landing orbits was performed by Cavoti [2] for both range-free and range-fixed problems, with the assumption of a two impulse burn. This study theoretically showed that the minimum-fuel descent transfer orbit could not be an exact Hohmann type orbit (tangential thrusting at apolune and perilune) and meet the terminal vertical attitude constraints. Cavoti found that the solution was to burn at a slight angle to the tangential direction. Trajectory analysis work, done by Bennett and Price [3], was the basis for dividing the powered descent phase of the Apollo landing trajectory into three phases: an fuel-optimum braking phase, a landing approach transition phase, and a terminal descent phase.

Existing guidance algorithms, which were vigorously tested, landed five Surveyor vehicles and six Apollo lunar modules successfully on the surface of the Moon. The Surveyor vehicles used a guidance scheme based on the work done by Cheng and Pfeffer [4], which controlled the velocity and slant range of the vehicle during the final descent. The attitude control law used is known as a "gravity turn" [5], which tended to force the flight path towards the vertical as time progressed. The Apollo missions used an explicit guidance algorithm, which was originally derived by Cherry [6] and then simplified by Klumpp [7] to be used onboard the lunar module guidance computer.

Several other guidance algorithms were proposed during the same time period. A proportional navigational guidance algorithm was proposed by Hall, Dietrich, and Tiernan [8], which was modified from work done by Kriegsman and Reiss [9]. More recently (in 1999), a near-minimum fuel law was proposed by Ueno and Yamaguchi [10].

Most of the aforementioned guidance algorithms were designed to minimize fuel, while minding safety and operational considerations. Optimality, or near-optimality, can only be proven for some of these algorithms given certain assumptions, such as constant thrust or constant gravity. To prove optimality, trajectory optimization and optimal control theory must be used. Trajectory optimization capabilities during the Apollo era were severely limited by computing power. An analytic solution for the one-dimensional vertical terminal descent of a lunar soft-landing, based on an application of Pontryagin's minimum principle, was found by Meditch [11] in 1964. Meditch showed the existence of an optimum thrust program that achieves soft landing under powered descent, which includes the real-time calculation of a switching function as the vehicle descends to the surface. Extensive numerical research on the one-dimensional problem was performed by Teng and Kumar [12], using various cost functionals. Their method is based on a time transformation, applied to the calculus of variations. The solution was found numerically, using a quasi-linearization method. In 1971, Shi and Eckstein [13] derived an exact analytic solution for the problem which Teng and Kumar addressed.

With the increase in computing power, trajectory optimization techniques, of the type to be discussed in Section 2.2, have greatly increased the feasibility of generating optimal trajectories with higher complexity and applicability. Recently, Vasile and Floberghagen

[14] applied a Spectral Elements in Time (SET) approach to the lunar soft-landing problem. Within the work, a lunar landing descent from three parking orbit scenarios down to an altitude of 2 m above the surface was optimized. The cost function used was based on the square of the control input, which has been noted to be different from the minimum fuel solution [15] used in the current research. In the section to follow, the approach for the trajectory optimization followed in the current research is outlined.

1.2 Thesis Overview

This thesis investigates the problem of soft-landing a vehicle on the surface of the Moon from an initial circular parking orbit, using a trajectory optimization technique. The objectives of the current research are to:

1. Determine operationally feasible landing trajectories, which minimize fuel expenditure, while considering the finite rotational motion of the vehicle and operational attitude constraints.

2. Analyze the fuel usage penalties and trajectory performance effects due to the inclusion of each operational constraint considered. Metrics of trajectory performance include terminal attitude, terminal velocity, control histories, steepness of approach to the landing site, etc..

The optimization method used to explore the Moon landing problem in the current research is the Legendre Pseudospectral Method. The Legendre Pseudospectral Method has been applied to a variety of trajectory optimization problems, including problems of ascent guidance [16], satellite formation flying [17], and impulsive orbit transfers [18]. DIDO [19] is used to implement the Legendre Pseudospectral Method in the current research. The entire trajectory, from de-orbit to soft landing, is included in the analysis and is treated as a single problem. This is done in order to generate a trajectory which is optimal over the entire time span of the landing process.

In considering both translational and rotational motion in the trajectory optimization of a soft-landing on the Moon, a direct comparison is made between results that include

rotational motion and those that do not, to gain insight into the effect on the fuel usage. The inclusion of the attitude dynamics in the optimization framework to see how the trajectory is reshaped by the attitude constraints is a major contribution of the current research. An outline of the thesis is given below.

First, an overview of basic optimization theory is given in Chapter 2, along with the numerical methods currently used in solving optimal control problems. The numerical method used in the current research, the Legendre Pseudospectral Method, is discussed and a simple example is presented to explain the implementation of the method.

Chapter 3 outlines the specifics of the landing problem. The coordinate frames used, and assumptions made, are discussed. An overview of the trajectory is given, as well as the assumed vehicle parameters. Operational requirements for a successful landing on the lunar surface are discussed.

The equations of motion are derived in Chapter 4. Full six degree-of-freedom (DOF) equations of motion (EOM) are derived in cartesian coordinates. Vehicle motion is assumed to be planar in the current research (though it can easily be extended to three dimensions) and the 6DOF EOM are reduced to this simplified case. The planar EOM are implemented in the optimization code.

The results obtained from trajectory optimization of the Moon Landing problem are presented in Chapter 5. A baseline trajectory is presented first, before progressing to more constrained scenarios (based on operational considerations). Results obtained for two-dimensional translational motion (TM) are explored first. Selected operational considerations related to the perilune height of the descent orbit, continuous thrusting, and a near-zero terminal velocity are implemented. The effects of these constraints on the trajectory are investigated. Next, the attitude dynamics are added to the optimization framework. Finally, a vertical descent phase is added to the trajectory and analyzed. The significant findings and a conclusion are given in Chapter 6, as well as avenues of future work.

1.3 Nomenclature

Standard nomenclature, defined below for an arbitrary variable (x), has been used throughout this document.

1. $\{x\}$: Regular characters represent scalar quantities or magnitudes of the corresponding vector.

2. $\{\mathbf{x}\}$: Bold, lower case characters represent vectors.

3. $\{\mathbf{X}\}$: Bold, upper case characters represent matrices.

4. $\{\dot{x}\}$: Overhead dots represent the time derivative of the variable.

5. $\{\mathbf{x}^i, \mathbf{x}^b, \mathbf{x}^r\}$: Superscripts denote the reference frame in which a vector is defined, where i, b, and r represent inertial, body, and rotating frames, respectively.

Chapter 2

Optimization Background

The objective of this chapter is to highlight key concepts necessary to understand the optimization analysis performed in subsequent chapters. The reader is referred to the following references for in depth coverage of the corresponding fields: Nonlinear programming ([20]), Optimal Control Theory ([21], [22]), and the Legendre Pseudospectral Method ([23]). A summary of trajectory optimization as a whole, including the first two topics mentioned above, is given by Betts [24].

The first section in this chapter is an overview of optimization theory, while the second describes numerical methods used for solving optimal control problems.

2.1 Basic Optimization

An optimization problem is any problem where it is desired to maximize (or minimize) a specified criterion. This criterion is referred to as a cost function, which is a function of the parameters over which the optimization takes place.

Let $\mathbf{x} \in \mathbb{R}^n$ be a vector of parameters and let $\mathcal{J}(\mathbf{x}) : \mathbb{R}^n \rightarrow \mathbb{R}$ define a cost function. It is desired to find the value $\mathbf{x}^*$ which minimizes $\mathcal{J}$ out of all admissible $\mathbf{x}$. The global minimum is defined as:

$$\mathcal{J}(\mathbf{x}^*) \leq \mathcal{J}(\mathbf{x}) \text{ for all admissible } \mathbf{x} \tag{2.1}$$

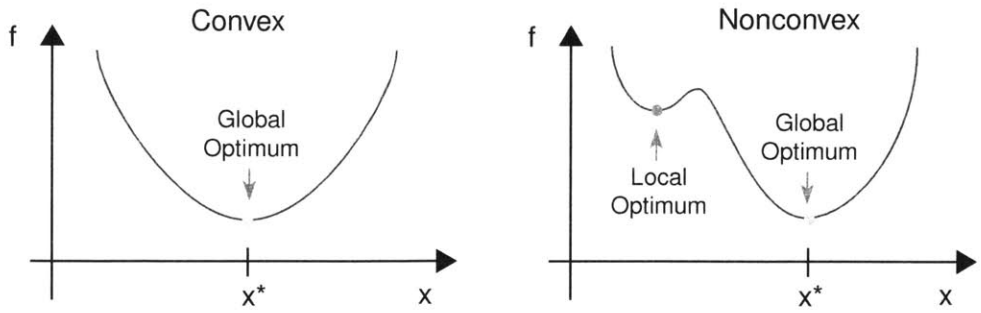

Figure 2-1: One-dimensional Convexity

A local minimum is defined as:

$$\mathcal{J}(\mathbf{x}^*) \leq \mathcal{J}(\mathbf{x}) \quad \text{for all } \mathbf{x} \text{ in the neighborhood of } \mathbf{x}^* \tag{2.2}$$

If a function is globally convex (it monotonically increases in every direction from the global optimum), then any local optimum found is also the global optimum. If the function is nonconvex, finding a local optimum does not necessarily imply that it is also the global optimum solution. The concept of convexity vs. nonconvexity and local vs. global optimums for an arbitrary one-dimensional function $f(x)$ is illustrated in Figure 2-1.

In the convex example, only one optimal solution exists, which is the global optimum. In the nonconvex example, two optimal solutions exist. One is a local optimum, while the other is the global optimum. Most trajectory optimization problems are nonconvex and therefore only local optimums are readily found.

A parameter optimization problem that has a linear cost function, linear constraints, and has only real values is known as a linear programming problem. The term is only used for problems which have real values, otherwise it falls into the category of integer or mixed-integer programming. If the problem has only real values, but includes a nonlinear cost function or nonlinear constraints, it is referred to as a nonlinear programming (NLP) problem.

2.1.1 Finding a Minimum

From basic calculus, recall that a local minimum of a function, which is the function of one variable (*i.e.*, $f(x)$), can be found by locating a point where the first derivative of the function with respect to the variable equals zero and the second derivative is positive.

This notion is expanded to higher dimensions with gradients and Hessians. A gradient is a vector consisting of the first-order partial derivatives of a function with respect to each variable. The Hessian is a matrix consisting of the second-order partial derivatives of the function. For example, the following conditions are satisfied at a local minimum for the cost function $\mathcal{J}(\mathbf{x})$:

$$\frac{\partial \mathcal{J}}{\partial \mathbf{x}} = 0 \tag{2.3}$$

$$\frac{\partial^2 \mathcal{J}}{\partial \mathbf{x}^2} \geq 0 \tag{2.4}$$

One could attempt to determine the minimum of the cost function analytically, but it may be difficult or impossible. Therefore, iterative techniques are used to locate the minimum by searching over the region of admissible $\mathbf{x}$. Newton's method, the most common technique, uses the gradient and Hessian information at the current location to determine a search direction. There are numerous other iterative techniques used, most being based on the principle of Newton's method.

2.1.2 Equality Constrained Optimization

Equality constraints are added to the optimization problem if it is desired that a function, or functions, of the parameters equal a specific value. The parameters can vary, but relationships between the parameters remain fixed. An equality constraint has the form:

$$\mathbf{f}(\mathbf{x}) = \mathbf{0} \tag{2.5}$$

where $\mathbf{f} : \mathbb{R}^n \rightarrow \mathbb{R}^q$.

The most convenient method of solving an equality constrained optimization problem

is to formulate the augmented cost function, which is a combination of the cost function and the constraints with multipliers.

$$\mathcal{J}' = \mathcal{J}(\mathbf{x}) + \boldsymbol{\lambda}^T \mathbf{f}(\mathbf{x}) \tag{2.6}$$

To find the minimum, the gradient of $\mathcal{J}'$ is taken with respect to $\mathbf{x}$ and $\boldsymbol{\lambda}$ and set to zero. The first-order necessary conditions for optimality become:

$$\frac{\partial \mathcal{J}'}{\partial \mathbf{x}} = \frac{\partial \mathcal{J}}{\partial \mathbf{x}} + \frac{\partial \mathbf{f}}{\partial \mathbf{x}} \boldsymbol{\lambda} = 0 \tag{2.7}$$

$$\frac{\partial \mathcal{J}'}{\partial \boldsymbol{\lambda}} = \mathbf{f}(\mathbf{x}) = 0 \tag{2.8}$$

2.1.3 Inequality Constrained Optimization

In addition to equality constraints, some problems have inequality constraints. An inequality constraint has the form:

$$\mathbf{g}(\mathbf{x}) \leq \mathbf{0} \tag{2.9}$$

where $\mathbf{g} : \mathbb{R}^n \rightarrow \mathbb{R}^p$.

The constraints are adjoined to the cost function in a similar manner as the equality constraints, but with the multipliers $\boldsymbol{\mu}$. The augmented cost function is now defined as follows:

$$\mathcal{J}' = \mathcal{J}(\mathbf{x}) + \boldsymbol{\lambda}^T \mathbf{f}(\mathbf{x}) + \boldsymbol{\mu}^T \mathbf{g}(\mathbf{x}) \tag{2.10}$$

There are two classes of inequality constraints that must be dealt with: active and inactive. The vector $\mathbf{g}(\mathbf{x})$ can be written as seen in Equation (2.11), with $g_i(\mathbf{x})$ for $(i = 1...p)$ representing individual components of the p-dimensional vector. An active constraint is when a component of the constraint vector equals zero at the optimum solution, (*i.e.*, $g_i(\mathbf{x}^*) = 0$). The optimization problem is bounded by these constraints. Inactive constraints are constraints where $g_i(\mathbf{x}^*) < 0$ and these constraints do not affect the optimal solution. The equation $\boldsymbol{\mu}^T \mathbf{g} = \mathbf{0}$, which is known as complementary slackness, ensures that the individual inequality constraints are either active or do not affect the solution.

$$\mathbf{g} = \begin{bmatrix} g_1(\mathbf{x}) \\ \vdots \\ g_p(\mathbf{x}) \end{bmatrix} \tag{2.11}$$

The first-order necessary optimality conditions, also known as the Karush-Kuhn-Tucker (KKT) conditions, are given by Equations (2.8) and (2.9), and the following:

$$\frac{\partial \mathcal{J}'}{\partial \mathbf{x}} = 0 \tag{2.12}$$

$$\boldsymbol{\mu} \geq \mathbf{0} \tag{2.13}$$

$$\boldsymbol{\mu}^T \mathbf{g} = \mathbf{0} \tag{2.14}$$

2.1.4 Optimal Control

A special class of optimization problems which include dynamical constraints that vary with time are known as functional optimization problems, where the term "functional" is used to denote a function of a function. Functional optimization problems that have an input, or control, to be determined are known as an optimal control problems. Optimal control problems have a wide variety of applications, including the field of trajectory optimization.

Let $\mathbf{x}(t) \in \mathbb{R}^n$ be the state of a continuous system where $t \in \mathbb{R}$ is time. Furthermore, let $\mathbf{u}(t) \in \mathbb{R}^m$ be the control or input. Lastly, let the dynamical constraints that govern the change of $\mathbf{x}(t)$ with respect to time be given as:

$$\dot{\mathbf{x}} = \mathbf{f}\left(\mathbf{x}(t), \mathbf{u}(t), t\right) \tag{2.15}$$

where $\mathbf{f} : \mathbb{R}^n \times \mathbb{R}^m \times \mathbb{R} \rightarrow \mathbb{R}^n$.

The general optimal control problem is to find the function $\mathbf{u}(t)$ that minimize the cost functional, $\mathcal{J}$, subject to the constraints imposed on the problem (which include the dynamical constraints). It is normally desired to either minimize a functional of the state and control over the entire time span or the final value of a criterion. The cost functional is therefore composed of two parts: a terminal cost $\boldsymbol{\phi} : \mathbb{R}^n \times \mathbb{R} \rightarrow \mathbb{R}$ (commonly referred to

as the Mayer cost) and an integrated cost $\mathcal{L} : \mathbb{R}^n \times \mathbb{R}^m \times \mathbb{R} \rightarrow \mathbb{R}$ (known as the Lagrange cost). The Bolza form of the cost functional, as seen in Equation (2.16), is a combination of the terminal and integrated costs.

$$\mathcal{J} = \boldsymbol{\phi}\left(\mathbf{x}(t_f), t_f\right) + \int_{t_0}^{t_f} \mathcal{L}\left(\mathbf{x}(t), \mathbf{u}(t), t\right)\, dt \tag{2.16}$$

The initial and final boundary conditions that the system must satisfy are given by Equations (2.17) and (2.18), respectively.

$$\boldsymbol{\psi}_0(\mathbf{x}(t_0), t_0) = \mathbf{0} \tag{2.17}$$

$$\boldsymbol{\psi}_f(\mathbf{x}(t_f), t_f) = \mathbf{0} \tag{2.18}$$

where $\boldsymbol{\psi}_0 : \mathbb{R}^n \times \mathbb{R} \rightarrow \mathbb{R}^{q0}$ and $\boldsymbol{\psi}_f : \mathbb{R}^n \times \mathbb{R} \rightarrow \mathbb{R}^{qf}$.

In order to combine all of this information, the augmented cost functional, $\mathcal{J}'$, is formulated. The dynamical and terminal constraints are adjoined to the cost functional with a vector of Lagrange multipliers (also known as the costate), $\boldsymbol{\lambda}(t) \in \mathbb{R}^n$, and the terminal constraint multipliers, $\boldsymbol{\nu} \in \mathbb{R}^{qf}$. The equation given below is similar to Equation (2.3.5) in Reference [22].

$$\begin{aligned}\mathcal{J}' = \boldsymbol{\phi}\left(\mathbf{x}(t_f), t_f\right) + \boldsymbol{\nu}^T \boldsymbol{\psi}\left(\mathbf{x}(t_f), t_f\right) \\ + \int_{t_0}^{t_f} \left[\mathcal{L}\left(\mathbf{x}(t), \mathbf{u}(t), t\right) + \boldsymbol{\lambda}(t)^T \{\mathbf{f}\left(\mathbf{x}(t), \mathbf{u}(t), t\right) - \dot{\mathbf{x}}\}\right]\, dt\end{aligned} \tag{2.19}$$

To simplify the augmented cost functional, the Hamiltonian and end point functionals are defined in Equations (2.20) and (2.21), respectively. $\mathcal{J}'$ is simplified to Equation (2.22). The functional dependencies have been omitted for clarity.

$$\mathcal{H} = \mathcal{L} + \boldsymbol{\lambda}^T \mathbf{f} \tag{2.20}$$

$$\mathcal{G} = \boldsymbol{\phi} + \boldsymbol{\nu}^T \boldsymbol{\psi} \tag{2.21}$$

$$\mathcal{J}' = \mathcal{G} + \int_{t_0}^{t_f} \left[\mathcal{H} - \boldsymbol{\lambda}^T \dot{\mathbf{x}}\right]\, dt \tag{2.22}$$

Calculus of variations is used to determine a stationary point of the augmented cost functional. Using the same concepts as before, the variation of $\mathcal{J}'$ is taken and appropriate functions are set to zero. The resulting necessary conditions for a local minimum for the free final time problem are derived by Hull [21] as:

$$\dot{\mathbf{x}} = \frac{\partial \mathcal{H}}{\partial \boldsymbol{\lambda}} = \mathbf{f}(x, u, t) \tag{2.23}$$

$$\dot{\boldsymbol{\lambda}} = -\frac{\partial \mathcal{H}}{\partial \mathbf{x}} \tag{2.24}$$

$$\mathbf{0} = \frac{\partial \mathcal{H}}{\partial \mathbf{u}} \tag{2.25}$$

$$\boldsymbol{\psi}_0(\mathbf{x}(t_0), t_0) = \mathbf{0} \tag{2.26}$$

$$\boldsymbol{\psi}_f(\mathbf{x}(t_f), t_f) = \mathbf{0} \tag{2.27}$$

$$\boldsymbol{\lambda}^T(t_f) = \left(\frac{\partial \mathcal{G}}{\partial \mathbf{x}}\right)_{t=t_f} \tag{2.28}$$

$$(\mathcal{H})_{t=t_f} = -\left(\frac{\partial \mathcal{G}}{\partial t}\right)_{t=t_f} \tag{2.29}$$

These necessary conditions are used later in the thesis to analyze optimality of obtained solutions. Additional optimality conditions, similar to those in Equations (2.13) and (2.14), must be included if there are inequality constraints involved. Additional equality constraints take the same form as that seen in Section 2.1.2.

2.1.5 Pontryagin's Minimum Principle

Equation (2.25) is used to solve directly for the control function $\mathbf{u}$. In some cases (*e.g.*, $\mathcal{H}$ is a linear function of $\mathbf{u}$), Equation (2.25) is not a function of $\mathbf{u}$ and the above method cannot be used to determine the control. Instead, the control is determined with Pontryagin's minimum principle [25], which is a more general form of the necessary optimality conditions. Pontryagin's minimum principle can be written as follows:

$$\mathbf{u}^* = \arg\min_{\mathbf{u}\in\mathbf{U}} \mathcal{H}(\mathbf{u}, \mathbf{x}^*, \boldsymbol{\lambda}^*, t) \tag{2.30}$$

where $\mathbf{u}^*$ is the optimal control and $\mathbf{U}$ is the set of all admissible controls. The

general idea is to find the control which minimizes the Hamiltonian at each point along the trajectory.

2.2 Numerical Methods

The previous section outlined optimality conditions, which are to be solved to find a stationary point. For most non-linear optimal control problems, solving these equations analytically is very tedious, or impossible. Researchers have instead turned to numerical methods and computers to aide in finding the optimal solution.

There are numerous numerical methods that have been formulated to solve optimal control problems and it is not in the scope of this thesis to explore them all. The method used in this research is the Legendre Pseudospectral Method, which is a direct transcription method that uses a spectral technique. The meanings of "direct", "transcription", and "spectral" will be discussed below and an example will be given to explain implementation of this method.

2.2.1 Direct Methods

Numerical methods used in solving optimal control problems fall into two distinct categories: direct and indirect. An indirect method uses information from the costate differential equations (2.24), the maximum principle (2.30), and the boundary conditions (2.26) - (2.29), to find the optimal solution. In order to use this method an estimate of the costate is required a priori, which may pose a problem since the costate does not usually have physical significance.

The more common approach is to use a direct method, which aims at directly optimizing the cost function, Equation (2.16). The method starts from an initial guess of the state and control and searches in the feasible region for a minimum of the cost function. This is reported as a local minimum solution, because it is impossible to search the entire feasible region. If it can be proven that the problem is convex, then local optimality implies global optimality.

Assuming that the user is familiar with the dynamics of the problem being posed, it

is much easier to provide an initial guess of the state and control rather than the costate. In some cases, a simple propagation of the state from the desired initial conditions with no control input is sufficient. However, if the problem is highly nonconvex, a good initial guess may be crucial in finding the correct local optimal solution.

A direct method was selected for this research for it simplicity and because it does not require costate estimates a priori. Multiple iterations of the solutions were performed, each time providing the optimizer with a different initial guess of the state and control time histories, in order to provide confidence that the obtained results were in fact the global minimum.

2.2.2 Direct Transcription Methods using Spectral Techniques

Within the class of direct methods, there are distinct categories, including direct shooting methods, direct transcription, etc. A direct transcription method is used in this thesis and will be outlined below.

Most real-time optimal control problems are in the continuous time domain. In order to be implemented on a computer, this continuous time domain system must be transformed into a discrete time domain system. The locations in time at which the problem is discretized are referred to as "nodes", and can be uniformly or non-uniformly distributed in the time domain. At each node, the discrete system represents the continuous system, and links must be made between the nodes to represent the dynamics of the original continuous system. A transcription method is used to transform the continuous system into the discrete problem. Most optimal control problems include either a nonlinear cost function or nonlinear constraints (which may include nonlinear dynamical constraints), that are only functions of real variables. As a result, the transcribed problem is an NLP.

The key to a transcription method is not only transforming the problem from a continuous system to a discrete system, but also linking the nodes together in a way that represents the dynamics of the original problem. The dynamics of the continuous system can be represented in several ways within the discrete framework, including the use of the Euler method, the Runge-Kutta method, and spectral methods. The method used in this thesis is a spectral method, which fits globally orthogonal polynomials to the discrete

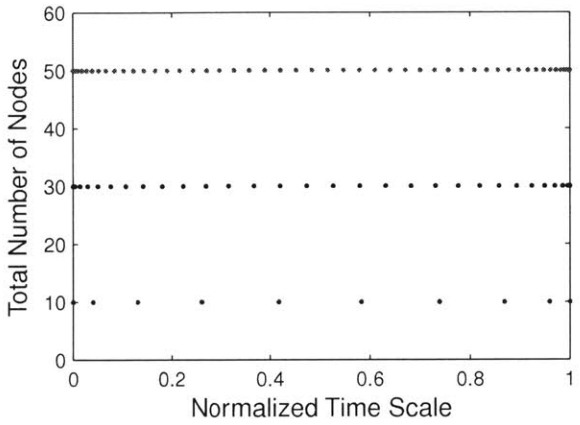

Figure 2-2: Legendre-Gauss-Lobatto Points

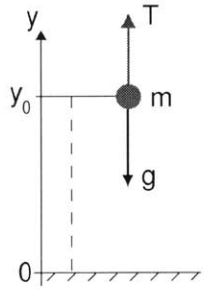

Figure 2-3: Vertical Descent Diagram

data over the entire time span.

The Legendre Pseudospectral Method uses a special class of orthogonal polynomials, known as Legendre Polynomials. The interior nodes are placed at the roots of the Legendre polynomial derivative, known as the Legendre-Gauss-Lobatto (LGL) points, which provides higher accuracy in the results. Figure 2-2 shows the placement of the LGL points for cases with 10, 30, and 50 nodes, respectively.

2.2.3 Implementation

DIDO [19] is the software package used to employ the Legendre Pseudospectral Method in the current research. It is easy to use and is capable of solving a wide variety of problems. To explain some of the implementation concepts of DIDO, a simple example is used.

Assume that a vehicle performs a controlled descent from an initial altitude to the surface of the Moon, as seen in Figure 2-3. For simplicity, assume a constant gravity,

g, and a constant engine exhaust velocity, V_{ex}. If the thrust, T, is represented by a throttle command ($k \in [0, 1]$) multiplied by a maximum thrust limit, T_{max}, the equations of motion are as follows:

$$\dot{y} = v \tag{2.31}$$

$$\dot{v} = \frac{T_{max}\, k}{m} - g \tag{2.32}$$

$$\dot{m} = -\frac{T_{max}\, k}{V_{ex}} \tag{2.33}$$

where y, v, and m represent the altitude, velocity, and mass respectively.

A minimum fuel solution is desired and therefore the cost function was selected to be Equation (2.34), which is the most direct measure of fuel usage. Some of the previous studies have used various norms of the applied translational acceleration as the fuel minimizing cost function, which has been shown to be inaccurate [15].

$$\mathcal{J}_{min} = -m(t_f) \tag{2.34}$$

The constraints on the system, in addition to the equations of motion, are the initial and final boundary conditions and a throttle bound.

Initial Conditions	**Final Conditions**	**Throttle Bound**
$y(t_0) = y_0$	$y(t_f) = y_f$	$0 \leq k(t) \leq 1$
$v(t_0) = v_0$	$v(t_f) = v_f$	
$m(t_0) = m_0$		

The vehicle was initialized at an altitude of 500 m, with a vertical velocity of -5 m/s. The initial mass of the vehicle was chosen to be 1000 kg. The maximum engine thrust and the engine exhaust velocity were chosen as 2500 N and 2500 m/s, respectively. These values are typical values for a lunar lander. A value of 1.62 m/s^2 was used as the lunar gravity constant. The final conditions are to soft-land at zero altitude, meaning that $y_f = 0$ and $v_f = 0$.

Scaling of the variables is a very important step in implementing any optimization problem. Optimization codes run more smoothly and have better convergence properties

Table 2.1: Vertical Descent Parameter Values

Parameter	Value	Normalized Value
T_{max}	2500 N	0.5
V_{ex}	2500 m/s	50
g	1.62 m/s^2	0.324
y_0	500 m	1.0
v_0	-5 m/s	-0.1
m_0	1000 kg	1.0

if the parameters over which it is searching for the optimal solution are roughly of the same order of magnitude. By normalizing the variables in the problem, a much smoother search region is obtained. For this example, the scaling factors were chosen to be 500 m, 10 sec, and 1000 kg, for distance, time and mass respectively. The normalized values of all parameters are listed in Table 2.1. The important dynamical ratios for this vertical descent example have the following values (in normalized units):

$$\frac{T_{max}}{m_0} = 0.5 \qquad \frac{T_{max}}{V_{ex}} = 0.01$$

A total of 64 nodes was used for this simple case because a switch in the control is expected in the middle of the time span, where there are inherently fewer nodes. The number of nodes was increased (to 64) until this switch was adequately captured. The local minimum fuel solution is shown in Figure 2-4. It can be seen that the minimum fuel solution is a free fall trajectory until the point where a maximum commanded throttle, during the remaining portion of the descent, is sufficient to stop the vehicle the instant it reaches the surface. This is the intuitive solution since t_f is also minimized in this fashion. By indirectly minimizing the time, less thrust is expended to counteract gravity.

In Figure 2-4, the discretized DIDO solution is plotted as points. As a feasibility check, the initial conditions are propagated forward using MATLAB's Runge-Kutta integrator (ode45), with the discretized control determined by DIDO. In this plot, the solid line represents either the interpolated control or the propagated state. The alignment of the propagated state (solid line) with the DIDO predicted state at the nodes verifies the

feasibility of the solution.

The Hamiltonian, as defined in Equation (2.20), is found to be:

$$\mathcal{H} = \lambda_y(v) + \lambda_v\left(\frac{T_{max}\ k}{m} - g\right) + \lambda_m\left(-\frac{T_{max}\ k}{V_{ex}}\right) \tag{2.35}$$

Using Equation (2.24), the dynamics of the costate are determined to be:

$$\dot{\lambda_y} = 0 \tag{2.36}$$

$$\dot{\lambda_v} = -\lambda_y \tag{2.37}$$

$$\dot{\lambda_m} = \lambda_v \frac{T_{max}\ k}{m^2} \tag{2.38}$$

The DIDO output includes estimates of both the Hamiltonian and the costate. These are plotted in Figure 2-5. A divergence is seen in the Hamiltonian and costate estimates at the boundaries of the time domain. This is an artifact of the current DIDO implementation of the Legendre Pseudospectral Method.

Because the Hamiltonian is not a function of time, it should be constant over the entire time span. Looking at Figure 2-5, the estimate of the Hamiltonian is fairly small, but oscillations are present. A larger fluctuation is seen where the throttle switch occurs, because of the discontinuity in the control. An interior discontinuity in the state or control is not handled as well by a spectral method.

Looking at Equation (2.36), λ_y should also be constant with time. An oscillation is also seen, but a flat trend is apparent. λ_v on the other hand, should have a constant slope equal to $-\lambda_y$, which is reflected in the plot. These simple tests show that the estimates of the Hamiltonian and costate are reasonable.

Since the Hamiltonian is a linear function of the throttle, Pontryagin's Minimum Principle must be used to determine the control. To find the control which minimizes the Hamiltonian at each node, each term in the Hamiltonian that is a function of the throttle is extracted and k is factored out. This is known as the switching function, which

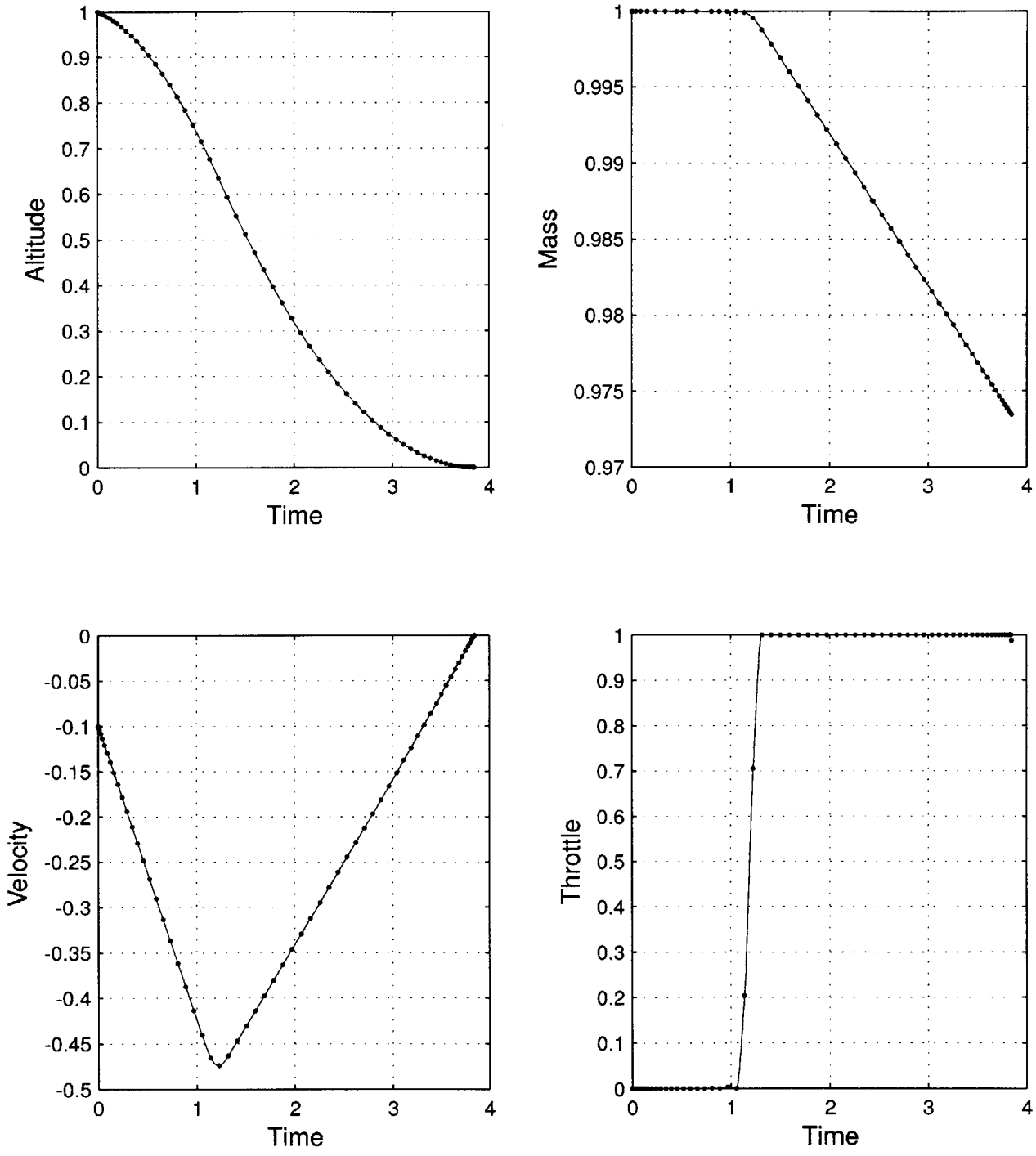

Figure 2-4: Vertical Descent Minimum Fuel Solution (Normalized Units)

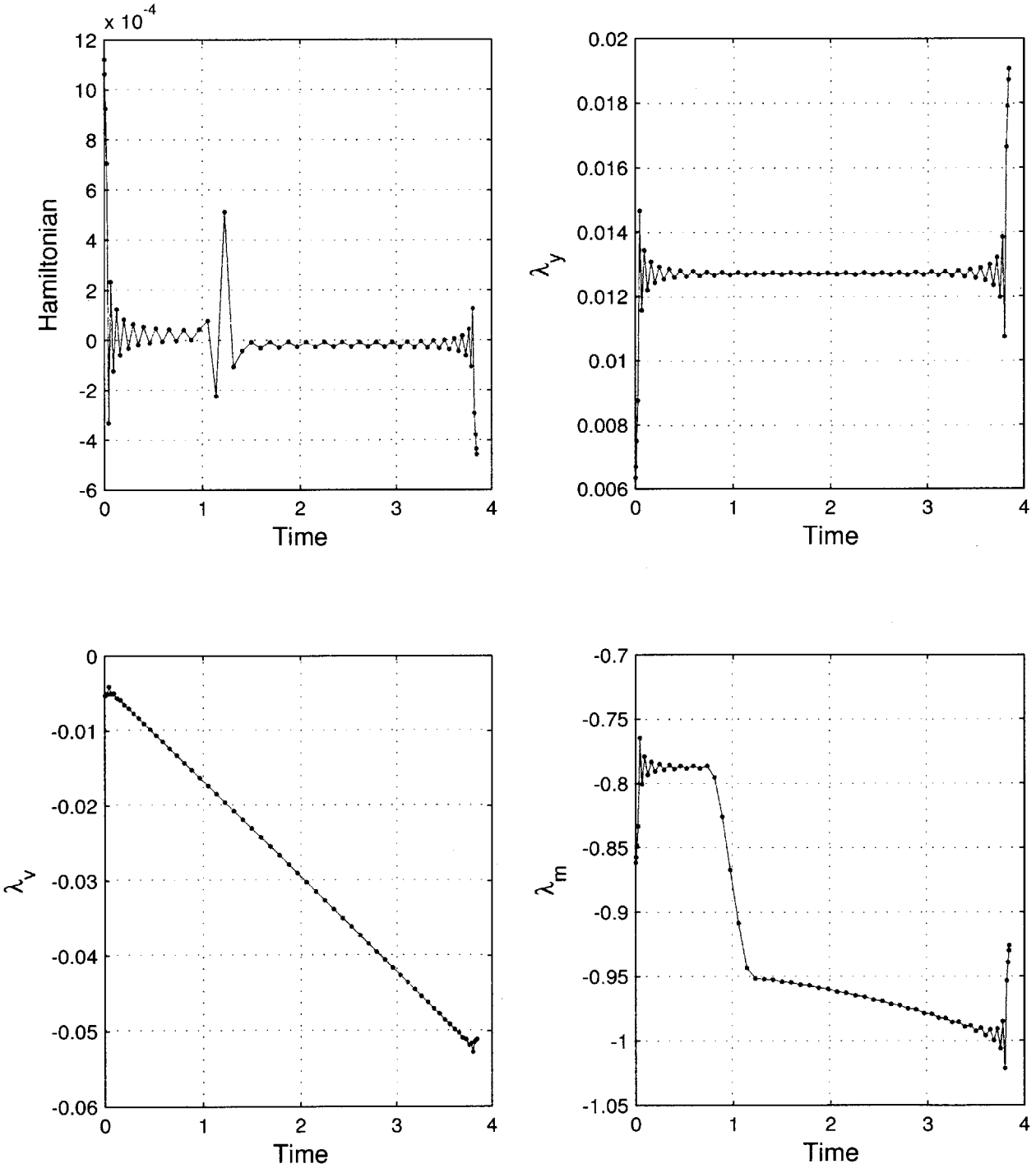

Figure 2-5: DIDO Estimated Hamiltonian and Costate (Normalized Units)

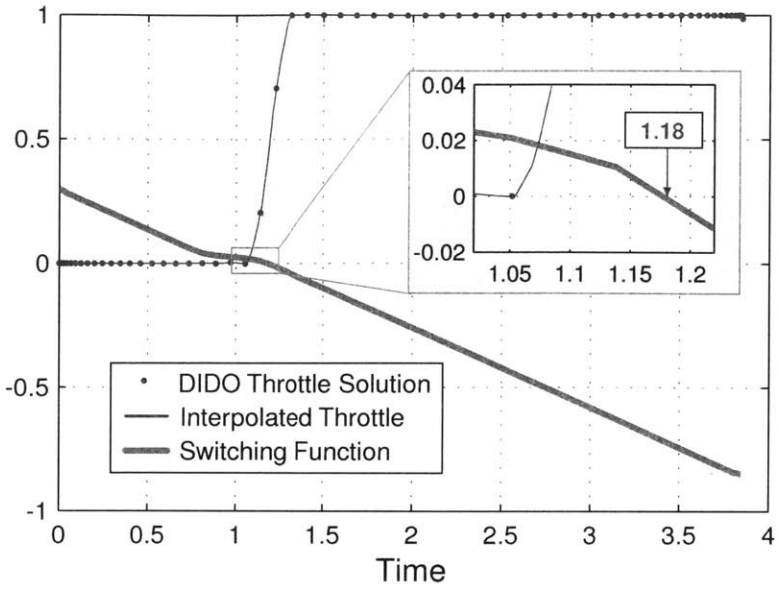

Figure 2-6: Estimated Switching Function

is written as in Equation 2.39 for this example.

$$\mathcal{S} = \left(\lambda_v \frac{T_{max}}{m} - \lambda_m \frac{T_{max}}{V_{ex}}\right) \tag{2.39}$$

By Pontryagin's Minimum Principle, the control is:

$$k(t) = \begin{cases} 0, & \mathcal{S} > 0 \\ 1, & \mathcal{S} < 0 \end{cases} \tag{2.40}$$

The DIDO estimates of the costate were used to calculate an approximate switching function. The result is plotted with the control in Figure 2-6. Using a cubic interpolation between the nodes, an estimate of the location where the switching function crosses zero is 1.18 in normalized time units. Thus, the obtained solution coincides with the estimated switch.

The next logical step is to split the problem into two distinct segments and allow for a discontinuity in the control. This is done in DIDO with the use of knots. Knots can also be used if there are discontinuities in the state (*e.g.*, finite mass jumps in the ascent of a multi-stage rocket). For this problem, the state is equated at the knot, while the throttle

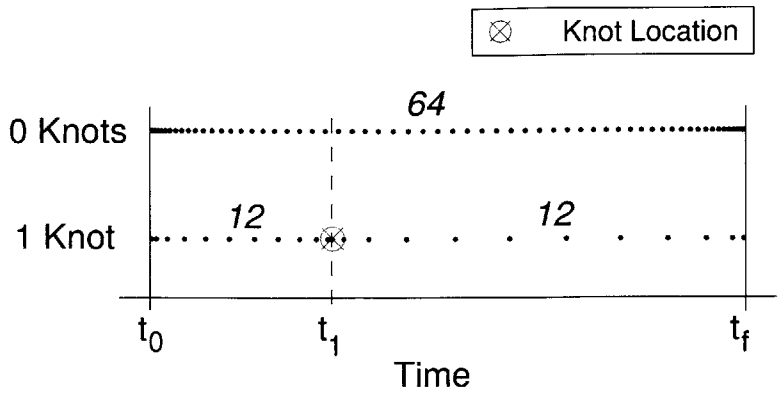

Figure 2-7: Knot Inclusion

is allowed to be discontinuous. Fewer nodes are needed, as seen in Figure 2-7.

A guess of the knot time was provided to the optimizer as 1.18, but this time was allowed to vary. The optimal solution found with one knot added is seen in Figure 2-8. The switch occurred at a normalized time value of 1.19. Therefore, the estimate of the switch location (calculated using an estimate of the costate and the derived switching function) is consistent with the knot location selected by DIDO.

To verify the result obtained from DIDO, an analytic solution is calculated from the method derived by Meditch [11]. He shows that there is no more than one switch in the throttle for the 1-dimensional vertical descent problem, and that the throttle changes from minimum to maximum at the switch. Using Pontryagin's minimum principle, Meditch derived an analytic expression to calculate the time where the switch occurs. The expression is shown below in Equation (2.41). In deriving this equation, an assumption is made that no more than 25% of the initial mass is used as propellant during the descent. This assumption is valid for this example.

$$\mathcal{N}(y, v, t) = \frac{b}{a} y(t) + 2a\sqrt{\frac{y(t)}{a}} + v(t) \tag{2.41}$$

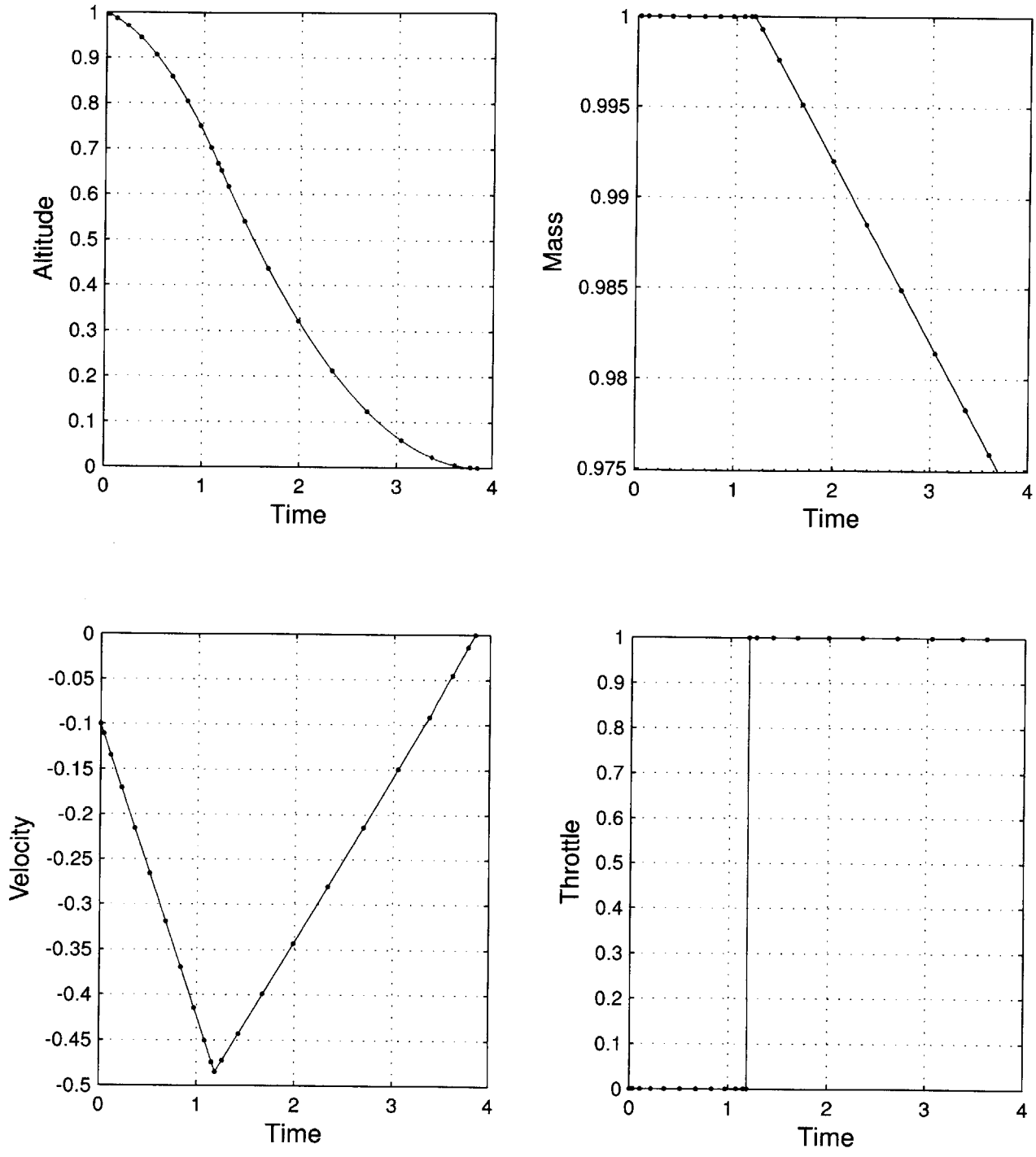

Figure 2-8: Vertical Descent Solution With One Knot (Normalized Units)

where

$$a = \frac{1}{2}\left(\frac{T_{max} - g\,m_0}{m_0}\right) \tag{2.42}$$

$$b = \frac{T_{max}^2}{2\,V_{ex}\,m_0^2} \tag{2.43}$$

The analytical solution placed the switch location at a normalized time of 1.21. The DIDO solution matches the analytical solution of the switching time, within a reasonable error of 1.6%. This simple vertical descent example has shown that solutions obtained by DIDO are good approximation of the optimal solution.

In the subsequent chapters, a soft-landing on the Moon from a parking orbit is analyzed using the same DIDO optimization utility. An optimal solution is first obtain with minimum constraints and no interior knots in order to analyze the optimality of the results and get an estimate of control discontinuity locations. The current implementation of DIDO does not provide estimates of the costate and Hamiltonian if interior knots are included, hence this analysis can only be performed with a solution that does not include knots. Knots are then added to the optimization framework in order to accurately capture control discontinuities, and to enforce desired characteristics of the trajectory based on operational considerations.

[This page intentionally left blank.]

Chapter 3

Moon Landing Problem

This chapter presents details of the Moon landing scenario being investigated. Included within are assumptions made, coordinate frames used, definitions of terms, and an overview of the trajectory.

3.1 Assumptions

The rotational period of the Moon about its own axis is equal to the period of revolution around the Earth. The equatorial surface velocity is approximately 4.6 m/s. This rotation would be a factor if the goal was to target a specific landing site because the site would move relative to the inertial frame. However, a target is not specified in this analysis and it is reasonable to neglect the rotation of the Moon. The extra fuel expenditure required to null the velocity of the vehicle relative to the rotating surface would be no more than 0.3% of the total fuel usage. This is not a significant factor and would not noticeably alter the results or trends.

The Moon has no atmosphere and is assumed to be spherical. A purely Newtonian gravity model is used, therefore gravity perturbations due to the Earth and Sun are neglected, as well as perturbations due to the oblateness of the Moon. Values used for the lunar equatorial radius, R_{eq}, and the lunar gravitational parameter, μ, are 1737.4 km and 4902.78 km^3/s^2, respectively [26].

An assumption of constant vehicle exhaust velocity is common in space flight me-

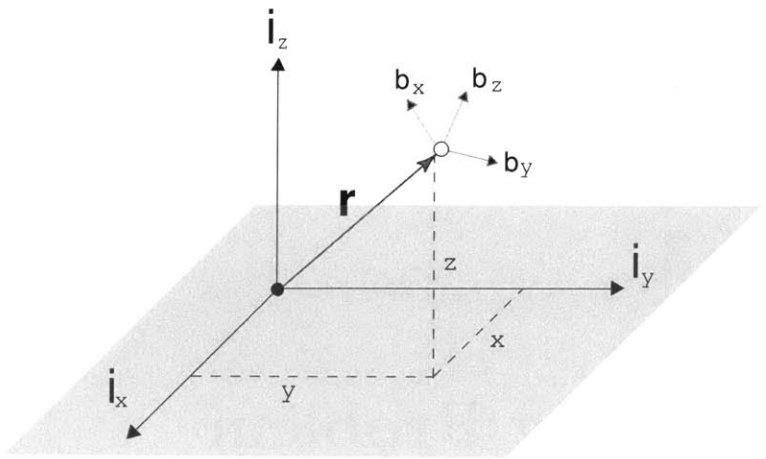

Figure 3-1: Three-Dimensional Inertial and Body Reference Frames

chanics problems because the properties of the engine do not change drastically in the operational range being used.

3.2 Reference Frames and Coordinate Systems

Three reference frames are used: the Inertial frame, the Vehicle Body frame, and a Rotating Polar frame. Where ambiguity is present, the frames are denoted with superscripts $(\,)^i$, $(\,)^b$ and $(\,)^r$, respectfully.

The standard unit vectors, $\hat{\mathbf{i}}_x$, $\hat{\mathbf{i}}_y$, and $\hat{\mathbf{i}}_z$ complete the inertial triad as seen in Figure 3-1. In this frame, the position vector, $\mathbf{r}$, is expressed as:

$$\mathbf{r} = x\hat{\mathbf{i}}_x + y\hat{\mathbf{i}}_y + z\hat{\mathbf{i}}_z \tag{3.1}$$

The body frame is fixed to the vehicle and is given by the 3-dimensional unit vector triad $[\hat{\mathbf{b}}_x, \hat{\mathbf{b}}_y, \hat{\mathbf{b}}_z]$.

For a majority of the research done, the motion of the vehicle is restricted to a single plane of motion, namely the Moon's equatorial plane. If we define the x-y plane as the plane of motion, the inertial frame simplifies to the perpendicular unit vector set $[\hat{\mathbf{i}}_x, \hat{\mathbf{i}}_y]$. The body frame also reduces to the 2-dimensional perpendicular unit vectors $[\hat{\mathbf{b}}_x, \hat{\mathbf{b}}_y]$. An illustration of this is seen in Figure 3-2. The position vector reduces from Equation (3.1)

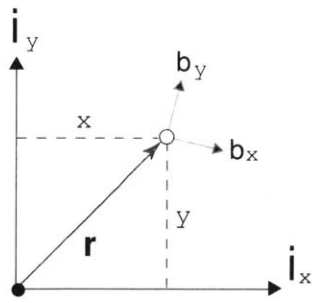

Figure 3-2: Two-Dimensional Inertial and Body Reference Frames

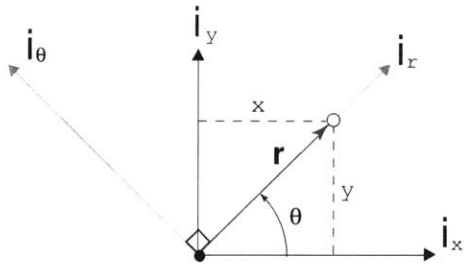

Figure 3-3: Two-Dimensional Inertial and Rotating Polar Frames

to Equation (3.2).

$$\mathbf{r} = x\hat{\mathbf{i}}_x + y\hat{\mathbf{i}}_y \tag{3.2}$$

By defining unit vectors $\hat{\mathbf{i}}_r$ and $\hat{\mathbf{i}}_\theta$ as in Equations (3.3) and (3.4) a rotating reference frame is created. This frame rotates at the same rate that the vehicle revolves around the Moon. It is referred to as the 'rotating polar frame' because of it is connection with the polar coordinates r and θ.

$$\hat{\mathbf{i}}_r = \cos\theta\hat{\mathbf{i}}_x + \sin\theta\hat{\mathbf{i}}_y \tag{3.3}$$

$$\hat{\mathbf{i}}_\theta = -\sin\theta\hat{\mathbf{i}}_x + \cos\theta\hat{\mathbf{i}}_y \tag{3.4}$$

Figure 3-3 displays the relationship between the rotating polar frame and the inertial frame (for planar motion). The vector $\hat{\mathbf{i}}_r$ always points from the origin to the vehicle and $\hat{\mathbf{i}}_\theta$ remains perpendicular to the radius vector in the direction of motion of the vehicle. The position vector can be expressed rather simply in the rotating polar frame as:

$$\mathbf{r} = r\hat{\mathbf{i}}_r \tag{3.5}$$

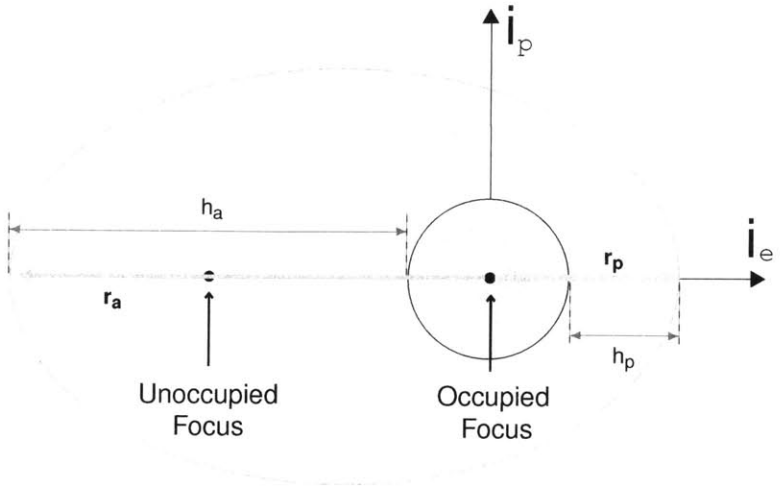

Figure 3-4: Orbital Dynamics Definitions

3.3 Orbital Dynamics Definitions

Standard orbital dynamics definitions [27] used in this document are displayed in Figure 3-4. The unit vectors $\hat{\mathbf{i}}_e$ and $\hat{\mathbf{i}}_p$ lie in the vehicle's orbital plane with $\hat{\mathbf{i}}_e$ in the direction of the pericenter, which is the point of closest approach of the orbit to the occupied focus. $\hat{\mathbf{i}}_p$ is perpendicular to $\hat{\mathbf{i}}_e$ in the plane of motion of the vehicle.

In the case of a lunar orbit, the pericenter is referred to as the perilune. The vector from the occupied focus to the perilune is defined as the perilune radius vector, $\mathbf{r_p}$. The altitude at this point above the surface is referred to as the perilune altitude, h_p. Conversely, the farthest point in the orbit is known as the apolune and the associated altitude is the apolune altitude, h_a.

With the position and velocity of the vehicle are denoted by $\mathbf{r}$ and $\mathbf{v}$, the perilune and apolune heights can be calculated using the following equations [27]:

$$\mathbf{h} = \mathbf{r} \times \mathbf{v} \tag{3.6}$$

$$\mathbf{e} = \frac{1}{\mu}\left(\mathbf{v} \times \mathbf{h} - \frac{\mu}{r}\,\mathbf{r}\right) \tag{3.7}$$

$$p = \frac{h^2}{\mu} \tag{3.8}$$

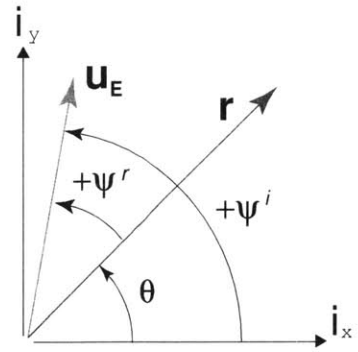

Figure 3-5: Thrust Angle Definitions

Perilune	**Apolune**	
$r_p = \frac{p}{1+e}$	$r_a = \frac{p}{1-e}$	(3.9)
$h_p = r_p - R_{eq}$	$h_a = r_a - R_{eq}$	(3.10)

where **h** and **e** are the massless angular momentum and eccentricity vectors, μ and R_{eq} are the lunar gravitational parameter and equatorial radius, and p is the parameter of the orbit, which is defined by Equation (3.8). The variables r, h, and e denote the magnitudes of the corresponding vector. Note the distinction between h_p and h_a, which both represents altitudes, and h, which is the magnitude of the massless angular momentum.

3.4 Angle Definitions

The planar equations of motion in both the cartesian and polar frames use a thrust direction angle, ψ, to represent the angular distance from a reference axis to the unit thrust vector. The cartesian equations of motion (EOM) uses ψ^i, which is defined from the fixed inertial x-axis. It is more convenient in the rotating polar frame to use ψ^r, which is defined from the rotating radius vector. Figure 3-5 is included for clarity. Equation (3.11) relates the two angles. By taking the derivative of Equation (3.11) with respect to time, the relationship in Equation (3.12) is obtained.

$$\psi^i = \psi^r + \theta \tag{3.11}$$

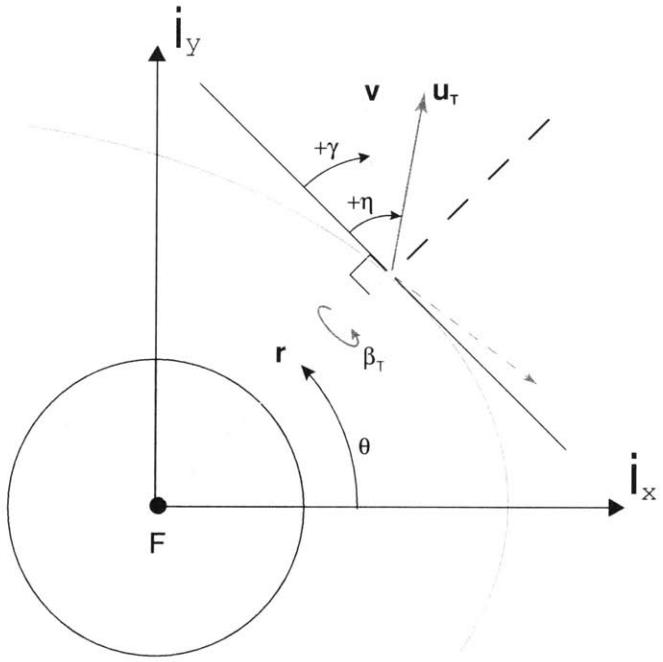

Figure 3-6: Angle Definitions

$$\dot{\psi}^i = \dot{\psi}^r + \dot{\theta} \tag{3.12}$$

For plotting purposes, the flight path angle, γ, and thrust direction angle, η, are defined. These angles are illustrated in Figure 3-6. The flight path angle, γ, is the angle between the velocity vector and a line perpendicular to the radius vector in the direction of motion, which is referred to as the local horizontal. The unit thrust vector is defined with a yaw-pitch angle sequence, which is defined as a rotation about the radius vector by the angle β_T and then a rotation about the z-axis (for the planar motion case) by the angle η. The thrust yaw angle, β_T, is defined from the direction of positive velocity. The thrust direction (pitch) angle, η, is the angle between the thrust vector and the local horizontal. The dotted vectors in Figure 3-6 show typical placements of the velocity and thrust vectors for the cases in this study.

3.5 Trajectory Description

A vehicle that transfers from the Earth to the Moon arrives on a hyperbolic trajectory (when viewed from the vicinity of the Moon) by the laws of Keplerian motion. It is the

decision of trajectory planners to determine whether the vehicle will descend directly to the surface from the hyperbolic orbit, or if the vehicle will first enter into a parking orbit around the Moon before attempting to land.

Both direct descent and parking orbit trajectories have their advantages and disadvantages. A direct descent trajectory requires fewer maneuvers and typically uses less fuel. One disadvantage, however, is that the Earth departure timing becomes crucial. The departure must be timed so that the vehicle not only transfers to the Moon with high accuracy, but also is in the correct position relative to the landing site at arrival. During a direct descent, there is less time to make adjustments to the orbit or assess how much navigational error has accumulated during the Earth-Moon transfer.

On the other hand, the parking orbit trajectory expends extra fuel to enter the parking orbit, but can remain in this orbit until the time of final descent. This allows time to observe landing sites, make adjustments to the orbit, perform scientific experiments, etc. The motion of the vehicle can also be observed for a longer duration of time to assess navigational error accumulation. Historically, missions to the Moon that successfully landed have entered into parking orbits before landing. The safety benefits have far outweighed the additional cost in extra fuel and maneuvers.

The Surveyor missions were unmanned vehicles launched during the years of 1966 to 1968 with the objective of soft landing on the Moon [5]. Of the seven Surveyor spacecraft launched, only five successfully made the voyage. Three were designed for a direct descent trajectory (Surveyor I, II, and IV) and four entered into a parking orbit for a short duration of time before initiating the final descent (Surveyor III, V, VI, and VII). Of the missions which used a direct descent, only Surveyor I successfully landed. Surveyor II and IV were terminated before lunar contact due to anomalies during flight. The parking orbit coast of Surveyor III, V, VI, and VII varied from 6.7 min to 22.4 min in duration, and all of these missions successfully landed.

All of the Apollo missions entered into an initial lunar orbit with average apolune and perilune altitudes of 310 km and 106 km, respectively [28]. The first Apollo landing missions, Apollo 11 and 12, performed an intermediate burn to bring the spacecraft's orbit to near-circular (120.6 km apolune and 99.5 km perilune). Apollo missions 14, 15,

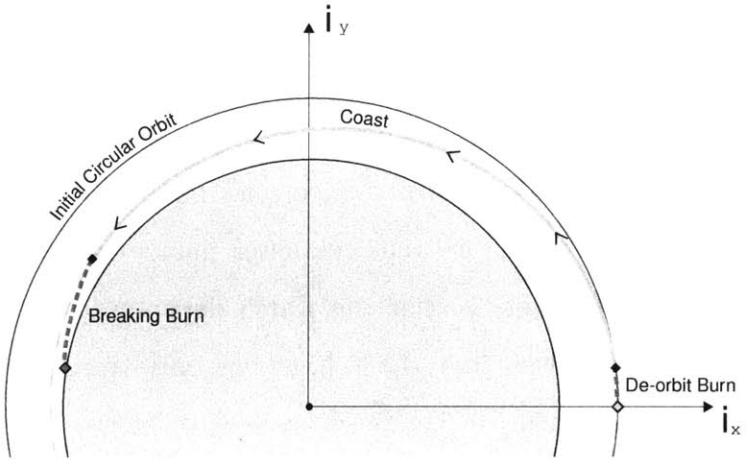

Figure 3-7: Position of Circular Orbit Case

16, and 17 transferred directly from the insertion orbit to the descent orbit, the later having average values of 109 km apolune and 15.3 km perilune for all six missions. Near the perilune altitude of the descent orbit, the descent engines were ignited and the final descent to the surface began. The engines remained ignited for the duration of the final descent in order to avoid the possibility of the engines not reigniting while the vehicle was in close proximity to the Moon. This failure mode is referred to as "engine restart failure" in this thesis.

The perilune altitude was chosen for fuel efficiency and to minimize the time that the vehicle was on a collision course with the surface. Having a perilune altitude above 15 km was found to be fuel inefficient and a perilune altitude below 15 km was hazardous because of the mountainous lunar terrain and possible guidance errors [3].

For this research, a descent from a lunar parking orbit was selected for reasons consistent with the historical perspective; namely safety, reliability, and flexibility. The vehicle transfers from the initial parking orbit to an intermediary descent orbit, which has a lower perilune altitude that brings the vehicle close to the lunar surface. The final breaking burn commences near perilune of the descent orbit and decreases the vehicle's velocity and altitude for a soft landing on the lunar surface. An illustration of the trajectory can be seen in Figure 3-7.

For simplicity, the initial parking orbit is assumed to be circular at an altitude of 40

km. The primary effect of changing the parking orbit to have a higher apolune altitude is to increase the velocity of the vehicle at perilune. This would increase the initial velocity of the vehicle in the optimization framework and contribute to the overall velocity to be nulled during the descent. If desired, the fuel needed to account for this change in apolune altitude can be calculated with a Hohmann Transfer [27] and included into the fuel cost.

The throttle profile consists of a small de-orbit burn, a portion of zero thrust, and then a large breaking burn. The de-orbit burn has a duration on the scale of 1 to 20 s, depending on the characteristics of the desired descent orbit. The breaking burn has a much longer duration (*e.g.*, Apollo average: 738.7 s [28]). Since there is no atmosphere on the Moon, the descent trajectory is very different from an Earth re-entry or a Martian landing. Instead of using the atmosphere to dissipate energy, the main thrust engine(s) must be used to decelerate the vehicle. A large braking burn is required to null the velocity from orbiting velocities to near-zero at the surface.

For the Apollo missions, the final descent phase was further divided into a braking phase, an approach phase, and a terminal descent phase, with a separate guidance scheme used for each phase [7]. The main purpose of the approach and terminal phases were to rotate the vehicle to a vertical position and cancel any remaining velocity. For the current study these subdivisions were not made. Instead, terminal attitude constraints are imposed and the entire trajectory is optimized to land with a vertical attitude and a near-zero vertical velocity.

3.6 Operational Considerations Included in the Optimization Design Problem

The goal of this research is to not only find optimal solutions, but also solutions that are viable and operationally feasible. Selected operational considerations are included in the optimization framework to enforce certain characteristics on the trajectory and to assess how these considerations effect the optimum results. Considerations, such as descent orbit perilune altitude, continuous braking, and attitude are included.

The intermediary descent orbit is very important in the design of the trajectory. It is desired that the perilune altitude of the descent orbit have a positive value in order to minimize the time the vehicle is on a collision course with the Moon. This is done for vehicle safety, but also for environmental precaution against objects unintentionally impacting the lunar surface. If a failure were to occur for any reason, the vehicle could continue to orbit the Moon while the situation was being assessed, if the vehicle's orbit had a positive perilune height.

Maintaining a continuous thrust during the final braking burn reduces the probability of engine restart failure when the vehicle's trajectory is reduced to a collision course with the Moon. Constraints are added to the throttle profile in order to keep the thrust above a minimum threshold during the final burn.

When landing, it is ideal to have the vehicle land with purely vertical motion and with the legs of the vehicle pointed towards the surface. This attitude is referred to as the "legs-down" orientation. Constraints are placed on the terminal phase to ensure vehicle orientation at landing. It is also desirable to land with a small descending vertical velocity to ensure touchdown, while not exceeding the structural integrity of the vehicle.

These operational considerations, as well as a few others, are discussed in more detail in Chapter 5.

3.7 Vehicle Specifications

The vehicle is assumed to be axially symmetric with a thrust to weight ratio that varies between 2.0 and 8.0. It assumed that the vehicle has one throttlable main engine, which is fixed to the vehicle and does not gimbal. For a hypothetical initial mass of 1800 kg (which is representative of an unmanned vehicle), a value of 8000 N was chosen for the engine's maximum thrust limit, T_{maxE}. The engine's exhaust velocity, V_{ex}, was chosen as 3500 m/s, which corresponds to a specific impulse of 358 s.

In comparison, the Surveyor vehicles had final landed masses varying from 1431 to 1486 kg [5]. Each lander had a propulsion system which consisted of one main solid propellant retro-fire engine and three throttlable liquid propellant vernier engines. The

vernier engines, which were used to remove the final 100 m/s of velocity and also for attitude control during the retro-fire, were capable of providing 133 N to 463 N of thrust each. They had a specific impulse which varied from 273 s at minimum thrust to 287 s at maximum thrust [29].

[This page intentionally left blank.]

Chapter 4

Equations of Motion

The equations of motion (EOM) of the vehicle are developed in this chapter. Initially, the full six degree-of-freedom (DOF) EOM are developed before simplifications are introduced to obtain the EOM used during analysis.

4.1 Six Degree-of-Freedom EOM

The complete 6-DOF EOM include translational dynamics, rotational dynamics, and a mass flow equation. These components will be discussed separately in the sections to follow.

4.1.1 Translational Dynamics

The vehicle's position and velocity, in cartesian coordinates, are represented by the vectors $\mathbf{r}$ and $\mathbf{v}$, as defined in Equations (4.1) and (4.2).

$$\mathbf{r}^T = \begin{bmatrix} x & y & z \end{bmatrix} \tag{4.1}$$

$$\mathbf{v}^T = \begin{bmatrix} v_x & v_y & v_z \end{bmatrix} \tag{4.2}$$

The thrust vector, $\mathbf{T}$, is realized by multiplying a throttle command, k_E, the maximum engine thrust, T_{maxE}, and the unit thrust vector, $\mathbf{u_E}$. The thrust unit vector defines the direction of thrust in the inertial frame. It is assumed that there is a single engine fixed

to the vehicle and $k_E \in [0, 1]$.

$$\mathbf{u_E}^T = \begin{bmatrix} u_{Ex} & u_{Ey} & u_{Ez} \end{bmatrix} \tag{4.3}$$

$$\mathbf{T} = T_{maxE}\, k_E\, \mathbf{u_E} \tag{4.4}$$

Given these vector definitions, the translational equations of motion can be written as follows:

$$\dot{\mathbf{r}} = \mathbf{v} \tag{4.5}$$

$$\dot{\mathbf{v}} = -\frac{\mu}{r^3}\mathbf{r} + \frac{T_{maxE}\, k_E}{m}\mathbf{u_E} \tag{4.6}$$

where m and μ are the vehicle mass and the planet gravitational parameter, respectively. The first term in Equation (4.6) represents gravity, while the second term is acceleration due to the applied thrust.

4.1.2 Rotational Dynamics

Vehicle rotation is defined using a quaternion for its non-singular properties. Attitude quaternions are also commonly used in vehicle guidance and navigation [30]. A right-handed, 4$^{\text{th}}$ part scalar nomenclature is used as seen in Equation (4.7).

$$\bar{\mathbf{q}} = \begin{bmatrix} \mathbf{q} \\ q_0 \end{bmatrix} = \begin{bmatrix} \mathbf{u}\sin(\phi/2) \\ \cos(\phi/2) \end{bmatrix} \tag{4.7}$$

In this thesis, the quaternion represents a body-to-inertial rotation, which is denoted as $\bar{\mathbf{q}}_b^i$. Angular rates are given by the vector $\boldsymbol{\omega}_{b/i}^b$, which represents the angular rate of the body with respect to the inertial frame, defined in body coordinates. For simplicity, notations on the quaternion and angular rate vectors are omitted ($\bar{\mathbf{q}}_b^i = \bar{\mathbf{q}}$ and $\boldsymbol{\omega}_{b/i}^b = \boldsymbol{\omega}$).

The reaction control system (RCS), which is composed of small thrusters (or jets) located around the perimeter of the vehicle, controls the rotational motion. The torque produced from each RCS jet is realized as $T_{maxJ}\,(\mathbf{d}_j \times k_j \mathbf{u}_j)$, where $\mathbf{d}_j$ is the location of

the j^{th} jet with respect to the vehicle's center of gravity. It is assumed that the jets are coupled and produce no net translational motion.

The RCS maximum thrust limit, T_{maxJ}, is normally significantly smaller than the engine's thrust capability, T_{maxE}. Similar to the model of the engine throttle, the j^{th} jet throttle command is represented with the variable k_j, where $k_j \in [0, 1]$. Lastly, $\mathbf{u}_j$ is the j^{th} jet body-fixed thrust vector, defined in the body frame. The total applied torque, $\boldsymbol{\tau}$, is obtained by summing the torque produced by each individual jet.

$$\boldsymbol{\tau} = T_{maxJ} \sum_{j=1}^{N} (\mathbf{d}_j \times k_j \mathbf{u}_j) \tag{4.8}$$

The full 6-DOF rotational EOM include the quaternion kinematics and angular rate dynamics listed below, which are defined in the body frame.

$$\dot{\bar{\mathbf{q}}} = -\frac{1}{2}\, \boldsymbol{\Omega}(\boldsymbol{\omega})\, \bar{\mathbf{q}} \tag{4.9}$$

$$\dot{\boldsymbol{\omega}} = \mathbf{I}^{-1} \left(\frac{T_{maxJ}}{m} \sum_{j=1}^{N} (\mathbf{d}_j \times k_j \mathbf{u}_j) - \boldsymbol{\omega} \times \mathbf{I}\boldsymbol{\omega} \right) \tag{4.10}$$

where the vehicle inertia matrix is defined as $\mathbf{I}$ and the variable $\boldsymbol{\Omega}$, as defined in Equation (4.11), is a 4x4 matrix used in the differential equation of the quaternion [30]. A negative sign is placed in Equation (4.9) because of the definitions of $\bar{\mathbf{q}}$ and $\boldsymbol{\omega}$. The first term in Equation (4.10) represents the applied torque, while the second term includes the inertia of the vehicle.

$$\boldsymbol{\Omega}(\boldsymbol{\omega}) = \begin{bmatrix} 0 & \omega_z & -\omega_y & \omega_x \\ -\omega_z & 0 & \omega_x & \omega_y \\ \omega_y & -\omega_x & 0 & \omega_z \\ -\omega_x & -\omega_y & -\omega_z & 0 \end{bmatrix} \tag{4.11}$$

The attitude of the vehicle is related to the vehicle's translation motion by rotating the body-fixed thrust vector, $\mathbf{u_E}^b$, to the inertial frame via the quaternion rotation seen in Equation (4.12). The inertial frame thrust vector, $\mathbf{u_E}$, is then used in the translational

dynamics in Equation (4.6).

$$\bar{\mathbf{u}_\mathbf{E}}^i = \bar{\mathbf{q}}_b^{i*}\, \bar{\mathbf{u}_\mathbf{E}}^b\, \bar{\mathbf{q}}_b^i \tag{4.12}$$

where:

$$\bar{\mathbf{q}}_b^{i*} = \begin{bmatrix} -\mathbf{q} \\ q_o \end{bmatrix} \qquad \bar{\mathbf{u}_\mathbf{E}}^i = \begin{bmatrix} \mathbf{u_E} \\ 0 \end{bmatrix} \qquad \bar{\mathbf{u}_\mathbf{E}}^b = \begin{bmatrix} \mathbf{u_E}^b \\ 0 \end{bmatrix}$$

4.1.3 Mass Flow Equation

The mass of the vehicle decreases when either the engine or the thrusters are ignited. Equation (4.13) represents the complete mass flow equation. The subscripts 'E' and 'J' distinguish engine and RCS jet quantities.

$$\dot{m} = -\frac{T_{maxE}\, k_E}{V_{exE}} - \frac{T_{maxJ}}{V_{exJ}} \sum_{j=1}^{N_J} k_j \tag{4.13}$$

4.2 Planar Equations of Motion

Six DOF motion was simplified to two translational components and one rotational. Per definition, this is a 3-DOF system, but as this term is generally used to indicate three dimensional translational motion without rotation, it is instead referred to as planar motion.

Both cartesian and polar forms of the EOM were investigated for the planar problem and are derived in this section. The term 'cartesian form' refers to the use of cartesian coordinates in the inertial frame. The term 'polar form' refers to the use of radial and circumferential components in the rotating reference frame. The motivation to use polar form is due to mathematical simplifications in the bound and constraint equations, which will be further discussed in Section 5.2.

4.2.1 Translational Dynamics in Cartesian Form

By constraining motion to the inertial x-y plane, for the cartesian form, the z-component of the translational dynamics becomes zero. The position and velocity vectors become:

$$\mathbf{r}^T = \begin{bmatrix} x & y \end{bmatrix} \tag{4.14}$$

$$\mathbf{v}^T = \begin{bmatrix} v_x & v_y \end{bmatrix} \tag{4.15}$$

The planar translational dynamics reduce to Equations (4.16) - (4.19), with the thrust angle ψ^i being defined as the angle between the inertial x-axis and the unit thrust vector ($\tan\psi^i = u_{Ey}/u_{Ex}$). The equations have been written in scalar quantities in order to compare with the EOM in polar form.

$$\dot{x} = v_x \tag{4.16}$$

$$\dot{y} = v_y \tag{4.17}$$

$$\dot{v}_x = -\frac{\mu}{r^3}\,x + \frac{T_{maxE}\,k_E}{m}\cos\psi^i \tag{4.18}$$

$$\dot{v}_y = -\frac{\mu}{r^3}\,y + \frac{T_{maxE}\,k_E}{m}\sin\psi^i \tag{4.19}$$

4.2.2 Translational Dynamics in Polar Form

In polar form, the position of the vehicle is defined with the radius, r, and the central angle θ, which is defined from the inertial x-axis. The velocity is defined with radial and circumferential components, v_r and v_θ. Defining ψ^r as the angle from the radius vector to the thrust vector, the translational dynamics are governed by:

$$\dot{r} = v_r \tag{4.20}$$

$$\dot{\theta} = \frac{v_\theta}{r} \tag{4.21}$$

$$\dot{v}_r = \frac{v_\theta^2}{r} - \frac{\mu}{r^2} + \frac{T_{maxE}\,k_E}{m}\cos\psi^r \tag{4.22}$$

$$\dot{v}_\theta = -\frac{v_r v_\theta}{r} + \frac{T_{maxE}\,k_E}{m}\sin\psi^r \tag{4.23}$$

In Equation (4.22), $\frac{v_\theta^2}{r}$ and $-\frac{\mu}{r^2}$ are the centrifugal and gravity terms, respectfully. The last terms in both of these equations is the acceleration due to the applied thrust. It should be emphasized that ψ^i (in Equations (4.18) and (4.19)) is referenced to the inertial x-axis, while ψ^r (in Equations (4.22) and (4.23)) is referenced to the rotating radius vector.

4.2.3 Rotational Kinematics

In both planar inertial and rotating reference frame cases, the vehicle rotates about an axis which is normal to the plane of translational motion. If the vehicle is assumed to be axially symmetric, the inertia matrix becomes a diagonal matrix and the second term inside the brackets in Equation (4.10) becomes zero. As a result, the rotational EOM can be simplified by governing the rate of change of the inertial angular velocity through a commanded inertial angular acceleration, α. The rotational EOM reduce to:

Cartesian	**Polar**	(4.24)
$\dot{\psi}^i = \omega$	$\dot{\psi}^r = \omega - \dot{\theta}$	(4.25)
$\dot{\omega} = \alpha$	$\dot{\omega} = \alpha$	(4.26)

4.2.4 Variable Mass

Lastly, the mass flow equation, seen in Equation (4.13), is the same in both cartesian and polar forms. It is similar to Equation (4.13) with the mass flow due to the thrusters neglected. This is a reasonable assumption because the mass flow due to the engine is significantly larger than the combined mass flow due to the RCS jets. An indirect method of accounting for the depletion of mass due to RCS jets will be discussed in Section 5.2.

$$\dot{m} = -\frac{T_{maxE}\, k_E}{V_{exE}} \tag{4.27}$$

Chapter 5

Results

This chapter explores the results obtained during trajectory optimization of the Moon Landing problem. The equations of motions derived in Chapter 4 were coded in DIDO in a fashion similar to the example problem seen in Chapter 2. In this thesis, all work is limited to planar motion, but can easily be extended to three-dimensions. The plane of motion is assumed to be the Moon's equatorial plane.

Guidance algorithms developed for spacecraft landing typically emphasize translational motion. It is left to the vehicle's attitude control system to rotate the vehicle in such a way to match the desired thrust direction (and motion) specified by the guidance computer. The attitude controller response is not instantaneous, due to the vehicle inertia. Sudden changes in the desired attitude of the vehicle are not possible as might be assumed by the guidance algorithm. By including attitude kinematics in the optimal control problem, a more realistic solution is obtained, which does not include discontinuities in the attitude of the vehicle. One of the main contributions of this thesis is the inclusion of the attitude kinematics in the optimization framework and the comparison to pure translational motion results.

Analysis was performed, first using pure translational motion (*i.e.*, two degrees-of-freedom), then vehicle rotation about a single axis was included (*i.e.*, three degrees-of-freedom). This is done in order to compare the pure translational motion results to solutions that include attitude kinematics. For clarity, 2-dimensional translational motion is given the acronym TM, while motion with two translational degrees-of-freedom and one

rotational degree-of-freedom is given the acronym TMR.

The convexity of this problem was not determined, therefore all results are reported as local optimum solutions. Multiple iterations were performed in each case, from varying initial guesses of the state and control at each node, to ensure convergence to the same solution. Performing multiple iterations, with different starting guess values provided higher confidence that the obtained solutions were in fact the global minimum, though this was not formally proven.

An initial parking orbit of $40km$ was chosen for the analysis throughout this thesis, as discussed in Section 3.5. Given the gravitational pull of the Moon and the characteristics of a circular orbit, the velocity of the vehicle is calculated to be 1660.8 m/s.

5.1 Translational Motion (TM)

For the pure translational motion analysis, the cartesian form of the equations of motion where used. The equations of motion were seen in Equations (4.16) - (4.19) and (4.27), and are restated below for quick reference. Note that these equations are two-dimensional, and it is assumed that the vehicle's motion is in the Moon's equatorial plane.

$$\dot{x} = v_x \tag{5.1}$$

$$\dot{y} = v_y \tag{5.2}$$

$$\dot{v}_x = -\frac{\mu}{r^3}\, x + \frac{T_{maxE}\, k_E}{m}\, u_{E1} \tag{5.3}$$

$$\dot{v}_y = -\frac{\mu}{r^3}\, y + \frac{T_{maxE}\, k_E}{m}\, u_{E2} \tag{5.4}$$

$$\dot{m} = -\frac{T_{maxE}\, k_E}{V_{exE}} \tag{5.5}$$

The state and control of the system are defined as:

$$\mathbf{x}(t)^T = [\, x(t) \quad y(t) \quad v_x(t) \quad v_y(t) \quad m(t) \,] \tag{5.6}$$

$$\mathbf{u}(t)^T = [\, k_E(t) \quad u_{E1}(t) \quad u_{E2}(t) \,] \tag{5.7}$$

where u_{E1} and u_{E2} are components of the inertial thrust direction vector, $\mathbf{u_E}$. In Section 4.2.1, the planar cartesian EOM were derived using the cosine and sine of the inertia thrust angle, ψ^i (defined in Section 3.4). Note that the following are equivalent:

$$\cos\psi^i = u_{E1} \tag{5.8}$$

$$\sin\psi^i = u_{E2} \tag{5.9}$$

The objective of the current research is to minimize fuel usage while meeting specified operational constraints. The cost function was chosen to be the final mass of the vehicle because this is the most direct measurement of fuel usage, as seen in Equation (5.10).

$$\mathcal{J}_{min} = \ -m(t_f) \tag{5.10}$$

Optimization routines run better if the parameters over which they are optimizing are normalized. For the translational motion analysis, the scaling factors chosen were the equatorial radius of the Moon, the Schuller period, and a mass of 1000 kg. The Schuller period is defined as the period of a circular orbit with a semi-major axis equal to the radius of the moon, as seen in Equation 5.12. The code was run with normalized parameters and later converted back to dimensional quantities during analysis.

$$\text{Distance Normalization Unit:} \quad DU_1 = R_{eq} \qquad = 1737.4\ km \tag{5.11}$$

$$\text{Time Normalization Unit:} \quad TU_1 = 2\pi\sqrt{\frac{R_{eq}^3}{\mu}} \qquad = 6498.43\ s \tag{5.12}$$

$$\text{Mass Normalization Unit:} \quad MU_1 \qquad = 1000\ kg \tag{5.13}$$

The vehicle parameters, as described in Section 3.7, are listed along with the initial conditions in Table 5.1. For simplicity, the vehicle is initialized along the inertial x-axis.

Table 5.1: Initial Conditions and Vehicle Parameters

Parameter	Value	Unit
T_{maxE}	8000	N
V_{exE}	3500	$\frac{m}{s}$
x_0	1777.4	km
y_0	0.0	km
v_{x0}	0.0	$\frac{m}{s}$
v_{y0}	1660	$\frac{m}{s}$
m_0	1800	kg

5.1.1 Baseline Trajectory (TM)

The first step in presenting results, which include only translational motion, is to define a baseline trajectory. This trajectory includes a minimal number of constraints in order to identify the undesirable characteristics of the trajectory, which are addressed in subsequent analysis by enforcing certain operational constraints.

The vehicle is initialized in a 40 km altitude circular orbit and descends to a soft landing. The main criterion is to land with zero velocity at the surface, while using bounded thrust. The vehicle must also remain above the surface of the Moon for the duration of the trajectory. The constraints on the system, in addition to the dynamical EOM listed in Equations (5.1) to (5.5), are as follows:

Initial Constraints

$$\mathbf{x}(t_0) = \mathbf{x}_0 \tag{5.14}$$

State Variable Bound

$$m(t) \geq m_{dry} \tag{5.15}$$

Control Variable Bounds

$$0 \leq k_E(t) \leq 1 \tag{5.16}$$

$$-1 \leq u_{E1}(t) \leq 1 \tag{5.17}$$

$$-1 \leq u_{E2}(t) \leq 1 \tag{5.18}$$

Path Constraints

$$x(t)^2 + y(t)^2 \geq R_{eq}^2 \qquad \textit{Above the surface} \qquad (5.19)$$

$$u_{E1}(t)^2 + u_{E2}(t)^2 = 1 \qquad \textit{Thrust Unit Vector} \qquad (5.20)$$

Terminal Constraints

$$x(t_f)^2 + y(t_f)^2 = R_{eq}^2 \qquad (5.21)$$

$$v_x(t_f) = 0 \qquad (5.22)$$

$$v_y(t_f) = 0 \qquad (5.23)$$

where $\mathbf{x}_0$ is the initial value of the state, using the values specified in Table 5.1.

$$\mathbf{x}_0^T = [\, x_0 \;\; y_0 \;\; v_{x0} \;\; v_{y0} \;\; m_0 \,] \qquad (5.24)$$

A total of 120 Nodes were used for the baseline case in order to capture the initial and final dynamics properly. A plot of the minimum fuel local optimal trajectory profile is displayed in Figure 5-1. As a feasibility check, the initial conditions are propagated forward using MATLAB's Runge-Kutta integrator (ode45), with the control sequence determined by DIDO. In using the integrator, the relative and absolute integration tolerances were set very low (1×10^{-13}), to obtain adequate accuracy. In Figure 5-1, the points represent the DIDO optimized solution and the solid line represents the propagated altitude and central angle.

An estimate of downrange distance is obtained by multiplying the central angle by the radius of the Moon. This scale is included at the top of Figure 5-1, where zero downrange represents the position of the landing point. The vehicle travels 4743 km around the Moon, while descending 40 *km*. The altitude vs. downrange for the final braking phase of the trajectory is shown in Figure 5-2.

Figures 5-1 and 5-2 are somewhat misleading in the flight path angle of the vehicle during final descent due to the scaling difference between altitude and downrange. It seems as though the vehicle lands with a vertical attitude, but in fact the trajectory is largely horizontal. The correct representation of the terminal final flight path angle is

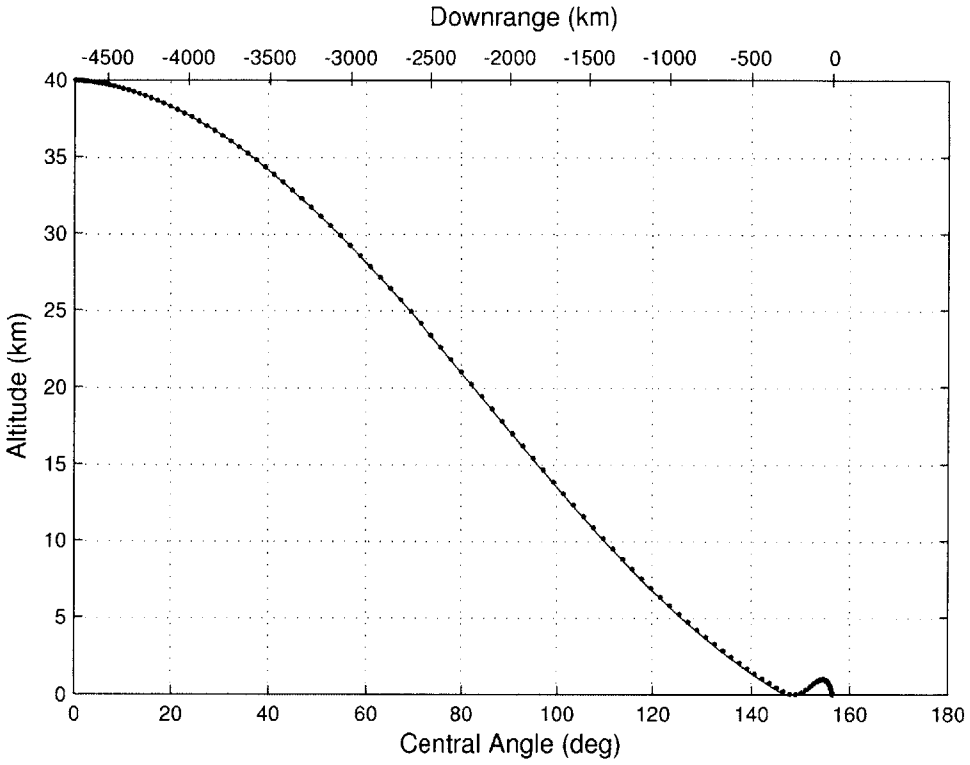

Figure 5-1: Baseline Trajectory Profile (TM)

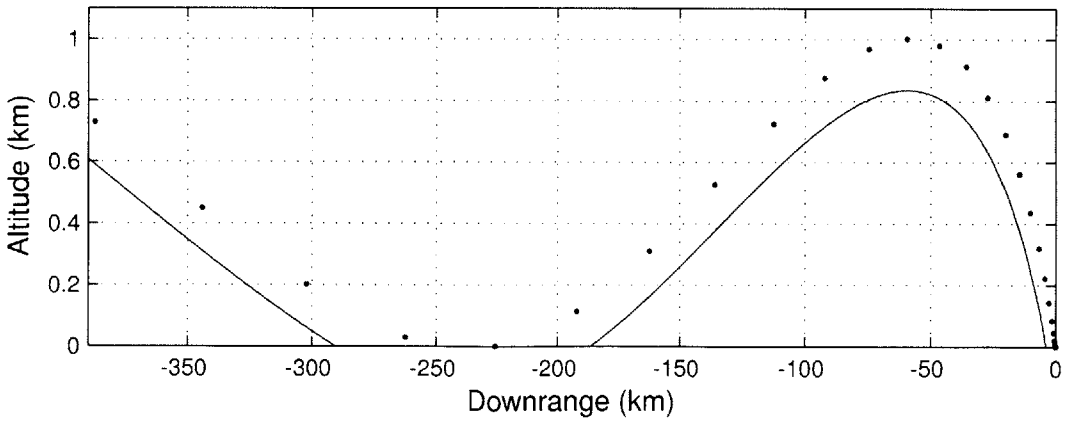

Figure 5-2: Baseline Altitude vs. Range during Final Braking Phase

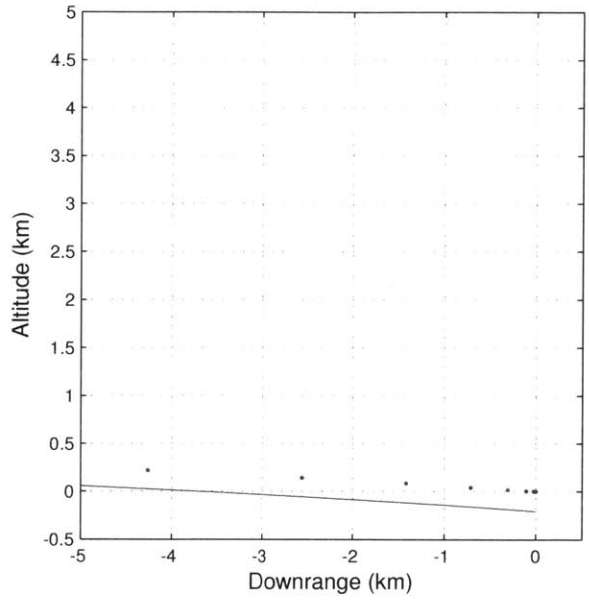

Figure 5-3: Baseline Altitude vs. Range (Equally Scaled Axes)

given in Figure 5-3, which has equally scaled axes. In this figure, zero downrange and zero altitude represents the position of the landing point.

The final value of the propagated altitude differs from the DIDO solution by 208 m, which is apparent in Figure 5-3. In normalized units, where the length scale is the radius of the Moon, this final propagation error corresponds to a value of 1.2×10^{-4}. The use of other MATLAB propagators was briefly investigated, such as ode113 and ode15s , but did not improve the solution significantly. The propagation error was seen to decrease with increasing nodes, which suggests that the solution is feasible, but differences in numeric integration techniques between the propagation and the spectral method are present. A plot of the final altitude propagation error vs. number of nodes is presented in Figure 5-4. However, there is a limit to the number of nodes which should be used in a trajectory with only one phase and no knots. This is because DIDO maps the time scale of the problem to an interval (-1,1) and the time intervals at the boundaries become smaller with increasing nodes. Increasing the nodes to 120, as used for the baseline case, reduces the time interval between the first and second node to 1.1953×10^{-16} on the mapped scale. Using more nodes only decreases this value and numerical errors begin to appear in the results. Adding knots mitigates this problem because each segment is mapped separately

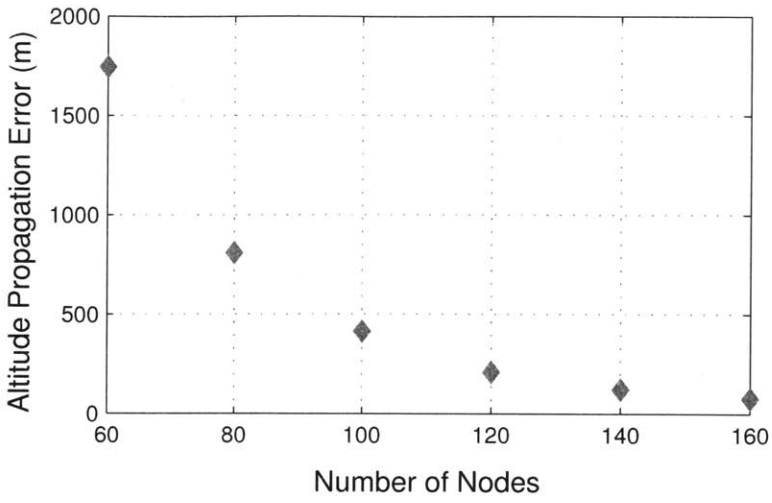

Figure 5-4: Final Propagation Error in Altitude

to the (-1,1) time span. Knots are added to this trajectory in subsequent analysis and a case with an increased total number of nodes will be presented.

A second source of error is due to the interpolation of the control. The DIDO solution is only given at discrete moments in time. In order to propagate the state forward from the initial values, it is necessary to interpolate the control at times between the node points. The interpolation schemes available in MATLAB include linear, cubic, and spline. A cubic interpolation scheme was found to most accurately fit the data. A linear interpolation scheme was not sufficient and a spline interpolater produced oscillations in the throttle at the switch, which is known as the Gibbs phenomenon. Using the cubic interpolation scheme introduces deviation between the propagation and the DIDO solution since two different approximation methods are used.

Details of the trajectory, including velocity components, throttle, flight path angle, etc., are plotted in Figures 5-5 and 5-6. Zoomed portions of the final 1.5 km of the trajectory (which encompasses the entire braking burn) are displayed in Figures 5-7 and 5-8. The zoomed graphs have a light grey background for quick distinction.

In Figure 5-5, altitude, central angle, and the horizontal and vertical components of velocity are plotted against time. It is important to note the difference in y-axis scales on the horizontal and vertical velocity plots. This trajectory is largely horizontal, having a maximum horizontal velocity of 1688 m/s which decreases rapidly once the final braking

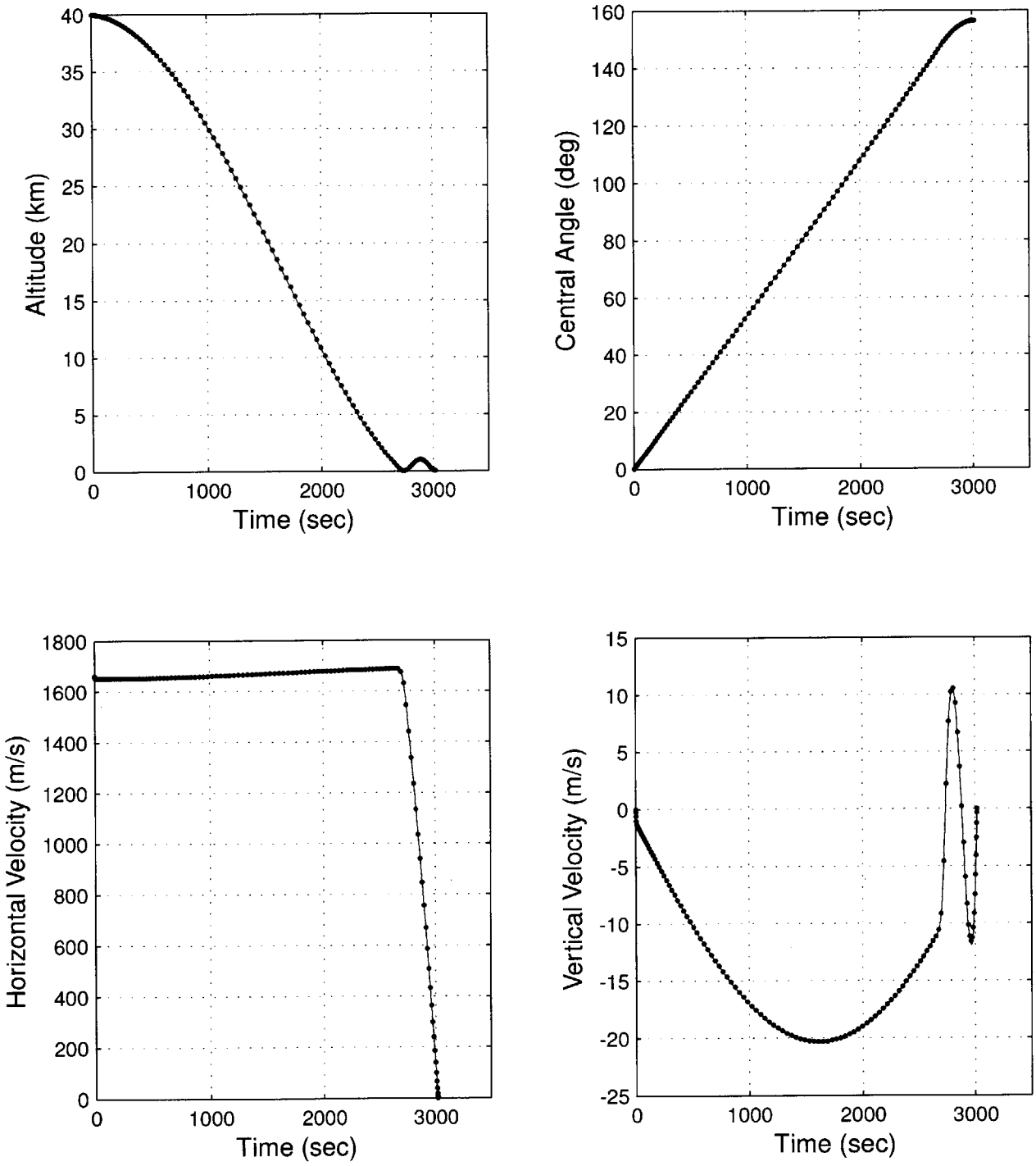

Figure 5-5: Baseline Trajectory Results (TM)

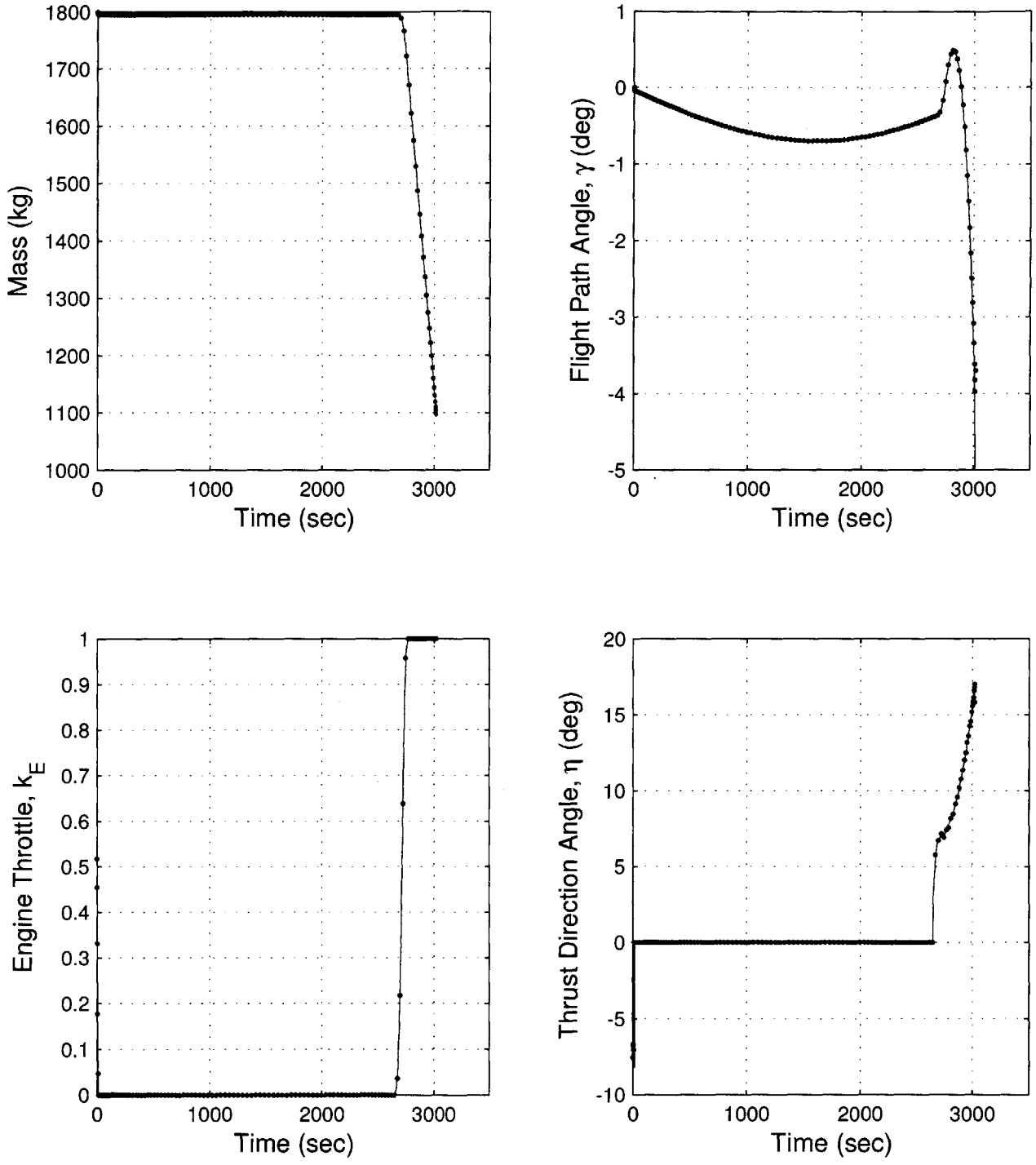

Figure 5-6: Baseline Trajectory Results (TM)

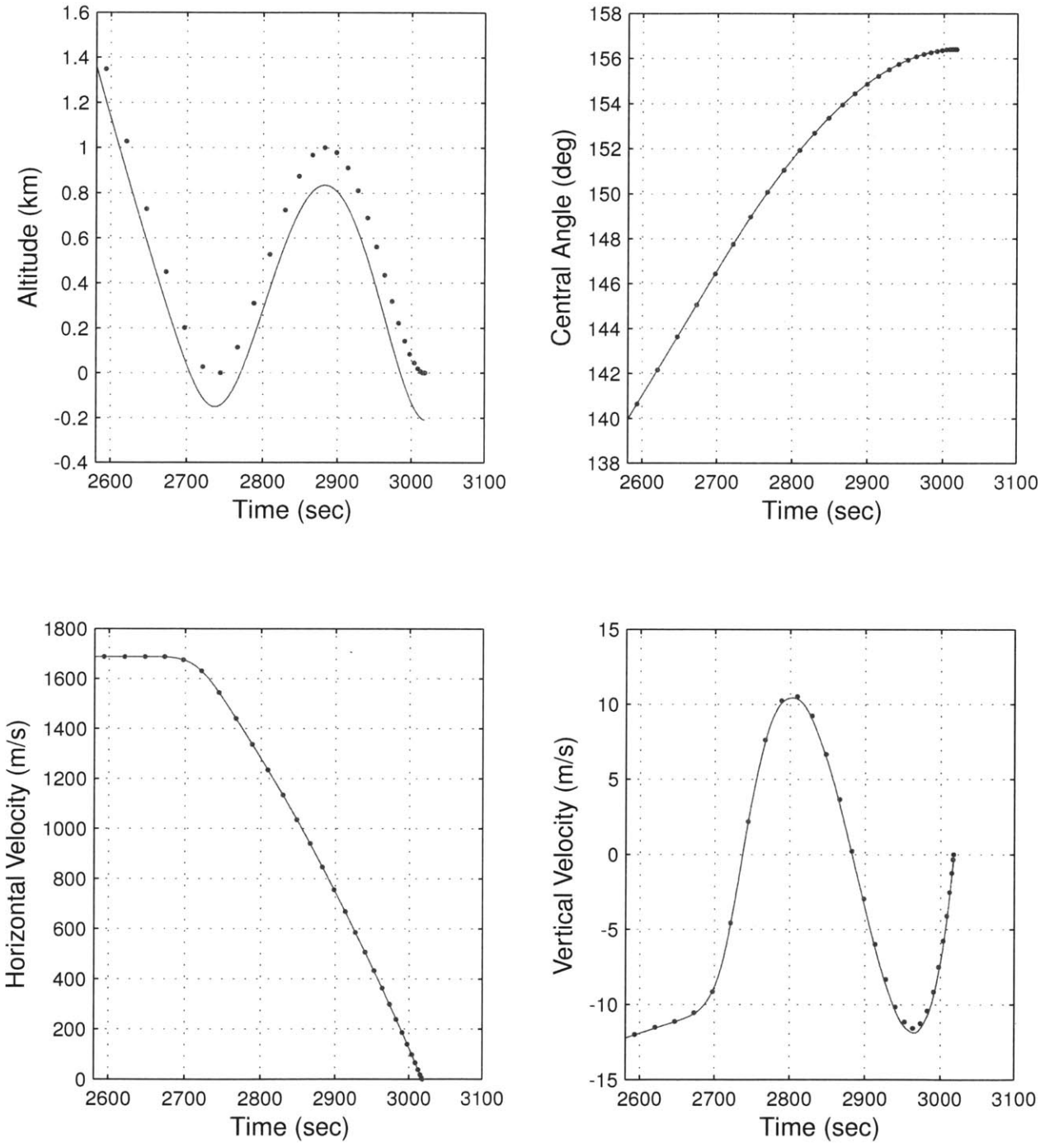

Figure 5-7: Baseline Trajectory Results (Starting from 1.5 km) (TM)

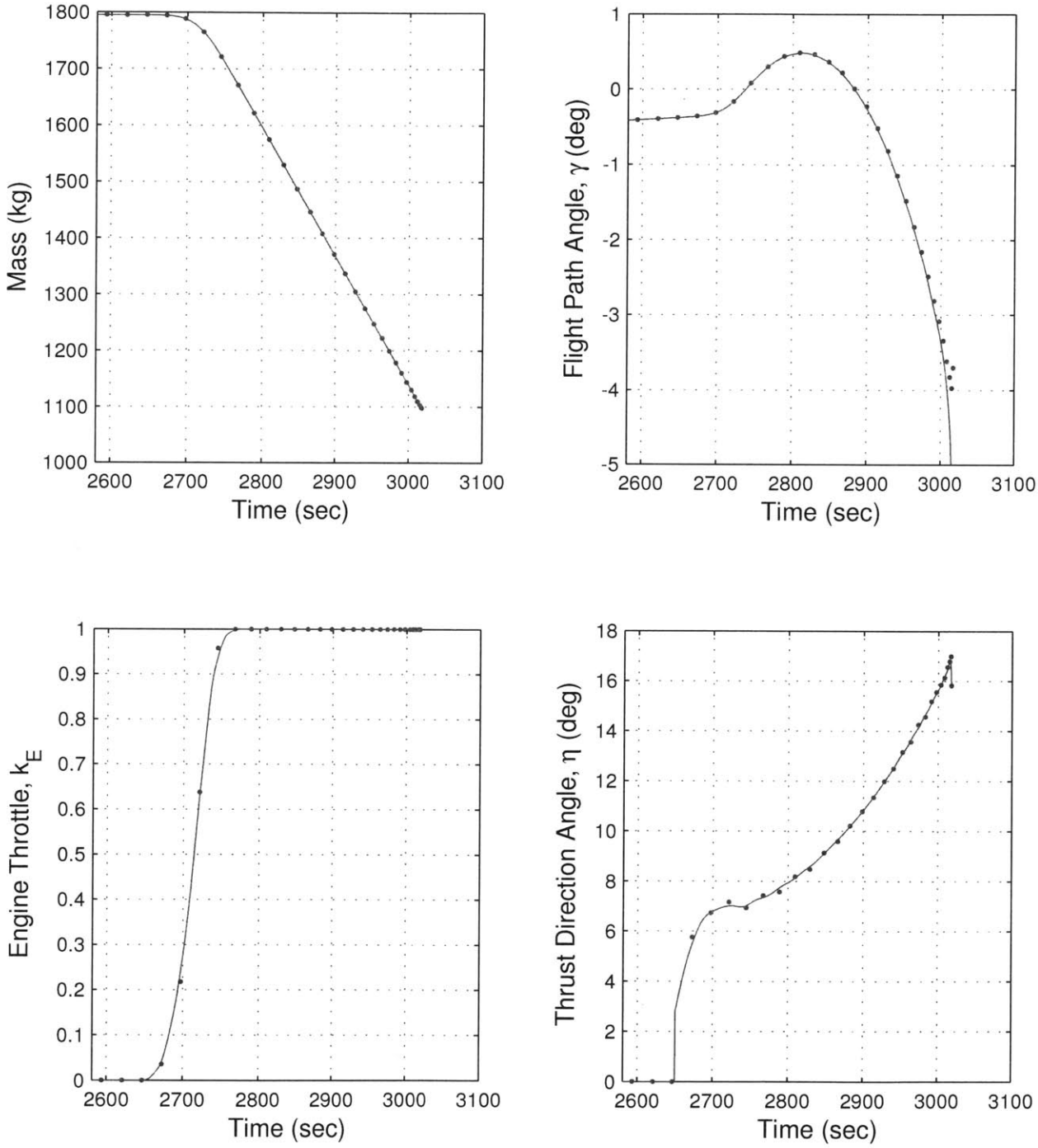

Figure 5-8: Baseline Trajectory Results (Starting from 1.5 km) (TM)

burn commences.

The throttle profile is presented in Figure 5-6, along with the mass history, flight path angle, and thrust direction angle. The throttle has a bang-off-bang profile, which is expected and consistent with Pontryagin's Minimum Principle (Equation (2.30)). The initial de-orbit burn has a duration of 14.31 s, followed by a descent coast of 2632.8 s, and a final braking burn for 370.9 s. The trajectory required 702.3 kg of fuel. In terms of ΔV, which is the integral of thrust acceleration magnitude, as defined in Equation (5.25), this corresponds to 1732 m/s.

$$\Delta V = \int_{t_0}^{t_f} |\, a|\, dt = \int_{t_0}^{t_f} \frac{T_{max,E}\ k_E}{m}\, dt \tag{5.25}$$

A noticeable characteristic of the trajectory is that it flies very close to the surface before touchdown. This is clear from the altitude vs. downrange plot of the final braking burn in Figure 5-2. The vehicle travels 390 km downrange, while remaining within 1 km of the surface. In Figure 5-7, it can be seen that the vehicle actually touches the surface at 2744.8 s, which is 97.7 s after the braking burn begins and the horizontal velocity is 1544 m/s.

The altitude of the vehicle is increased before the final descent and touchdown, which is referred to as "lofting" in this thesis. This lofting is present when the final burn is initiated close to the target altitude (*i.e.*, within a few kilometers). For the baseline case, thrusting is initiated when the vehicle is at an altitude of 0.73 km above the surface. The velocity components at this point are -11 m/s vertical and 1688 m/s horizontal. If the vertical descent of the vehicle is not altered, it would land approximately 66 seconds later, not accounting for the extra acceleration the vehicle would undergo due to gravity. In order to stop the horizontal motion of the vehicle before it reaches the surface, the vehicle would need to apply an acceleration of at least 25.6 m/s^2, which is above the capability of the engine. The trajectory must loft (increase in altitude) to gain the time required to zero the horizontal velocity. Having a large horizontal velocity close to the surface is an operational hazard and a highly undesirable characteristic of this local optimal solution.

The flight path and thrust direction angles, which were defined in Section 3.4, are

plotted in Figure 5-6. For this planar motion analysis, the thrust yaw angle remained 180 *deg*. Therefore, only the thrust pitch angle, η (also referred to as the thrust direction angle), is displayed. When the engine is off, the thrust direction angle is not defined for TM analysis. The flight path angle starts at zero when in a circular orbit about the Moon. Due to the large horizontal velocity component, the flight path angle remains between 0 and -1 *deg* until the braking burn is initiated. The flight path angle is seen to decrease only marginally during the end of the trajectory, since the trajectory is largely horizontal at landing. The final relevant value of the flight path angle is approximately -3.4 *deg*.

During the final braking burn, the thrust direction angle has nearly the same pitch as the flight path angle, only slightly more vertical. This is apparent in Figure 5-8. Given that the thrust vector has a yaw of 180 *deg*, the vehicle is thrusting opposite the velocity and slightly vertical to counteract gravity. This is an intuitively correct result. Also note the almost linear trend in the thrust direction angle profile during the braking burn, which is consistent with optimal control theory in a uniform gravity field [22].

The descent orbit perilune height (DOPH) for this trajectory is -2.7 *km* relative to the surface, which means that the vehicle is on a collision course with the Moon during the descent and braking phases. From an operational standpoint, this is undesirable since the vehicle will collide with the surface if engine ignition failure were to occur and the final burn is not initiated. It is customary to design a trajectory that has a descent orbit which will remain above the surface of the Moon for this reason.

Optimality of the Baseline Solution

The optimality conditions of the baseline solution is investigated next. The DIDO estimates of the Hamiltonian and costate components for the baseline trajectory are displayed in Figure 5-9. Using Equation (2.20), the Hamiltonian is found to have the following form:

$$\begin{aligned}\mathcal{H} = \lambda_x(v_x) + \lambda_y(v_y) + \lambda_{v_x}\left(-\frac{\mu}{r^3}\,x + \frac{T_{maxE}\,k_E}{m}\,u_{E1}\right) \\ + \lambda_{v_y}\left(-\frac{\mu}{r^3}\,y + \frac{T_{maxE}\,k_E}{m}\,u_{E2}\right) + \lambda_m\left(-\frac{T_{maxE}\,k_E}{V_{exE}}\right) \\ + \mu_1\left(R_{eq}^2 - (x^2+y^2)\right) + \mu_2\left(1 - (u_{E1}^2 + u_{E2}^2)\right) \quad (5.26)\end{aligned}$$

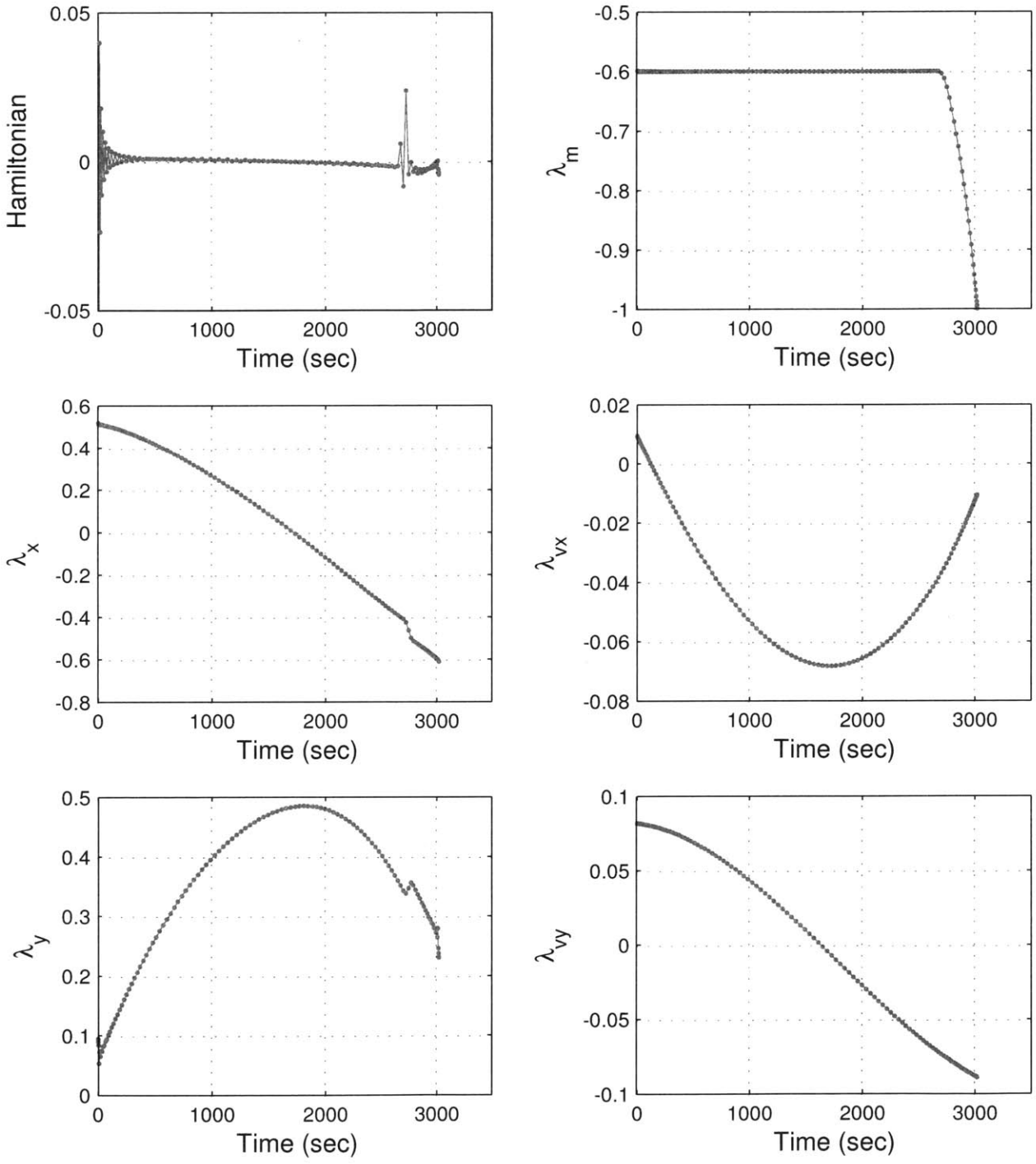

Figure 5-9: Baseline Trajectory Hamiltonian and Costate Components

where $\lambda_{(\ )}$ is the costate component of the corresponding state component and the variables μ_1 and μ_2 are constraint multipliers.

The DIDO estimate of the Hamiltonian, which is seen in Figure 5-9, has similar characteristics to the estimated Hamiltonian of the vertical descent example problem given in Section 2.2. Since the Hamiltonian is not a function of time, it should be constant. The DIDO estimate is fairly flat and is small in magnitude, but it is not constant. Large oscillations are seen at the end points of the time span, with a larger fluctuation seen at the location of the control discontinuity. Overall, the DIDO estimates of the costate and Hamiltonian, for this baseline case, are well behaved.

5.1.2 Baseline Trajectory with Knots (TM)

From previous sections it was seen that there is a limit to the number of nodes that can be placed in the problem. In order to accurately capture the discontinuities in the throttle and increase the concentration of nodes during times of non-zero thrust, the problem is segmented into three phases through the inclusion of two knots. One knot is placed near the end of the de-orbit burn and the other is placed near the beginning of the braking burn, but each is free to move as determined by the optimizer. The number of nodes in the respective phases are 60, 40, and 60, which places a much higher concentration of nodes in the first and last segments of the trajectory.

Event constraints are added to equate the state at the knot locations, while the control is allowed to be discontinuous. The throttle is set to zero during the descent orbit coast, by equating the upper and lower throttle bounds in the middle segment of the trajectory. The constraints listed below, in addition to the equations of motion, the initial and terminal conditions (Equations (5.14) to (5.15)), and the path constraints (Equations (5.19) and (5.20)), complete the system of equations for the optimal control problem. The variables

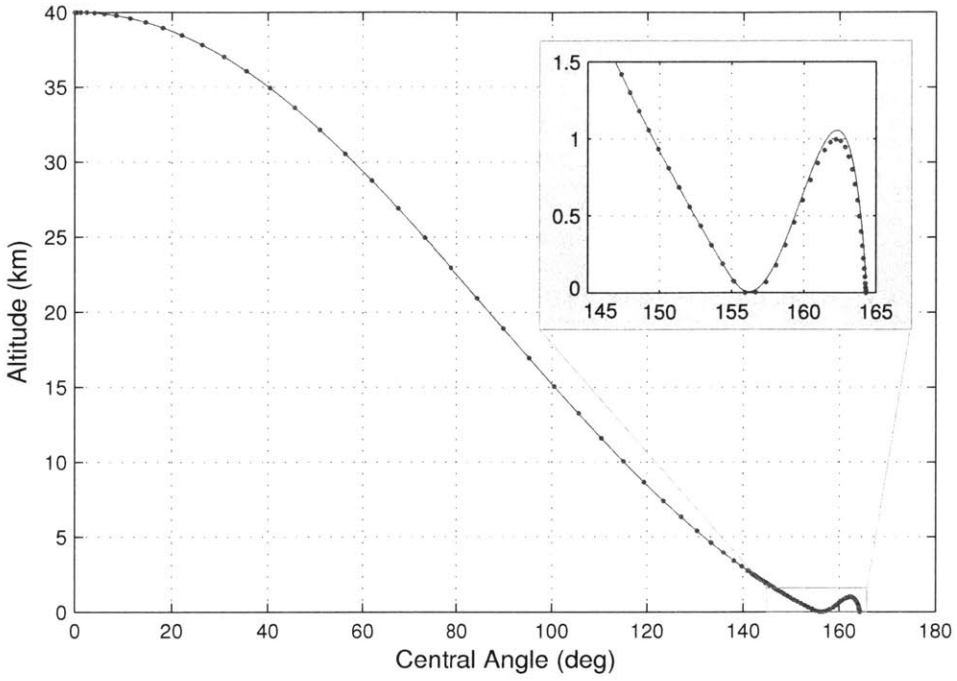

Figure 5-10: Baseline Trajectory Profile with Knots (TM)

t_1 and t_2 represent the time locations of the first and second knot, respectively.

Throttle Bounds

$$0 \leq k_E(t) \leq 1 \qquad \textit{De-orbit Phase} \quad (t_0 \leq t \leq t_1) \tag{5.27}$$

$$k_E(t) = 0 \qquad \textit{Descent Coast Phase} \quad (t_1 \leq t \leq t_2) \tag{5.28}$$

$$0 \leq k_E(t) \leq 1 \qquad \textit{Braking Phase} \quad (t_2 \leq t \leq t_f) \tag{5.29}$$

Event Constraints

$$\mathbf{x}^-(t_1) = \mathbf{x}^+(t_1) \tag{5.30}$$

$$\mathbf{x}^-(t_2) = \mathbf{x}^+(t_2) \tag{5.31}$$

$$t_0 < t_1 < t_2 < t_f \tag{5.32}$$

Equations (5.27) - (5.29) set the throttle bounds in each phase and replace Equation (5.16). The state is equated at the knot with Equations (5.30) and (5.31), where the superscripts $(\,)^-$ and $(\,)^+$ denote the values of the state just prior to and after the knot, respectively. The final constraint ensures that events are sequential.

The results for the local optimum minimum fuel trajectory, including two knots, is displayed in Figure 5-10, with a zoomed portion of the final 1.5 kilometers. In the figure, the points represent the DIDO optimized solution and the solid line represents the propagated altitude and central angle. The results are very similar to the baseline case without knots. Details of the trajectory are plotted in Figures 5-11 and 5-12, with the last 1.5 km of the trajectory (covering the entire braking burn) plotted in Figures 5-13 and 5-14.

The initial de-orbit burn has a duration of 2.2 s, which is much shorter than the in the case without knots, which had de-orbit burn of 14.31 s. The de-orbit burn is characterized by a short maximum thrust burn, but is ill-defined in the case without knots since a discontinuity in the control is not allowed. A longer, smaller magnitude burn is instead seen. Defining short, impulsive-like burns and throttle switches are two of the main advantages of adding knots.

For the case with knots, the de-orbit burn was followed by a descent coast of 2841.2 s, and a final braking burn for 290.9 s. Adding knots increased the total duration of the trajectory by 144 s. The trajectory required 702.2 kg of fuel, which corresponds to a ΔV requirement of 1730.5 m/s and is slightly less than the case without knots. The DOPH for this trajectory is -1.8 km relative to the surface, which is similar to the perilune height previously reported as -2.7 km. The new value obtained for the perilune height, -1.8 km, is thought to be a better estimate of the optimal solution because the trajectory is more clearly defined.

The baseline case with knots is also seen to have a more distinct switch in the throttle at the initiation of the braking burn. The transition from minimum throttle to maximum throttle takes only 28.2 seconds. This is compared to the baseline without knots case that took 120.1 seconds to make the transition.

The altitude propagation error for this trajectory is 107 m, which is a decrease in error by 49% from the case without knots. A decrease is expected because there are more nodes concentrated in the higher dynamical segments of the trajectory. It is interesting to note that in this case with knots, the altitude error biases the trajectory upwards, where in the original case without knots, the propagation was below the DIDO solution.

One of the disadvantages of this new trajectory is that spikes are seen in the thrust

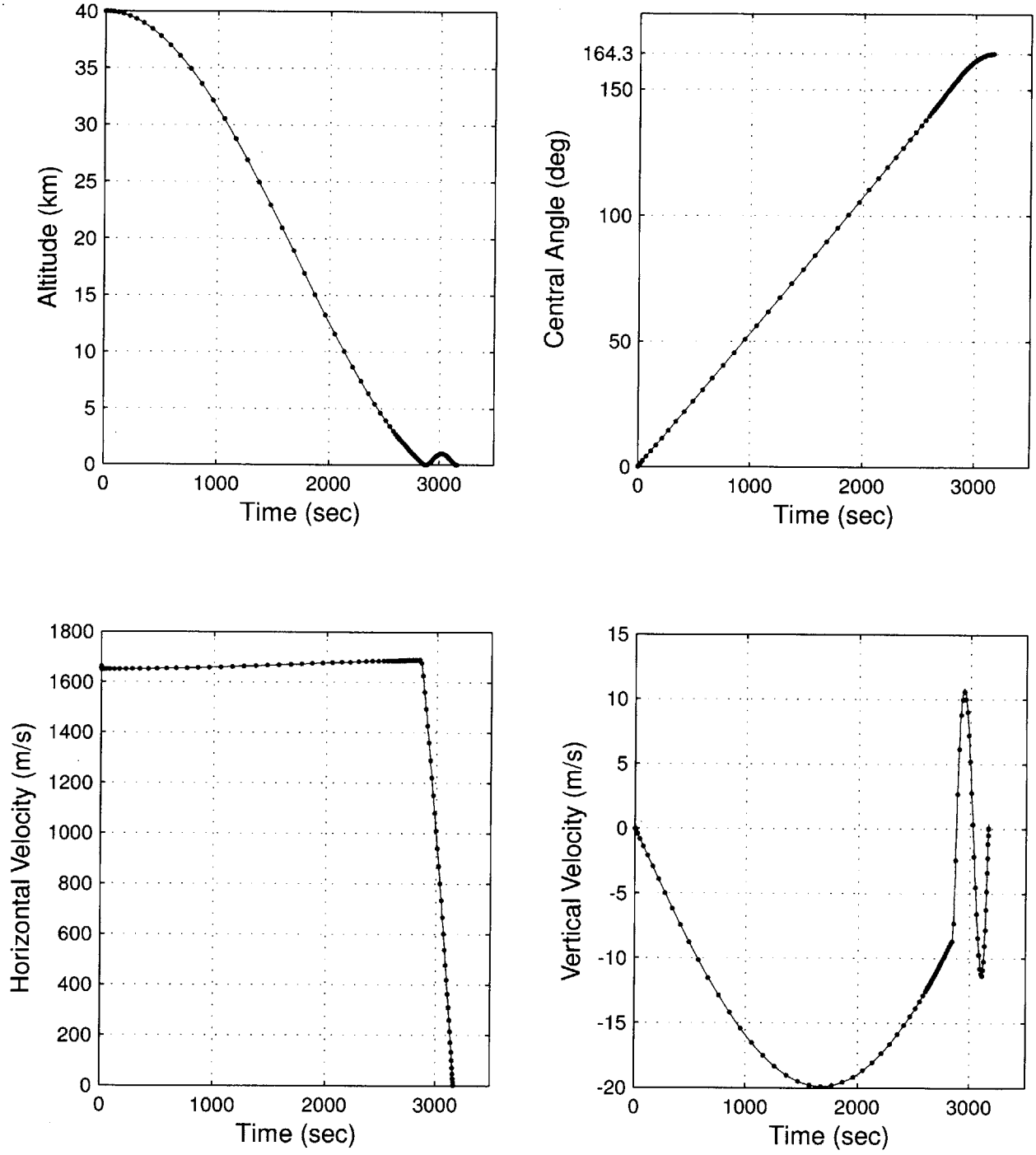

Figure 5-11: Baseline Trajectory Results with Knots (TM)

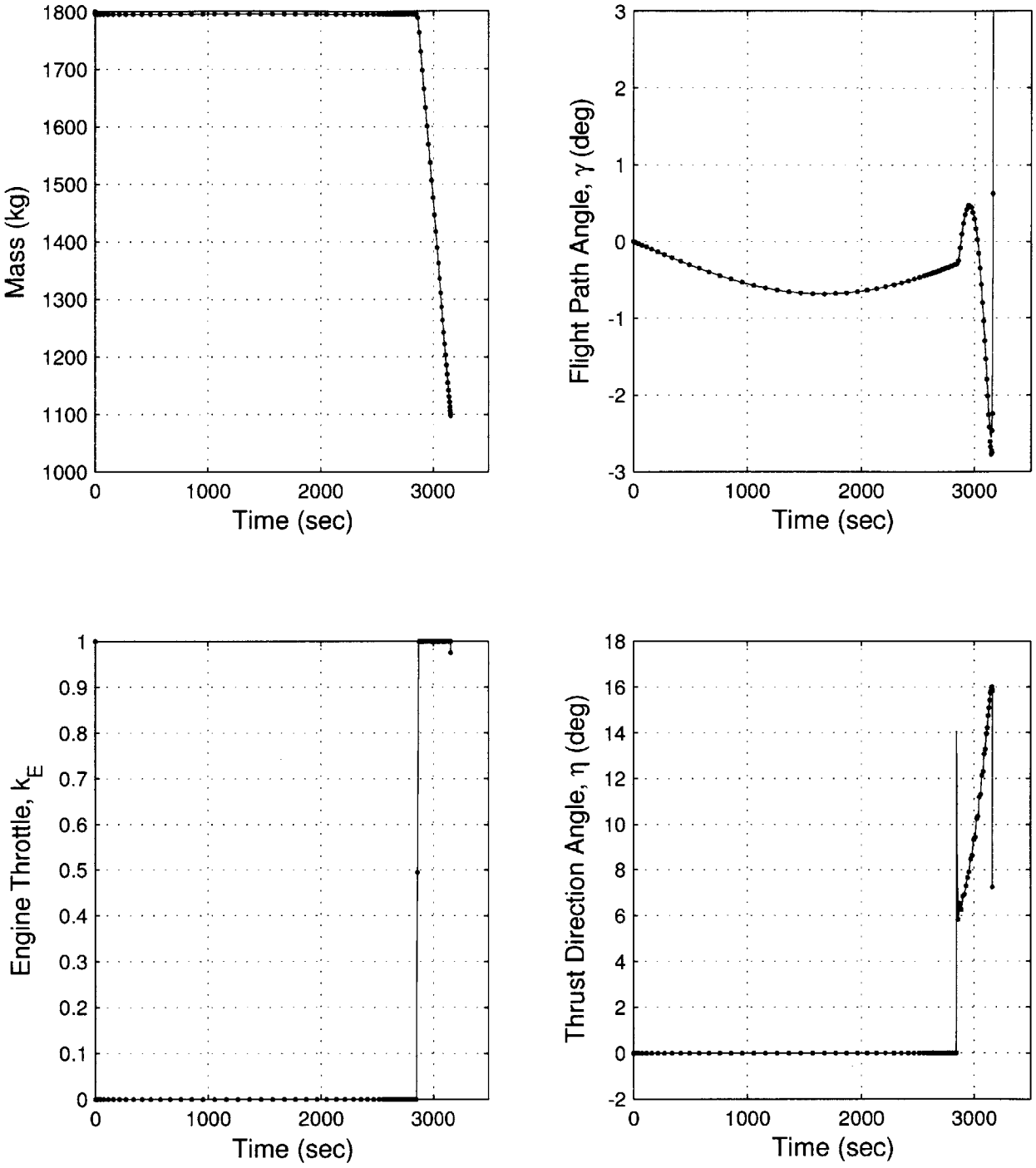

Figure 5-12: Baseline Trajectory Results with Knots (TM)

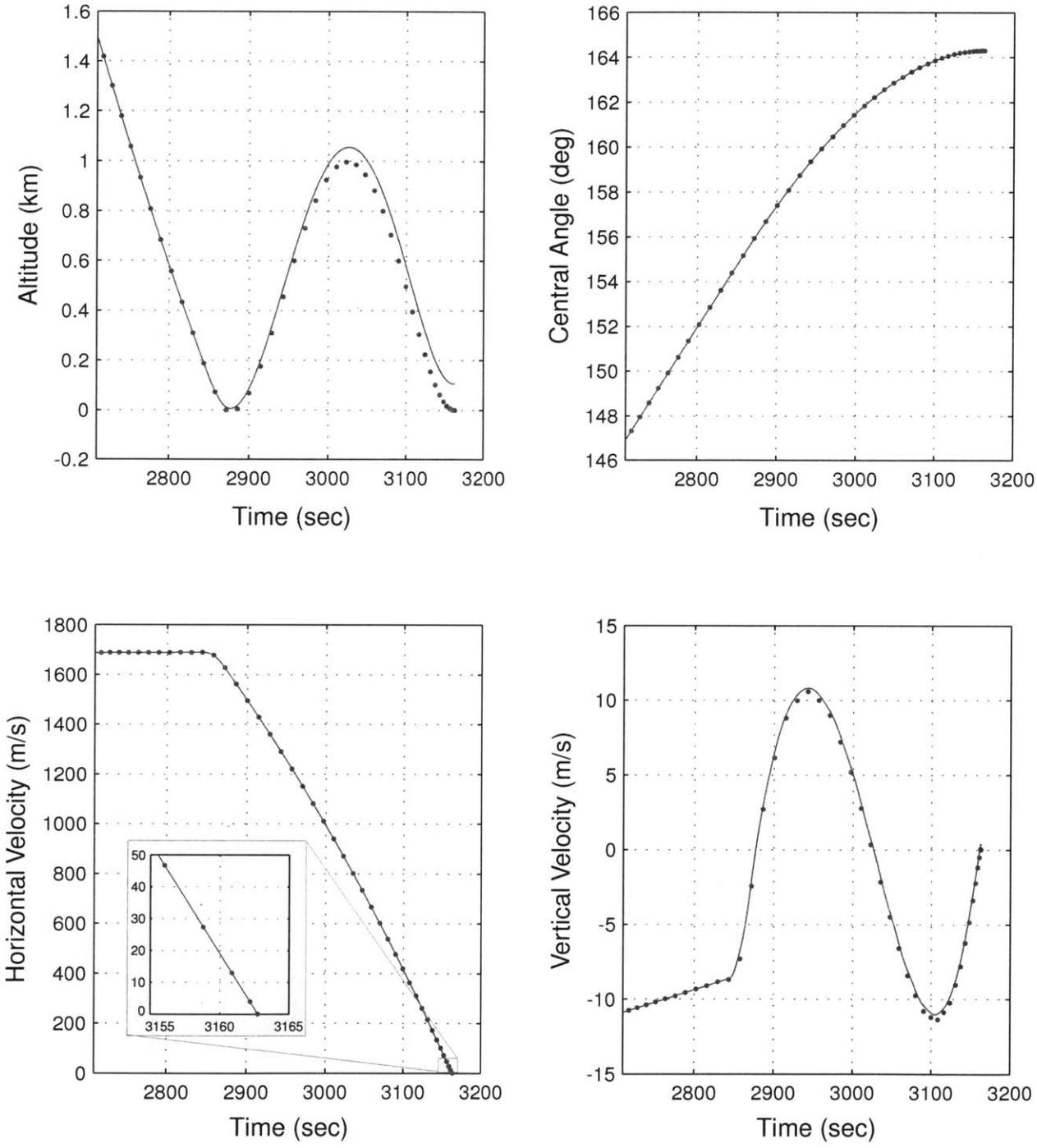

Figure 5-13: Baseline Trajectory Results with Knots (Starting from 1.5 km) (TM)

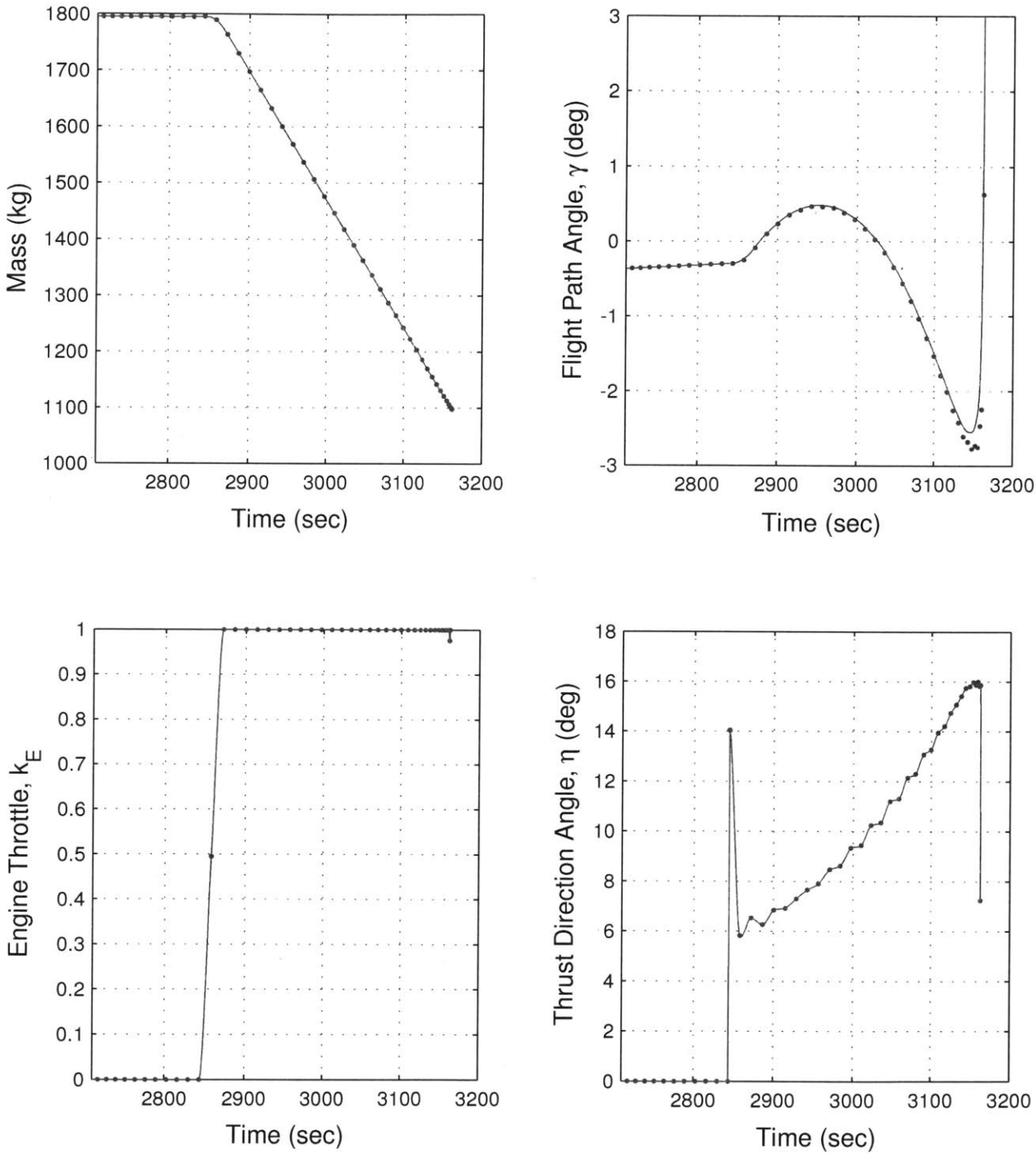

Figure 5-14: Baseline Trajectory Results with Knots (Starting from 1.5 km) (TM)

direction angle at the beginning of the braking phase and at landing. These spikes are clearly noticeable in Figure 5-14. The first spike is because the control is allowed to be discontinuous at the knot location. The first value is seen to deviate from the general trend of the solution. The second spike may be an artifact of the current implementation of DIDO as the control at the endpoints of the time-span are less well-behaved.

By adding knots to the trajectory, the optimizer is able to capture control discontinuities and switch location more accurately. The total number of nodes can be increased and a higher concentration of nodes can be placed where more dynamics are present. As a result, the propagation errors are seen to decrease.

Summary of Baseline Results

In this section, the baseline trajectory was calculated with and without the implementation of knots. In both cases, the baseline trajectory is impractical for the following reasons: first, the DOPH is below the surface (by 1.8 km for the case with two knots). This is dangerous since the vehicle will collide with the surface if the final burn is not initiated. Secondly, the trajectory is extremely shallow (horizontal) close to the surface and actually touches the surface prior to final impact. The vehicle is seen to travel a downrange distance of 390 km while having an altitude of no more than 1 km. This is highly undesirable from an operational point of view and is a safety hazard due to the variations in the lunar terrain. Furthermore, the flight path angle, which is related to this horizontal profile, is also nearly horizontal at landing. A vehicle with this trajectory would have minimal time to view the actual landing site upon approach. Instead, it is desired that the vehicle descend with zero horizontal and non-zero vertical velocity. Lastly, assuming that the thrust is fixed to the body of the vehicle, the terminal attitude of the vehicle is almost completely horizontal and the vehicle does not land with a "legs down" orientation. Because of these considerations, this baseline trajectory is not a viable solution from an operational standpoint. It represents a trajectory that could be obtained if optimization techniques are used for trajectory design with only minimal constraints included. Operational constraints are added next to address some of these issues and obtain a viable solution. The framework with the two knots presented above is used in

subsequent analysis.

5.1.3 Inclusion of Selected Operational Constraints (TM)

In the previous section a baseline trajectory was identified, but this trajectory had undesirable operational characteristics. In the following section, constraints are added based on operational considerations, such as the DOPH and a terminal near-zero vertical velocity. Also considered is the total number of finite engine burns, which is constrained by imposing a non-zero lower throttle limit. The objective is to obtain an operationally viable solution, and to investigate the individual effects of these constraints on the overall trajectory, control behaviors, and fuel requirements. These effects are investigated through a parametric study and the constraints are discussed next, starting with the DOPH.

The main operational constraint considered in this section of the thesis is the DOPH. This parameter was constrained by placing an event constraint at the terminus of the de-orbit phase. During the de-orbit burn, the main engine burns until a desired perilune height is obtained. The coast phase is initiated by constraining the throttle to zero, which prevents the perilune height from being altered during the intermediate descent coast. The vehicle follows the descent coast trajectory until the altitude is below a specified value (to be discussed shortly) and the braking phase begins. A diagram of the throttle bounds can be seen in Figure 5-15.

It was found necessary to bound the descent orbit coast by event constraints on both ends of the segment. By specifying a desired DOPH and then constraining the throttle to zero, at attempt is made to force a less-optimal value for the DOPH. If a finite duration of the descent coast phase is not also enforced, the optimizer shrinks the descent coast phase (which has constrained throttle region) to zero. After the de-orbit burn reduces the perilune height of the orbit to the desired parametric value, the optimizer immediately transitions to the braking phase in order to continue thrusting and achieve the optimal perilune for the coast phase. The trajectory is seen to continue thrusting till the optimal DOPH of -1.8 km is reached and then continues with a trajectory similar to the baseline trajectory.

The descent coast phase is initiated when the perilune height of the orbit decreases to

a desired value, r_{pC}, which is varied in the parametric study. The end of the descent coast phase is bounded above by a radius constraint, namely $(x(t_2)^2 + y(t_2)^2 \leq r_2^2)$. This means that the vehicle cannot terminate the coast and begin the final descent until the altitude of the vehicle is below a specified value, r_2. A value of 20 km was chosen in order enforce a coast down to the 20 km altitude, but not further constrain the initiation altitude of the braking burn. Note that r_2 cannot be set below the desired parametric DOPH, because this would cause an infeasibility in the solution. As a result, in the cases which targeted 20, 25, and 30 km, r_2 was set 5 km above the DOPH of the individual case (*i.e.*, 25, 30, and 35 km, respectively). Lowering the r_2 value for any case did not have an effect on the overall performance of the trajectory (except to enforce a coast). Only when set so low that it over constrained the problem, or made the problem infeasible, did this constraint cause an issue. In order to target a specific perilune height and enforce a coast, the event constraints listed below are added to the system at the knots locations t_1 and t_2. Note that the calculation of perilune radius, r_p, is given in Equation (3.9).

$$r_p(t_1) = r_{pC} \tag{5.33}$$

$$x(t_2)^2 + y(t_2)^2 \leq r_2^2 \tag{5.34}$$

Figure 5-15 also displays the number of nodes for each phase (bottom of figure). Note that this parametric study is referred to as the "open throttle cases" because thrust is allowed to vary between 0 and 1 during the de-orbit and braking thrust arcs. For the coast and braking phase, the number of nodes were decreased to 30 to reduce the computation time of the parametric study. Reducing the number nodes in each phase, while keeping the nodes concentrated in high dynamical regions, seemed to have minimal effect on the final results. A total number of 100 nodes was found to be sufficient for the parametric study.

A plot of the resulting trajectory profiles for each targeted perilune height is given in Figure 5-16. The dashed lines in the figure represent the 5 km incremental targeted perilune heights. Notice that trajectory lofting is manifested only in cases of non-positive targeted perilune height. It was not determined at exactly which altitude the trajectory

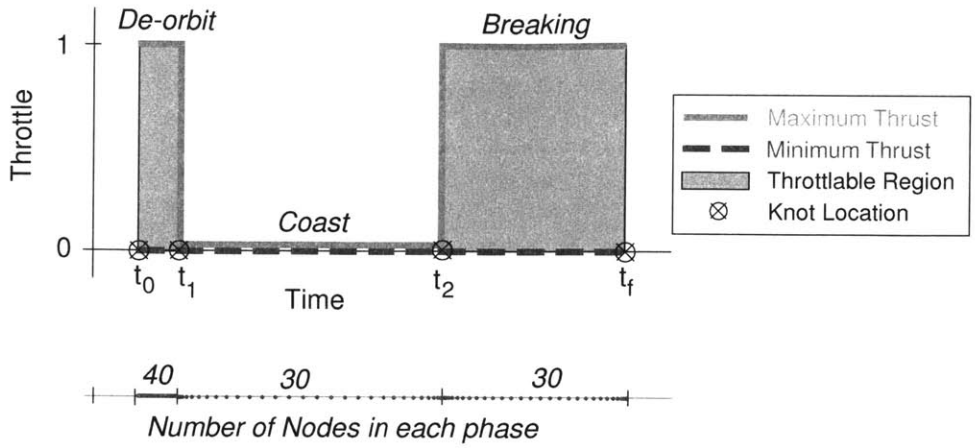

Figure 5-15: Throttle Bounds and Number of Nodes for Open Throttle Cases

begins exhibiting lofting, however the results suggest a gradual transition. Tabulated data for this parametric study is given in Tables 5.2 and 5.3. Total ΔV and fuel requirements are summarized in Figures 5-23 and 5-24.

Taking the 20 km case as an example, the throttle profile is plotted in Figure 5-17. The trajectory for this example case required 704.0 kg of fuel (1737.3 m/s ΔV), which is 1.8 kg (6.8 m/s) above the baseline trajectory fuel and ΔV requirements, respectively. The optimizer initiated the braking phase for the 20 km case at 2248 s. Instead of a continuous thrust to the ground, a short impulse-type burn is seen, followed by another coast phase, before the final braking burn commences. This short impulse-type burn changes the targeted perilune height to a subsurface value, which is more cost effective than burning continuously to the ground. The duration and ΔV of the impulse-type burns for each targeted perilune height case is listed in Tables 5.2 and 5.3, as well as the altitude at which it occurs and the incremental change in targeted perilune height due to the burn. Only for cases where the DOPH is above the surface is this impulse-type burn present in the throttle command. For comparison, the throttle profile for the -10 km targeted perilune height case is displayed in Figure 5-18. Notice that there is no intermediary impulsive-like burn.

From an operational standpoint, it is safer to have continuous thrust during the braking burn to eliminate engine restart failure. As a result, a continuous burn was enforced by constraining the vehicle throttle to remain above a lower limit once the braking burn is

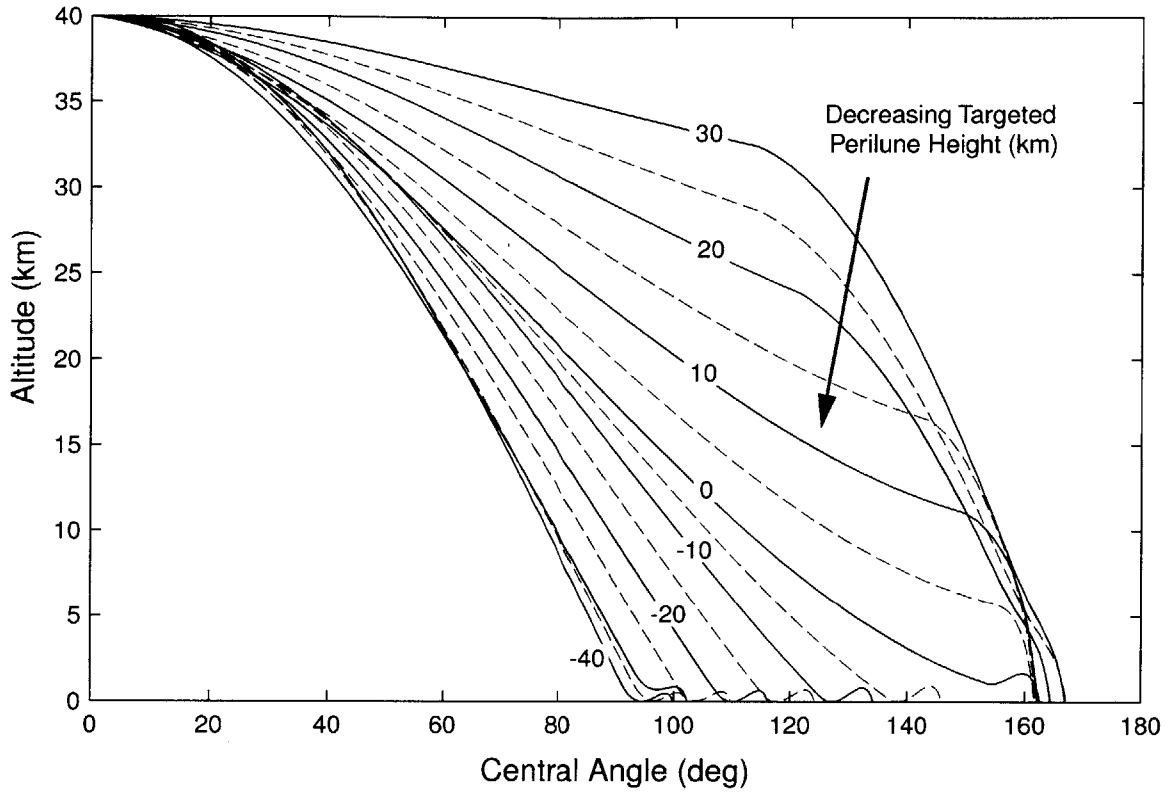

Figure 5-16: Open Throttle DOPH Parametric Study (TM), Dashed lines represent increments of 5 km

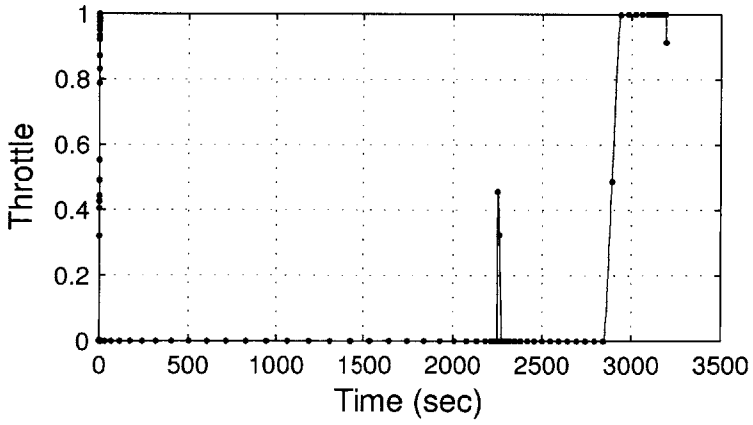

Figure 5-17: Throttle Profile (20 km Target Perilune Height)

Table 5.2: Open Throttle during De-orbit and Braking Phases, Tabulated Data A

Perilune Altitude km	Normalized Cost -	De-orbit ΔV m/s	Impulsive ΔV m/s	Braking ΔV m/s	Δh_p due to Impulse km
30	-1.095573	2.39	33.02	1704.62	-126.39
25	-1.095896	3.59	28.22	1707.14	-104.05
20	-1.096005	4.78	30.89	1701.58	-109.88
15	-1.095191	6.08	92.33	1640.10	-322.24
10	-1.095824	7.34	105.00	1623.63	-355.48
5	-1.096936	8.59	5.52	1718.12	-2.06
0	-1.097713	9.77	-	1719.90	-
-5	-1.097625	10.73	-	1719.26	-
-10	-1.097424	11.88	-	1718.70	-
-15	-1.097228	13.10	-	1718.10	-
-20	-1.097049	14.32	-	1717.45	-
-25	-1.096914	15.53	-	1716.69	-
-30	-1.096777	16.77	-	1715.92	-
-35	-1.096628	18.03	-	1715.12	-
-40	-1.096471	19.36	-	1714.27	-

Table 5.3: Open Throttle during De-orbit and Braking Phases, Tabulated Data B

Perilune Altitude km	De-orbit Duration s	Coast Duration s	Impulsive Duration s	2^{nd} Coast Duration s	Braking Duration s	Impulsive Altitude km	Braking Altitude km
30	0.57	2119.1	33.35	739.22	360.0	32.514	10.585
25	0.85	2125.7	33.01	731.70	356.3	28.733	8.753
20	1.24	2246.5	27.85	569.58	348.5	24.017	9.004
15	1.42	2648.5	37.55	119.60	337.3	16.564	13.168
10	1.69	2747.2	86.88	0	301.9	11.174	10.104
5	1.98	2784.7	9.76	0	321.6	6.079	6.023
0	2.89	2816.9	-	-	307.2	-	1.123
-5	2.50	2503.7	-	-	320.9	-	0.418
-10	2.74	2304.7	-	-	307.3	-	0.403
-15	3.07	2121.0	-	-	310.1	-	0.637
-20	4.02	1969.8	-	-	314.2	-	0.909
-25	3.76	1856.4	-	-	310.2	-	1.044
-30	4.09	1715.6	-	-	314.7	-	2.120
-35	4.44	1710.9	-	-	316.4	-	1.578
-40	6.41	1679.1	-	-	308.0	-	1.376

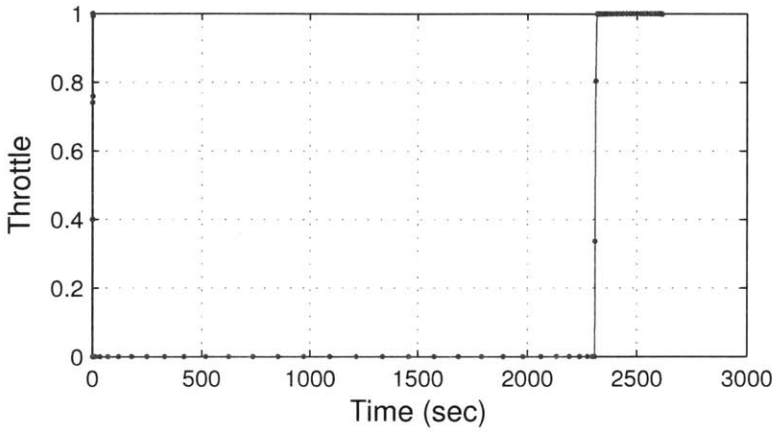

Figure 5-18: Throttle Profile (-10 km Target Perilune Height)

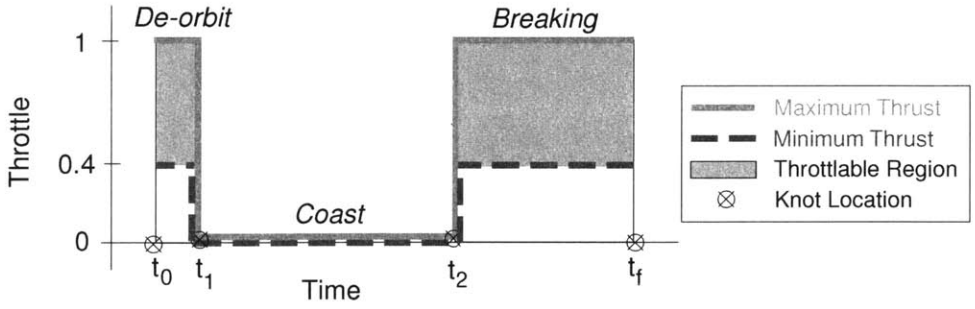

Figure 5-19: Throttle Bounds for Continuous Thrust Cases

initiated, as shown in Figure 5-19. When designing for a specific mission, the minimum throttle of the main engine should be used for the lower limit. A value of 40% was chosen for the purposes of this study to show general trends. A throttle command of 0.4, at the initiation of the braking burn, corresponds to approximately 1.10 lunar g's. Note that the number of nodes in each phase remained unchanged from Figure 5-15. The throttle bounds seen in Equations (5.27) - (5.29) were changed to:

$$0.4 \leq k_E(t) \leq 1 \quad \textit{De-orbit Phase} \quad (t_0 \leq t \leq t_1) \tag{5.35}$$

$$k_E(t) = 0 \quad \textit{Descent Coast Phase} \quad (t_1 \leq t \leq t_2) \tag{5.36}$$

$$0.4 \leq k_E(t) \leq 1 \quad \textit{Braking Phase} \quad (t_2 \leq t \leq t_f) \tag{5.37}$$

The fuel optimal trajectories obtained with the continuous thrust condition can be seen in Figure 5-20. Notice the difference in trajectories for the 30 km to 20 km cases from the corresponding cases in Figure 5-16. In the continuous thrust cases (Figure 5-20), the braking burn is initiated within 2.2 km above the perilune altitude and the vehicle's engine continues to burn until the vehicle reaches the surface. This causes a more rapid decrease in altitude. Note that Figure 5-20 is misleading in the final descent flight path angle because of scaling difference between altitude and central angle. In the left plot of Figure 5-21, the correct representation of the final approach of the vehicle is illustrated. In this figure, four DOPH cases are included for clarity and the touchdown location is at zero altitude and zero downrange. These altitude vs. downrange profiles are similar to the original baseline case seen in Figure 5-3. Also shown in Figure 5-21 is the thrust direction angle profile for each of the selected cases, with the circles indicating the start of the final braking phase. Note that all of these profiles exhibit a similar linear behavior as previously noted in the baseline case with knots (Figure 5-14). Tabulated data for the TM DOPH parametric study with continuous throttle is given in Table 5.4, and total ΔV and fuel requirements are summarized in Figures 5-23 and 5-24.

A direct comparison of the throttle profiles for the 20 km case is seen in Figure 5-22. The continuous thrust case initiates the braking phase slightly after the non-continuous thrust case, then is bounded by the 0.4 lower throttle limit until full throttle is com-

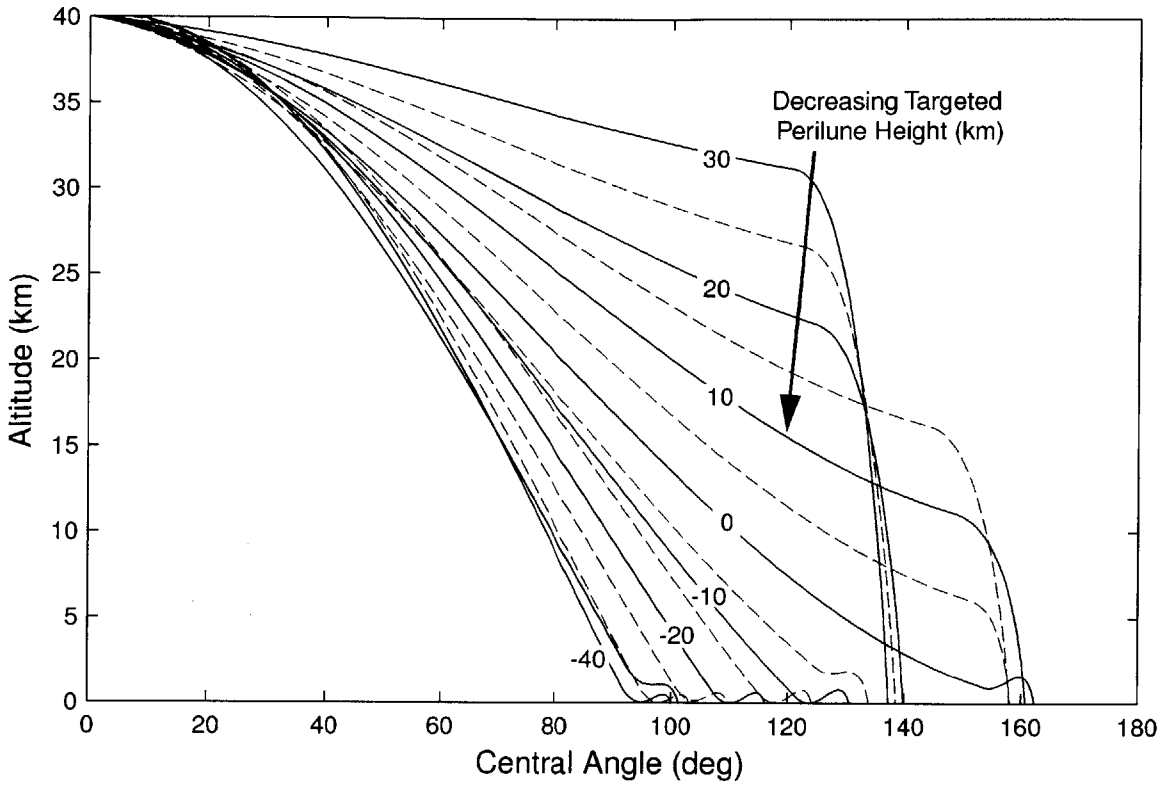

Figure 5-20: Continuous Thrust DOPH Parametric Study (TM), Dashed lines represent increments of 5 km (TM)

manded. Notice that a small spike is seen at the initiation of the braking burn for the continuous thrust case. The fuel penalty of the continuous thrust constraint is 3.4 kg (9.7 m/s ΔV) more than the corresponding open throttle case. This will vary, depending on the lower throttle limit of the engine, but the overall trend is observable. The continuous thrust case takes a shorter time to reach the surface, which is expected because the horizontal velocity is decreased significantly and no longer counteracts gravity.

A compilation of the ΔV usages for each constraint scenario in the parametric study is displayed in Figure 5-23. The ΔV penalty for adding the continuous thrusting constraint is evident in the cases with positive DOPH. For both constraint scenarios there is a minimum seen around 0 to -5 km. This is consistent with the baseline result of -1.8 km as the minimal fuel perilune height. The corresponding fuel usages for the same cases are shown in Figure 5-24.

A brief study was done to determine the fuel required if the throttle was constrained

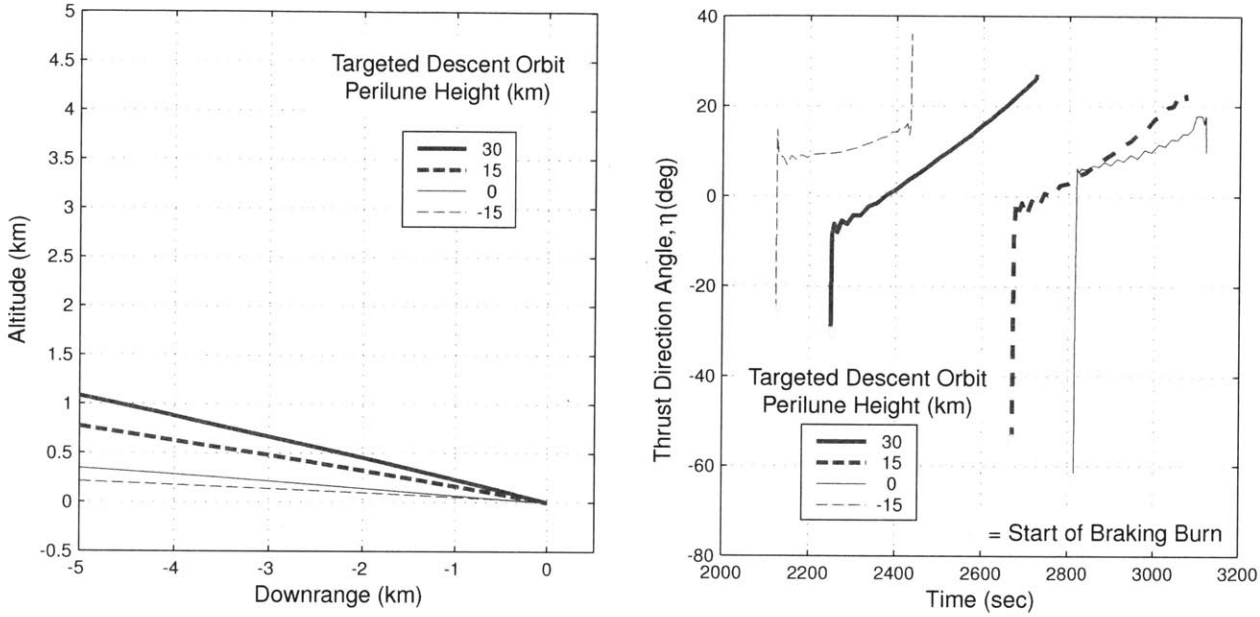

Figure 5-21: Continuous Thrust (TM), Left Plot: Altitude vs. Downrange (Equally Scaled Axes), Right Plot: Thrust Direction Angle during Braking Phase

Table 5.4: Continuous Thrust Case, Tabulated Data

Perilune Altitude km	Normalized Mass Cost -	De-orbit ΔV m/s	Braking ΔV m/s	De-orbit Duration s	Coast Duration s	Braking Duration s	Braking Altitude km
30	-1.090011	2.75	1752.70	0.64	2249.1	474.7	31.237
25	-1.091331	4.12	1747.22	0.96	2282.9	450.6	26.684
20	-1.092607	5.39	1741.51	1.30	2314.0	434.9	22.178
15	-1.094234	6.21	1734.97	1.44	2669.3	402.2	16.220
10	-1.095550	7.38	1729.27	1.70	2740.9	369.0	11.142
5	-1.096840	8.60	1724.59	1.99	2729.2	323.2	6.400
0	-1.097261	9.88	1721.67	2.93	2811.2	306.8	1.023
-5	-1.097323	11.03	1720.46	2.57	2296.9	309.9	2.182
-10	-1.097390	11.97	1719.25	2.76	2238.1	307.3	0.419
-15	-1.097108	13.10	1719.04	3.07	2120.5	311.0	0.695
-20	-1.097010	14.32	1718.06	4.06	1969.3	314.4	0.984
-25	-1.096854	15.54	1717.34	3.76	1851.0	314.2	1.311
-30	-1.096741	16.77	1716.53	4.09	1695.6	315.6	2.607
-35	-1.096538	18.14	1715.84	4.44	1728.2	320.6	1.749
-40	-1.096440	19.38	1714.88	6.41	1681.2	308.4	1.478

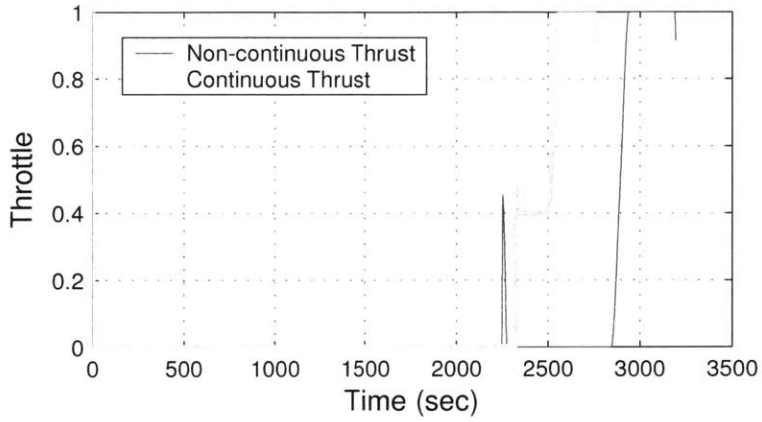

Figure 5-22: Throttle Comparison for 20 km Target Perilune Height Cases

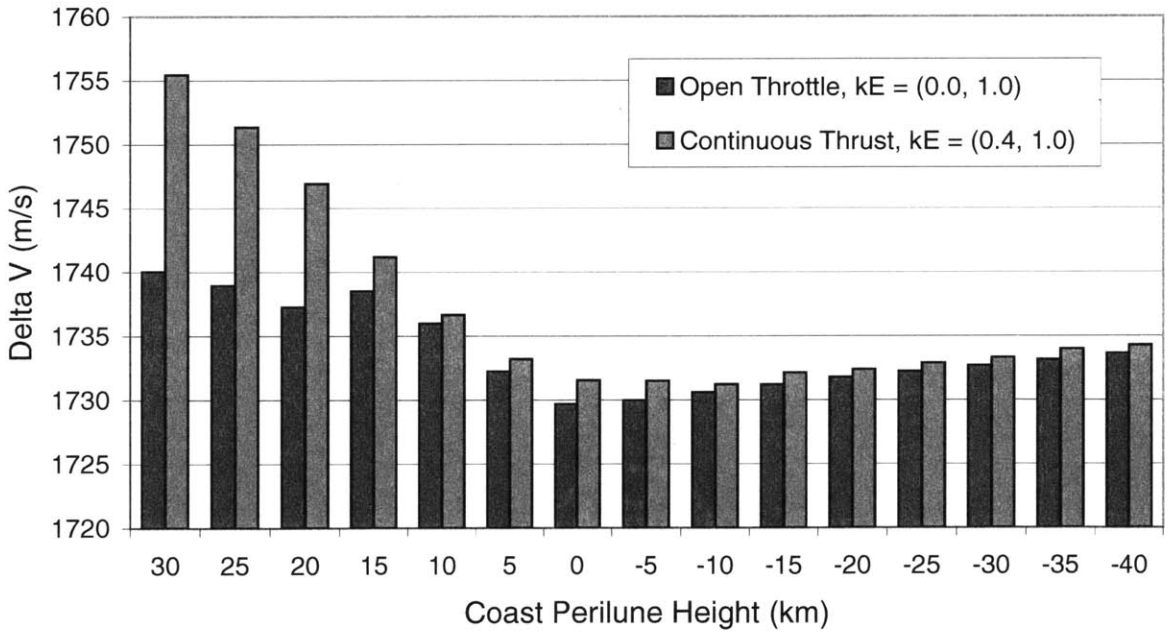

Figure 5-23: DOPH Parametric Study ΔV Results (TM)

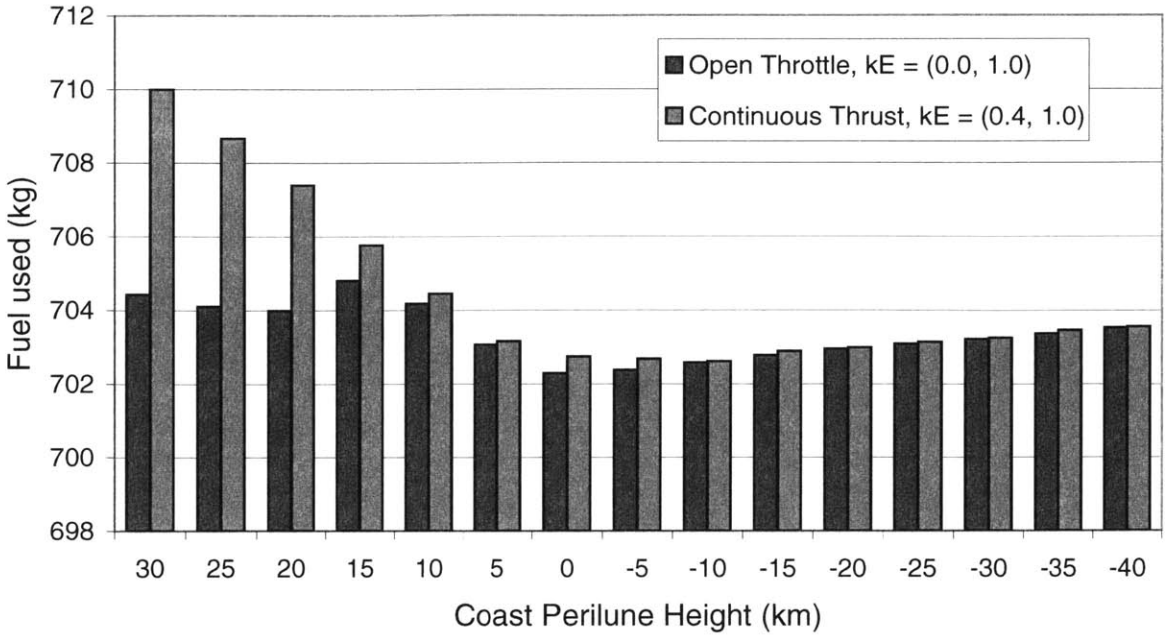

Figure 5-24: DOPH Parametric Study Fuel Usage Results (TM)

to maximum during the thrust arcs, which is consistent with a guidance algorithm that assumes constant thrust during the de-orbit and braking phases. As expected, by further tightening the throttle bounds, more fuel was required. For example, the case which targets a perilune height of 15 km used a total of 707.0 kg of fuel (1746.1 m/s ΔV) when the throttle is constrained to maximum thrust. This value is 1.3 kg (4.9 m/s) above the continuous throttle bound case.

A brief study was performed that attempted to prevent the vehicle from lofting, by constraining the radial velocity to nonpositive (either negative or zero) values. A path constraint was added to the problem of the form:

$$x\, v_x + y\, v_y \leq 0 \tag{5.38}$$

which is the dot product of the radius and velocity vectors written in component form (*i.e.*, $\mathbf{r} \cdot \mathbf{v} \leq 0$).

It was found that instead of lofting, the vehicle flew horizontally at altitudes around 1 km. This was deemed an inappropriate method of constraining the trajectory. An example of the results obtained are seen in Figure 5-25. The plots show only the final

portion of the trajectory during the braking phase. The thick line represents the original -10 km case with continuous thrust, while the thin line includes the nonpositive radial velocity constraint. When lofting is suppressed, the vehicle is seen to fly horizontally at an altitude of 670 m. The flight and thrust direction angle profiles have similar shapes, but the flight path angle for the case with loft suppression does not rise above 0, which is consistent with the constraints imposed on this trajectory. Also notice that there is a time shift of approximately 30 s in the angle profiles, which means that the case with lofting suppression commences the final braking burn 30 s earlier. This shift is not seen in the altitude vs. downrange plot because each case is referenced to the landing point specific for that case. The extra constraint caused the fuel to increase by 0.24 kg (0.78 ΔV). This is not a significant increase, and may be in the noise of the results. A jagged behavior is seen in the thrust direction angle when the additional constraint is added. This suggests that the solution is not well behaved. This study was not further investigated because lofting of the trajectory only occurred where the trajectory targeted to a nonpositive DOPH, which is an operational hazard.

The final operational constraints included in the translational motion setup, before rotational dynamics are introduced, are constraints on the magnitude and direction of the terminal velocity. As discussed in Section 3.6, it is desirable to land the vehicle with a small descending vertical velocity to ensure touchdown The magnitude of the terminal velocity was constrained to be between -0.5 to -2.0 m/s, as these are reasonable values for the lander to withstand at impact. The direction of the velocity is constrained to be directly opposite of the radius vector, which implies a vertical descent direction. Note that this does not guarantee that the attitude of the vehicle will also be vertical.

The two constraints added to the problem, which replace the zero terminal velocity constraints seen in Equations (5.22) and (5.23), are listed below.

$$x(t_f)\, v_x(t_f) + y(t_f)\, v_y(t_f) = -1 \tag{5.39}$$

$$0.5^2 \leq v_x(t_f)^2 + v_y(t_f)^2 \leq 2.0^2 \tag{5.40}$$

Equation (5.39) is the dot product of the radius and velocity vectors at the terminal

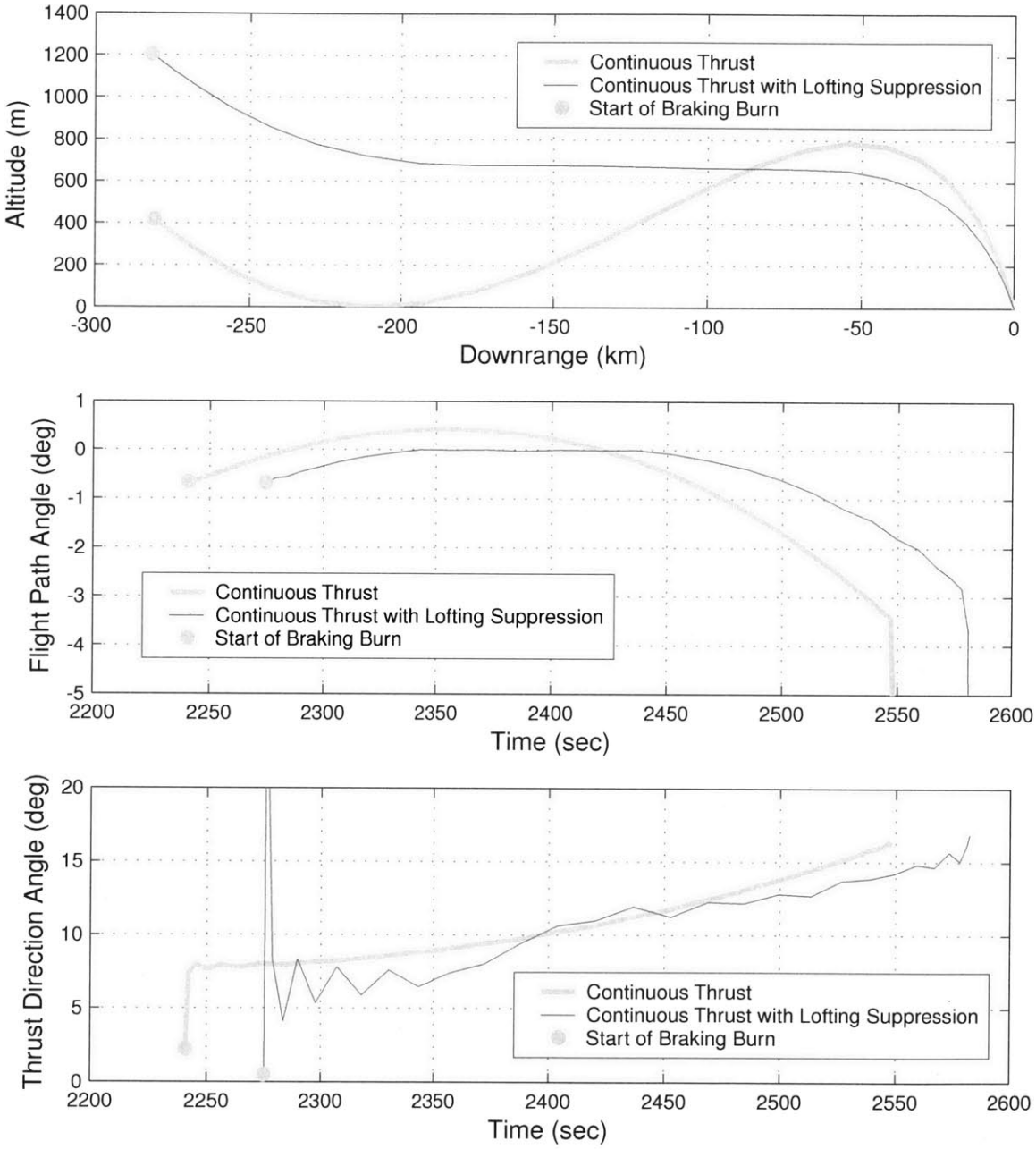

Figure 5-25: Lofting Suppression Result for -10 km Case (TM)

Table 5.5: Addition of Non-zero Terminal Velocity Constraint to Continuous Thrust Case, Tabulated Data

Perilune Altitude km	Total ΔV for Zero Terminal Velocity m/s	Total ΔV for Non-zero Terminal Velocity m/s	Δ V Difference m/s
30	1755.45	1754.28	1.16
25	1751.34	1750.31	1.03
20	1746.90	1746.18	0.73
15	1741.17	1740.29	0.88
10	1736.65	1735.76	0.89
5	1733.19	1732.12	1.07
0	1731.55	1729.46	2.10
-5	1731.49	1731.27	0.22

time, written in component form (*i.e.*, $\mathbf{r}(t_f) \cdot \mathbf{v}(t_f) = -1$) and Equation (5.40) constrains the magnitude of the terminal velocity. Given these constraints, the local optimal solution was found always to have a vertical velocity of -2.0 m/s at landing, which is an extremal of the bound placed on the terminal velocity. This is because any additional velocity the vehicle attempts to null, uses extra fuel. A comparison between the ΔV usages for the continuous thrusting case between the cases which had zero and non-zero terminal velocity constraints is given in Table 5.5. On average, a decrease of 1 m/s is seen. This is equivalent to requiring less fuel to brake the vehicle to -2 m/s, rather than zero.

With the terminal vertical velocity constraints added to the problem, the flight path angle and vertical velocity profiles change slightly. To illustrate this, the vertical velocity and flight path angle profiles for the case which targeted a 15 km perilune height are shown in Figure 5-26. The altitude vs. central angle profile is similar to the 15 km case shown in Figure 5-20 (dotted line between the solid lines marked 10 and 20). In Figure 5-26, the final values for the flight path angle and vertical velocity of the DIDO solution are -90 deg and -2 m/s, respectively. There is a propagation error of 4.5 deg and 1.1 m/s for flight path angle and vertical velocity, respectively. In the final 1.7 sec of the trajectory, the vehicle's flight path angle changes 72 deg, which is an average rate of 42.4 deg/s. The vehicle's trajectory is still largely horizontal and only becomes vertical at the last possible moment. The thrust angle, although not shown, has a final value of 21 deg

and the vehicle does not land in a legs down orientation.

These trajectory characteristics are still undesirable. First, the vehicle has a vertical velocity only during the last seconds of the trajectory. The vehicle's approach is still largely horizontal and viewing of the landing site for hazard avoidance is hampered. Second, it is more desirable to descend vertically for a longer duration of time in order to acquire accurate site-relative altitude and velocity measurements. This trajectory does not allow for this. Lastly, the vehicle still lands with a non-vertical attitude. Because attitude kinematics are not included in the dynamics of the problem, the final attitude profile of the vehicle cannot be constrained. It is more reasonable to add attitude kinematics and control the angular rate, angular acceleration, and terminal attitude constraints of the vehicle. If attitude constraints are added, the flight path angle should also have a more gradual transition to radially down. Hence the vehicle's trajectory will exhibit a steeper approach path to the landing site. All of the reasons listed above provide motivation to include attitude kinematics and constraints in the optimization framework. This study is presented in the following section.

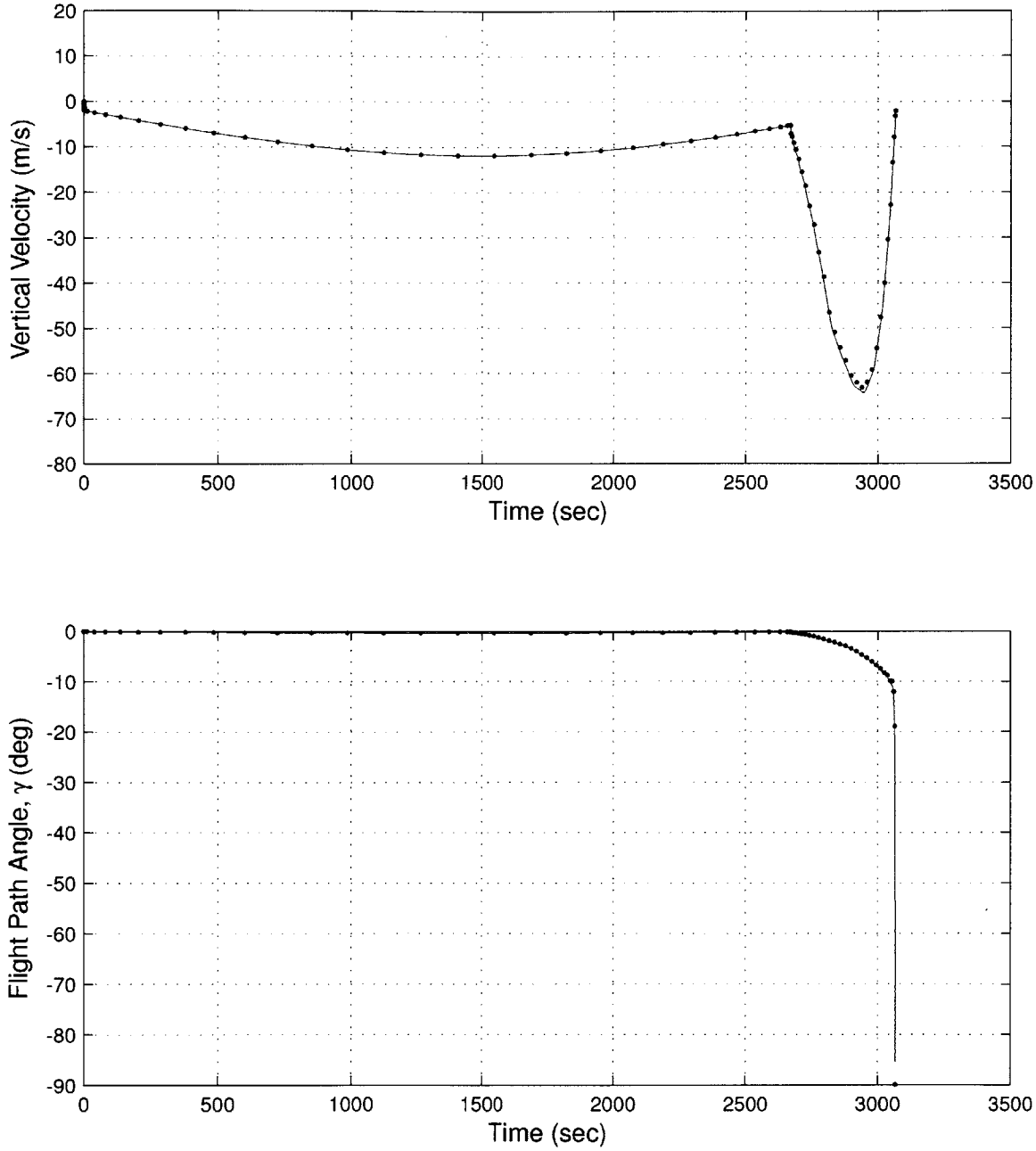

Figure 5-26: Parametric Study Fuel Usage Results (TM)

5.2 Translational Motion with Rotation (TMR)

In the previous section, only the translational motion of the vehicle was included in the equations of motion. In that case, the attitude of the vehicle was able to change instantaneously. This is not realistic, because rotational motion is retarded by vehicle inertia. In this section, attitude kinematics are included in the EOM to restrict the rotational motion of the vehicle and to investigate to effect of the attitude kinematics on the fuel usage of the trajectory. The problem is set up and explained next.

For the TM analysis, the cartesian form of the EOM was used. However, the polar form of the EOM is used in this section since it is more straightforward to define attitude and terminal velocity constraints in the polar coordinate framework. The thrust angle from the radial direction (ψ^r as defined in Section 3.4), the vertical velocity (v_r), and the horizontal velocity (v_θ) are individual components of the state. Therefore, simple bounds can be placed on the variables, instead of nonlinear event constraints. Bounds and event constraints are treated separately by the optimization code [31]. By bounding a variable to be within a certain range, the optimization code only searches in this range. If an event constraint is instead imposed, the searchable region is open and the optimizer can search over all possible solutions and checks to ensure that the event constraint is satisfied. Thus, converting the problem to the polar form reduces the search region, which allows the optimization code to run faster.

The polar form of the EOM were given in Equations (4.20) - (4.23), (4.25) - (4.26), and (4.27) and are restated below for convenience. To verify the EOM, a trial case was run using both the cartesian and polar forms of the EOM and the same results were obtained, when compared in the inertial frame. The fuel usages for these trial runs matched to within 0.01% and the altitude vs. central angle profiles had no distinguishable differences. This

verifies that both EOM forms were correctly derived and implemented.

$$\dot{r} = v_r \tag{5.41}$$

$$\dot{\theta} = \frac{v_\theta}{r} \tag{5.42}$$

$$\dot{v_r} = \frac{v_\theta^2}{r} - \frac{\mu}{r^2} + \frac{T_{maxE}\, k_E}{m} \cos\psi^r \tag{5.43}$$

$$\dot{v_\theta} = -\frac{v_r v_\theta}{r} + \frac{T_{maxE}\, k_E}{m} \sin\psi^r \tag{5.44}$$

$$\dot{\psi^r} = \omega - \dot{\theta} \tag{5.45}$$

$$\dot{\omega} = \alpha \tag{5.46}$$

$$\dot{m} = -\frac{T_{maxE}\, k_E}{V_{exE}} \tag{5.47}$$

The state of the system is given as:

$$\mathbf{x}(t)^T = [\ r(t) \quad \theta(t) \quad v_r(t) \quad v_\theta(t) \quad \psi^r(t) \quad \omega(t) \quad m(t)\ ] \tag{5.48}$$

and the control vector is composed of the engine throttle command, k_E, and the inertial angular acceleration command, α:

$$\mathbf{u}(t)^T = [\ k_E(t) \quad \alpha(t)\ ] \tag{5.49}$$

where $\alpha \in [-0.5, 0.5]$ in units of deg/s^2, and $k_E \in [0, 1]$.

The angular acceleration command of the vehicle was used so that the results are applicable to different vehicle RCS configurations. Maximum and minimum limits on the angular rate and angular acceleration were chosen as $\pm$ 10 deg/s and $\pm$ 0.5 deg/s^2, respectively, to limit the rotational motion of the vehicle to reasonable values. The maximum angular acceleration limit was based on an assumed vehicle inertia about the rotational axis normal to the plane of motion. If the vehicle is assumed to be spherical, with a radius of 0.9 m, the moment of inertia varies from 583 $kg\,m^2$ at the initiation of the trajectory to approximately 350 $kg\,m^2$ at landing. The variation of the moment of inertia is due to the change in the vehicle mass. The assumed vehicle inertia is comparable to the Surveyor

I vehicle [32], which had a slightly lower mass of 995 kg at landing and a moment of inertia of approximately 295 $kg\,m^2$ about the pitch axis. Given the vehicle parameters assumed in this thesis at landing, two coupled 100 N thrusters, will produce a maximum angular acceleration of 0.514 m/s^2. A maximum angular acceleration limit of 0.5 m/s^2 was selected to be consistent with these estimates.

While performing preliminary analysis, the angular acceleration was seen to fluctuate rapidly, while still respecting the minimum and maximum limits. This caused jagged profiles of both the angular rate and thrust angle. The fluctuations in the angular acceleration did not directly affect the final fuel cost because the mass flow due to rotational dynamics was neglected, but led to large propagation errors (since these rapid changes are ill-conditioned for the propagator). For a realistic system, these rapid fluctuations would unnecessarily deplete fuel, as the thrusters would be firing rapidly to produce the required torques on the vehicle. The cost of an angular acceleration command was included in the cost to be minimized, by appending the integral of a constant, C, times the square of the angular acceleration to the cost functional. The value of C was given a small value (*e.g.*, 1×10^{-4}) so that this term would only have a very small effect on the cost. The modified cost functional is presented in Equation (5.50) and is referred to as the "weighted" minimum fuel cost. The square of the angular acceleration, instead of its absolute value, was used because the square does not have a discontinuity in the derivative at zero.

$$\mathcal{J}_{min} = -m(t_f) + \int_{t_0}^{t_f} C\left[\alpha(t)\right]^2 dt \tag{5.50}$$

Another problem that arose when the rotational kinematics were included in the EOM was a scaling issue. In order to scale the angular rate and angular acceleration to match the time units of the problem with the previous scaling factors, a multiplication of 6500 s and $(6500\ s)^2$ was needed. This produced a large variation in the magnitudes of the state and control components. An altitude of 40 km scaled to 1.023 in normalized units, while an angular acceleration of 0.5 deg/s scaled to 3.7×10^5 in normalized units. This degraded the performance of the optimization code and a sluggish rotational response resulted. This is due to a large difference in the magnitude of the residual for each state component, which is

Table 5.6: Comparison of Scaled Values

Parameter	Unscaled Value	Previous Scaling	New Scaling
T_{maxE}	8000 N	194.4	0.097
V_{exE}	3500 $\frac{m}{s}$	13.1	1.31
r_0	1777.4 km	1.023	20.46
v_{θ_0}	1660 $\frac{m}{s}$	6.21	0.621
m_0	1800 kg	1.8	1.8
ψ_0	-90 deg	-1.57	-1.57
ω_{max}	10 $\frac{deg}{s}$	1134	5.67
α_{max}	0.5 $\frac{deg}{s^2}$	3.7 $\times 10^5$	9.21

the difference between the derivative of the component estimated via the spectral method and the calculated value using the EOM. It is difficult to minimize a cost functional with large variations in the residuals since the optimizer tries to minimize these residuals. When one value is much bigger than the other, the smaller value disappears in the "noise" of the larger value. The scale factors were adjusted to reduce the magnitude variation of the normalized variables. The distance scale factor was reduced by 20, and the time scale factor was reduced by 200. All angles were converted to radians.

$$\text{Distance Normalization Unit } (DU_R) = R_{eq}/20 = 86.87\ km \tag{5.51}$$

$$\text{Time Normalization Unit } (TU_R) = 2\pi\sqrt{\frac{R_{eq}^3}{\mu}}\ /200 = 32.49\ s \tag{5.52}$$

$$\text{Mass Normalization Unit } (MU_R) = 1000\ kg \tag{5.53}$$

A scaling comparison between the previous scaling and the new scaling for some of the relevant quantities is listed in Table 5.6. The code was implemented with the normalized parameters, which were later converted back to dimensional quantities for analysis. The implementation of the code for the current TMR analysis is discussed next.

5.2.1 Constrained Optimal Trajectory with Rotational Motion (TMR)

The discussion of the TMR results starts with the case which includes the operational constraints considered in the previous TM analysis. As discussed in Section 3.6, it is highly desirable to target a positive DOPH in case the engine fails to ignite for the final descent. It was seen in the comparison of fuel usage vs. DOPH in Figure 5-24, that fuel usage increases with increasing perilune height for cases that target above 5 km. Therefore, minimizing the targeted DOPH is the most fuel effective. A minimum DOPH of 15 km supports clearance of mountainous lunar terrain and includes margin for navigational error [3]. The representative case used to illustrate the rotational kinematic effects was therefore chosen to have a DOPH of 15 km, which is a compromise between safety and fuel consumption. Other criteria enforced on the trajectory include: bounded thrust, a near-zero terminal vertical velocity, and a terminal vertical attitude.

The terminal vertical velocity was constrained to be between -0.5 and -2.0 m/s to ensure touchdown. Given this constraint, the optimum was always found to have a -2.0 m/s solution, since any attempt to null the additional velocity will use extra fuel. The terminal thrust angle, ψ_f, is constrained to be within $\pm$ 0.5 deg of the vertical direction at landing. During preliminary analysis, when the scaling problem had not yet been resolved, the optimizer had difficulties finding a feasible solution that terminated the attitude at exactly zero ($\psi_f \equiv 0$). This is because the vehicle has a large horizontal velocity and the sluggish response cause the vehicle to be unable to right itself in time before it landed. A relaxed constraint was placed on this variable in order to loosen this constraint. In an actual landing, a deviation of 0.5 deg would not be significant, as vehicles are normally designed to tolerate landing at angles of more than 20 deg relative to the surface without tipping. In later analysis, after the scaling issue was resolved, the loose attitude constraint was left in the problem in order to investigate which attitude the vehicle would chose as the optimum within the bounds. It was found that the vehicle always chose the terminal attitude to be -0.5 deg with respect to vertical. Any additional rotation of the vehicle would require more input angular acceleration and add to the cost.

The initial and terminal constraints imposed on the system are listed below. Notice that these are all simple bounds on the state variables, and are not nonlinear constraints as seen previously with the cartesian form of the equations of motion. This improves the convergence properties of the optimizer, which is a major benefit of using the polar form of the equations of motion for the Moon landing problem.

Initial Constraints

$$\mathbf{x}(t_0) = \mathbf{x}_0 \tag{5.54}$$

Terminal Constraints

$$r(t_f) = R_{eq} \tag{5.55}$$

$$-2.0 \leq v_r(t_f) \leq -0.5 \qquad m/s \tag{5.56}$$

$$v_\theta(t_f) = 0 \tag{5.57}$$

$$-0.5 \leq \psi^r(t_f) \leq 0.5 \qquad deg \tag{5.58}$$

$$m(t_f) \geq m_{dry} \tag{5.59}$$

The variable $\mathbf{x}_0$ is the initial value of the state, where $(\theta_0,\ v_{\theta 0},\ \omega_0) = 0$ and the other components previously specified in Table 5.6 were used:

$$\mathbf{x}_0^T = [\ r_0 \quad \theta_0 \quad v_{r0} \quad v_{\theta 0} \quad \psi_0^r \quad \omega_0 \quad m_0\ ] \tag{5.60}$$

A total of 144 nodes were used for this study, with each phase having 48 Nodes each. The three phases (de-orbit, descent, and braking) were separated with two knots in order to allow a discontinuity in the control and place a higher concentration of nodes in the de-orbit and braking phases. Having an equal number of nodes in each phase was sufficient for this purpose and propagation error did not accumulate as rapidly by having an increased number of nodes during the descent phase. The additional constraints needed to include the two knots and to constrain the DOPH are listed below. The throttle was bounded between 0.4 and 1 during the thrusting arcs of de-orbit and braking. Because of this, it

was not necessary to constrain the altitude at the end of the coast phase.

State Variable Bounds

$$r(t) \geq R_{eq} \qquad \textit{Above the surface} \tag{5.61}$$

Control Variable Bounds

$$0.4 \leq k_E(t) \leq 1.0 \qquad \textit{De-orbit Phase} \quad (t_0 \leq t \leq t_1) \tag{5.62}$$

$$-0.5 \leq \alpha(t) \leq 0.5 \qquad \textit{De-orbit Phase} \quad (t_0 \leq t \leq t_1) \tag{5.63}$$

$$k_E(t) = 0 \qquad \textit{Descent Coast Phase} \quad (t_1 \leq t \leq t_2) \tag{5.64}$$

$$\alpha(t) = 0 \qquad \textit{Descent Coast Phase} \quad (t_1 \leq t \leq t_2) \tag{5.65}$$

$$0.4 \leq k_E(t) \leq 1.0 \qquad \textit{Braking Phase} \quad (t_2 \leq t \leq t_f) \tag{5.66}$$

$$-0.5 \leq \alpha(t) \leq 0.5 \qquad \textit{Braking Phase} \quad (t_2 \leq t \leq t_f) \tag{5.67}$$

Event Constraints

$$\mathbf{x}^-(t_1) = \mathbf{x}^+(t_1) \tag{5.68}$$

$$\mathbf{x}^-(t_2) = \mathbf{x}^+(t_2) \tag{5.69}$$

$$r_p(t_1) = r_{pC} \tag{5.70}$$

$$t_0 < t_1 < t_2 < t_f \tag{5.71}$$

The state is equated at the knot with Equations (5.68) and (5.69), where the superscripts $(\ )^-$ and $(\ )^+$ denote the values of the state just prior to and after the knot, respectively. The descent orbit perilune radius is specified with Equation (5.70), where the variable r_{pC} represents the desired perilune radius value. The final constraint ensures that events are sequential. The calculation of perilune radius was given in Equation (3.9). Using the polar form variables, this equation simplifies to Equation (5.72), which does not have a singularity.

$$r_p = \frac{r^2 v_\theta^2}{\mu\left(1 + \sqrt{\left(\frac{r v_\theta^2}{\mu} - 1\right)^2 + \left(\frac{r v_r v_\theta}{\mu}\right)^2}\right)} \tag{5.72}$$

The local weighted fuel minimum solution for the 15 km targeted perilune height

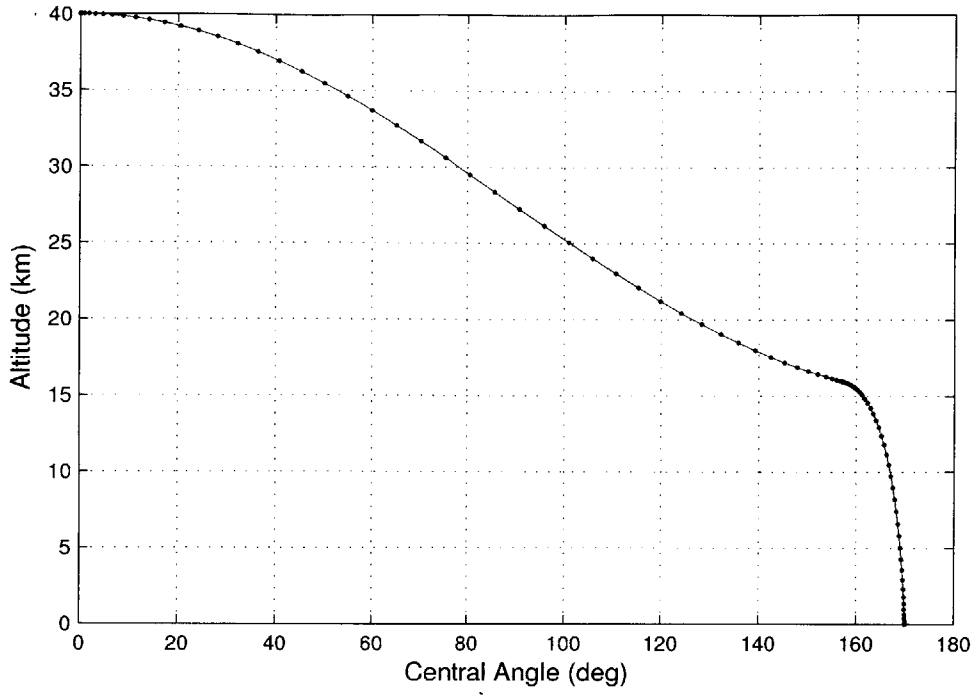

Figure 5-27: Weighted Minimum Fuel Local Optimum Trajectory Profile; +15 km DOPH (TMR)

trajectory is presented in Figure 5-27. The points in the plot represent the DIDO solution, while the solid line is the propagated altitude and central angle. The trajectory descends on the 40 by 15 km descent orbit and initiates the final braking burn (prior to reaching perilune) at an altitude of 16 km. The final descent consists of a continuous burn to the ground and a rotation of the vehicle during the last 50 s. The vehicle lands -0.5 deg from a completely vertical attitude, with -2 m/s of vertical velocity, at a final central angle of 169.92 deg. This corresponds to a total downrange transverse of 5153 km during the flight. The trajectory requires 713.97 kg of fuel (1768.1 m/s ΔV), which is 8.8 kg (27.81 m/s) more than the corresponding 15 km TM case with the near-zero terminal vertical velocity constraint imposed. An altitude vs. downrange plot of the final braking phase is presented in Figure 5-28. As expected, the trajectory is not as shallow as the original baseline case (seen in Figure 5-2). For a better scaling representation of the final approach to the touchdown point, the final 5 km of downrange is plotted in Figure 5-29. A vertical approach during the final portion of the trajectory is visible.

Details of the trajectory are presented in Figures 5-30 and 5-32. Enlarged portions

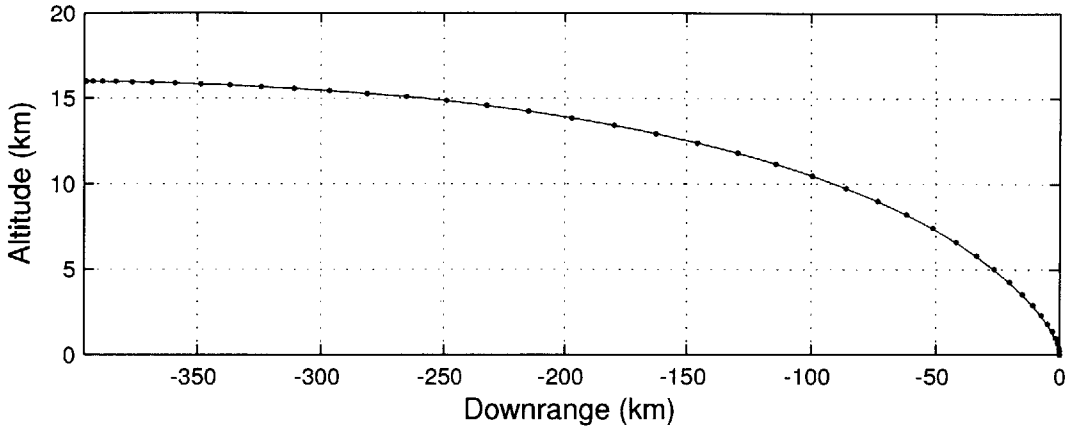

Figure 5-28: TMR +15 km DOPH, Altitude vs. Downrange during Final Braking Phase

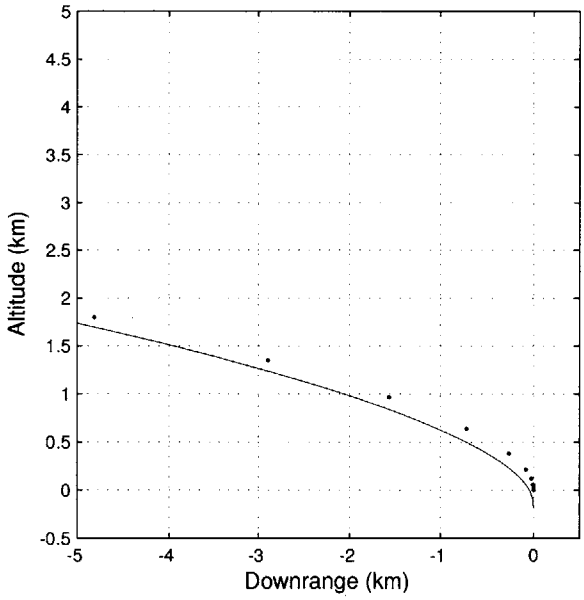

Figure 5-29: TMR +15 km DOPH, Altitude vs. Downrange (Equally Scaled Axes)

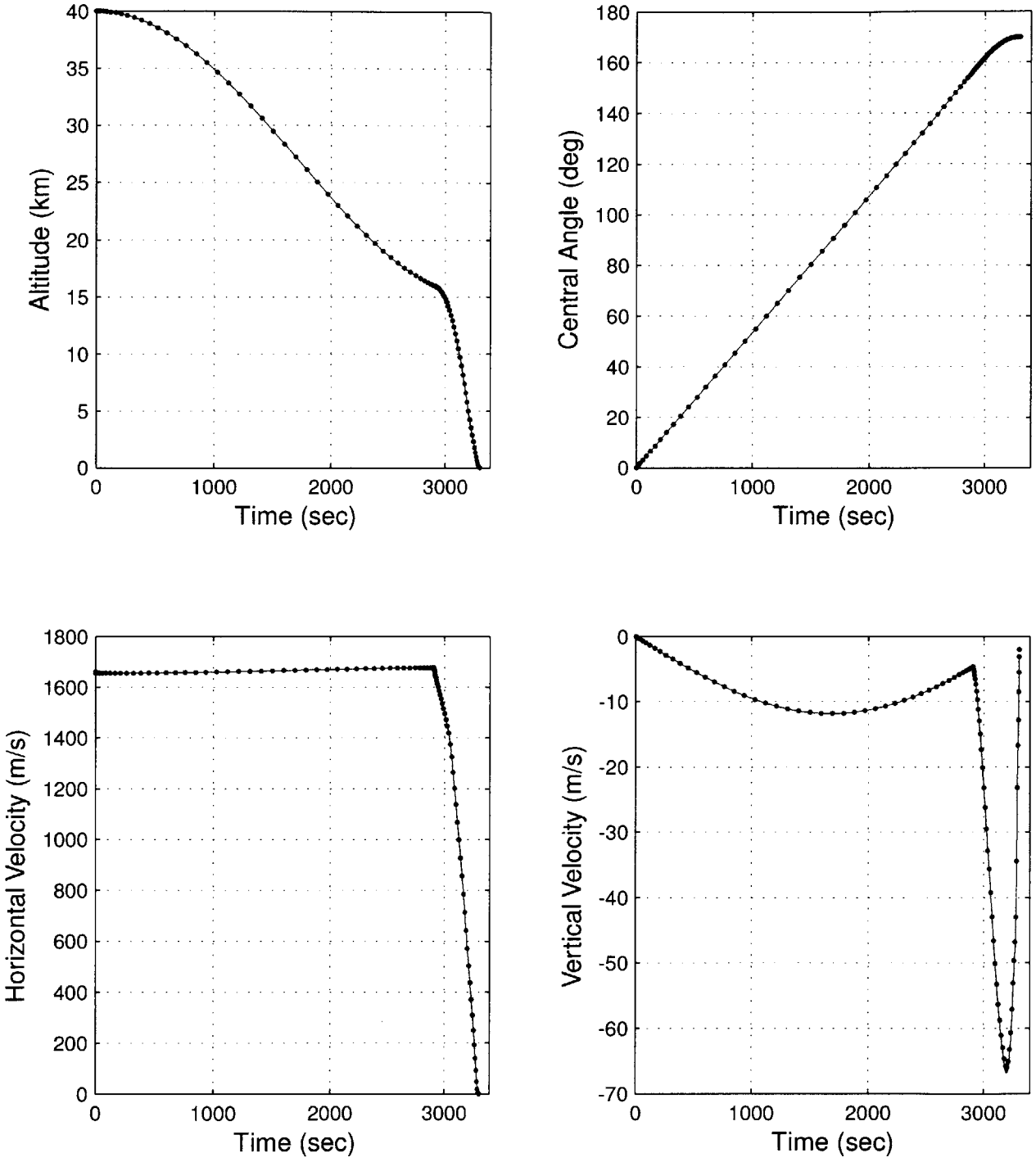

Figure 5-30: TMR +15 km Targeted Perilune Trajectory Results

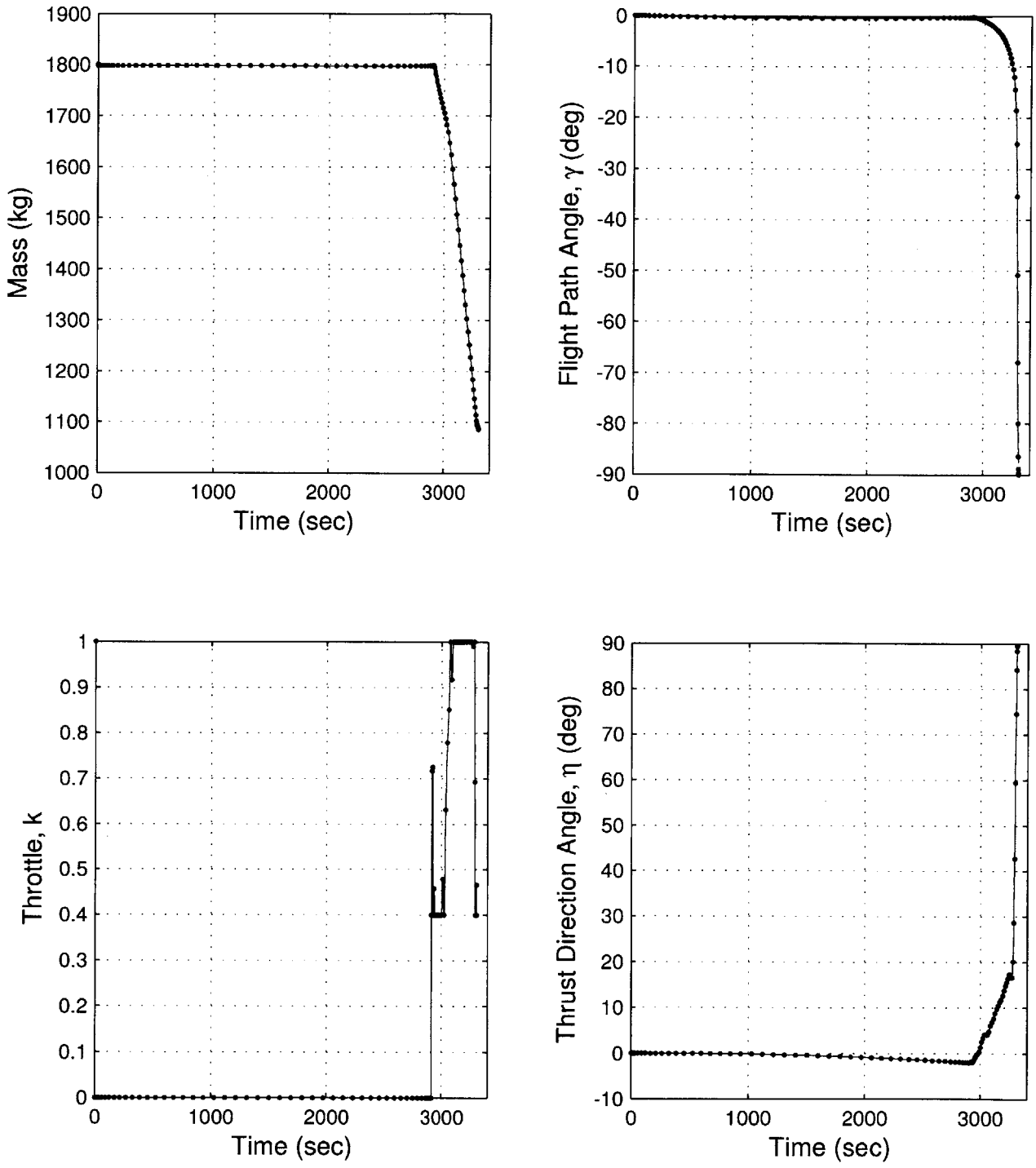

Figure 5-31: TMR +15 km Targeted Perilune Trajectory Results

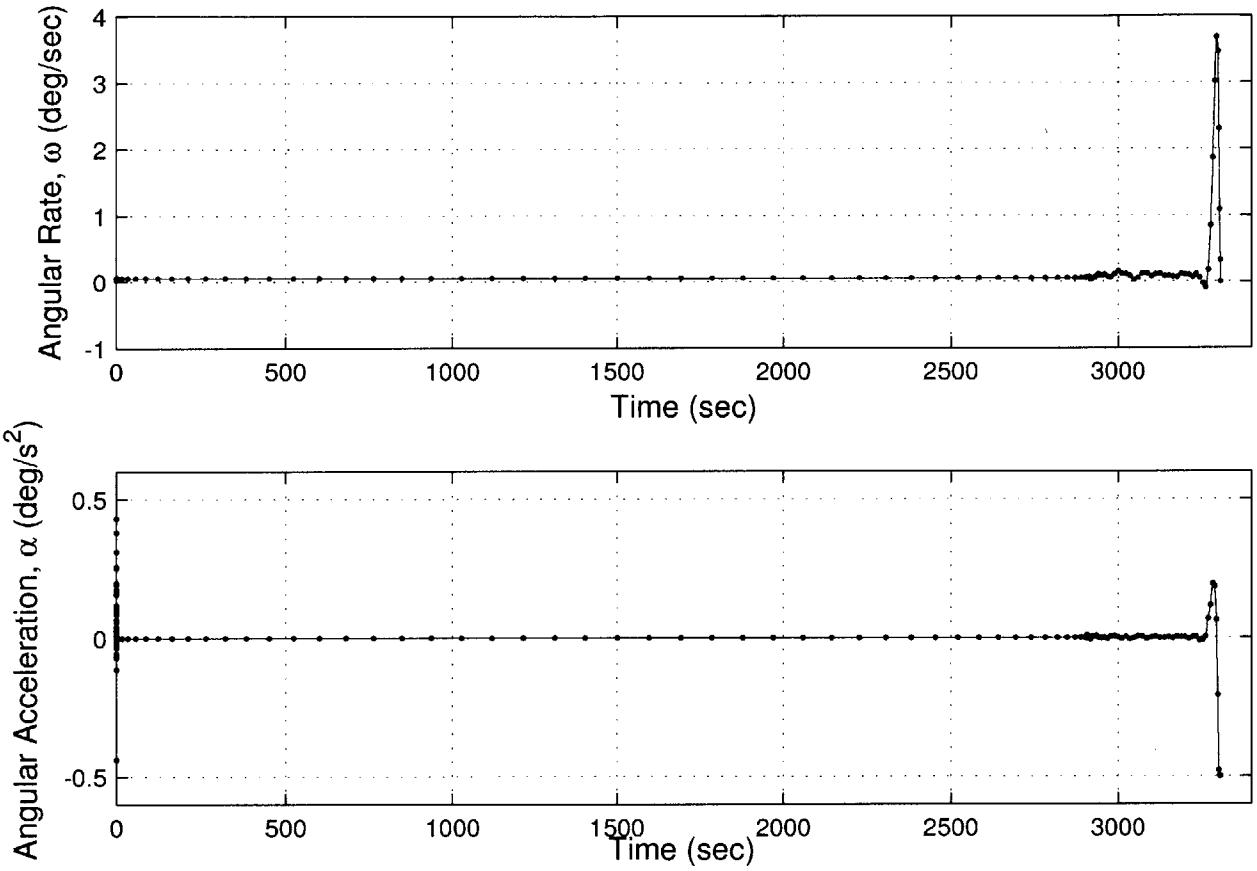

Figure 5-32: TMR +15 km Targeted Perilune Case, Angular Rate and Acceleration

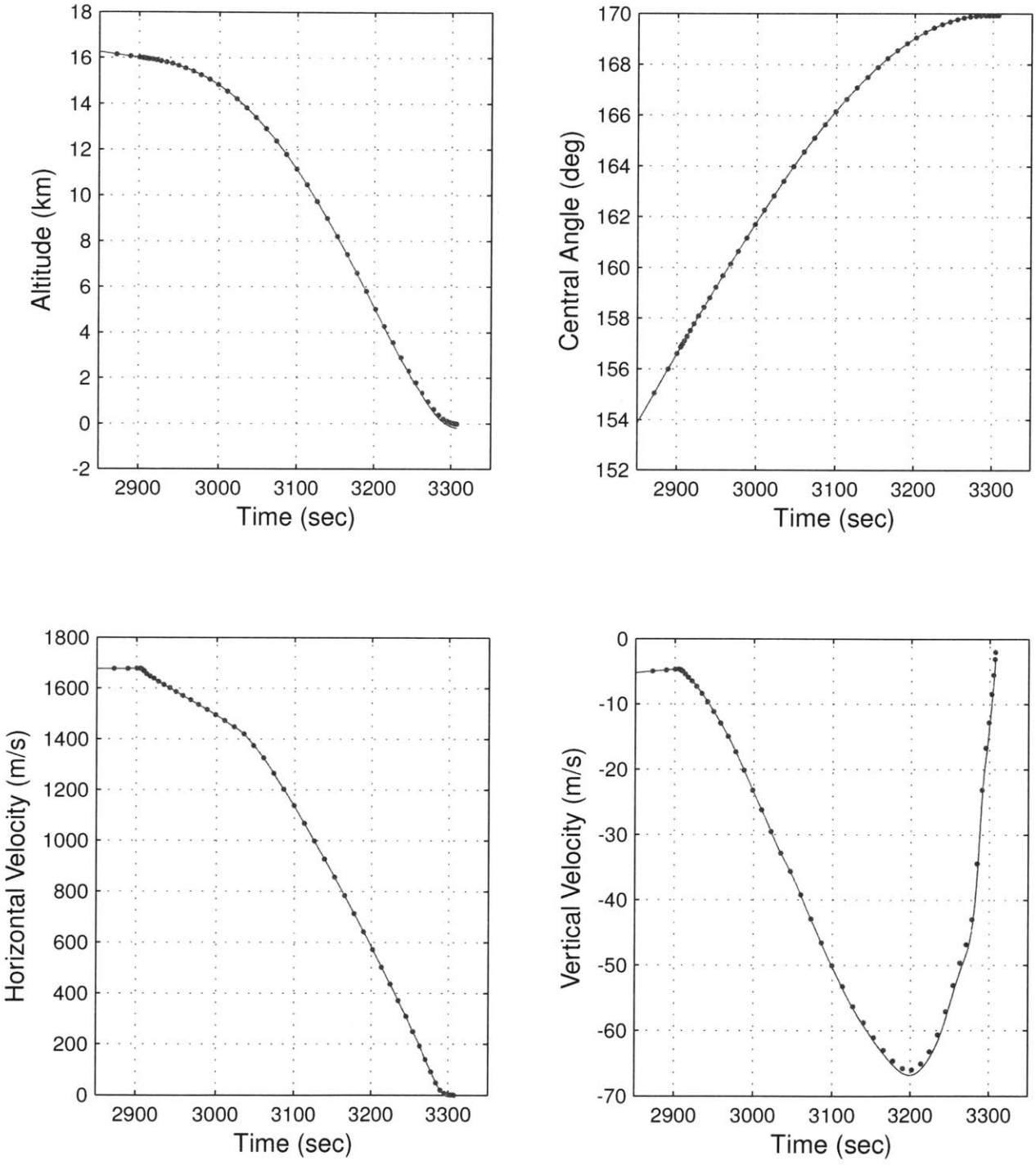

Figure 5-33: TMR +15 *km* Targeted Perilune Trajectory Results (Braking Phase)

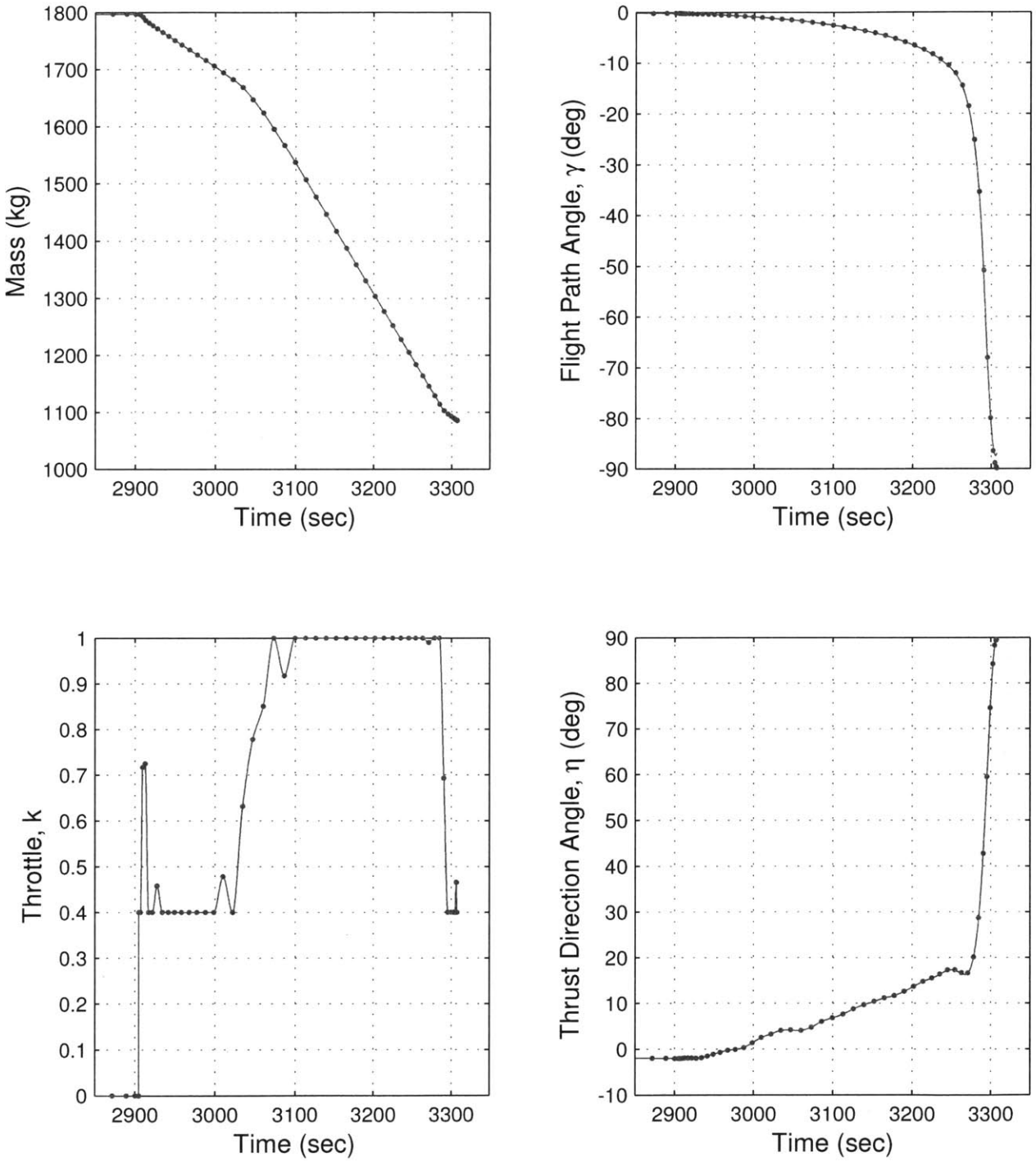

Figure 5-34: TMR +15 km Targeted Perilune Trajectory Results (Braking Phase)

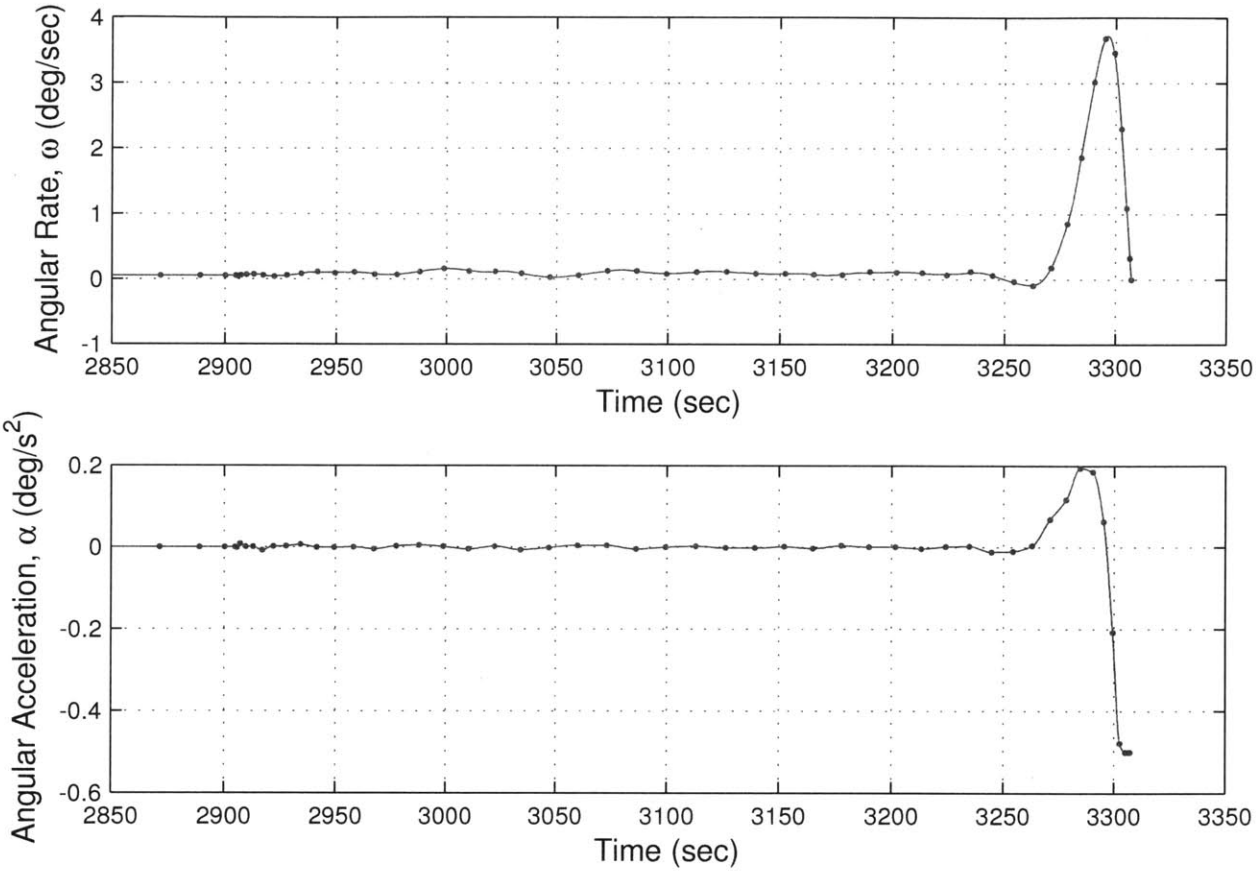

Figure 5-35: TMR +15 km Targeted Perilune Case, Angular Rate and Acceleration (Braking Phase) (TMR)

of the trajectory during the final braking burn are given in Figures 5-33 and 5-35. The zoomed figures have a light grey background for easy distinction. The throttle profile in Figure 5-31 has a short de-orbit burn of 1.32 s in duration, which consumes 3.03 kg of fuel (5.89 m/s ΔV), before the vehicle coasts along the coasting orbit for 2903.6 s. The final burn is initiated at 2904.9 s, when the throttle rises to a value of 0.7 for approximately 9.7 s. This short impulse-like burn is above the 0.4 lower limit, and is similar to the throttle spike previously noted in Figure 5-22 for the continuous thrust 20 km TM case. After the pulse, the throttle remains at the lower limit of 0.4 as it descends to an altitude of 14.2 km, at which full throttle is commanded and maintained until touchdown.

The flight path angle, γ (Figure 5-31), is nearly horizontal for the majority of the trajectory. A deviation of more than -0.5 deg from horizontal is not observed until the final descent begins. This is consistent with a vehicle that is in a nearly circular descent orbit.

The thrust direction is given by the yaw-pitch sequence defined in Section 3.4. As before, the yaw remains at 180 deg, and the vehicle thrusts in a direction opposite the vehicle motion during the entire trajectory. The thrust direction angle, η, which is displayed in Figure 5-31, does not deviate more than -2.5 deg from the changing local horizontal. In order for the thrust direction angle to remain consistent with the local horizontal, the vehicle's attitude must rotate at the same rate that the vehicle revolves around the Moon. This angular rate was calculated to be 0.0541 deg/s. The angular rate of the vehicle during the descent orbit coast was 0.0533 deg/s, which is a difference of 1.5%. This causes a two degree decrease in the thrust direction angle over the duration of the descent coast (Figure 5-31). Also, since the initial angular rate of the vehicle is constrained to zero, an angular acceleration is commanded during the de-orbit burn to increase the angular rate to 0.0533 deg/s at the initiation of the descent coast phase.

The final braking phase of the trajectory is presented in Figures 5-33 to 5-35 as the vehicle descends from 16 km altitude to the surface. A transition from the maximum throttle limit to the minimum begins at 3284 s, and takes approximately 11 s to reach the lower throttle limit, which is due to the spacing of the nodes in this region. During this time, the flight path and thrust direction angles rotate a total of 33 deg and 31 deg,

respectively. The fact that the throttle remains along the lower throttle limit for a the final moments of the trajectory, suggests that the optimal is to command zero thrust as the vehicle rotates. This is further explored by adding a vertical descent phase to the trajectory, which is discussed in 5.2.3. The final value of the angular rate is constrained to zero, which prevents the vehicle from tipping after the vehicle has landed.

The final value of the flight path angle is -90 *deg*, and the vehicle lands with a descending vertical velocity of -2 m/s. This is consistent with the constraints imposed on the problem. The thrust angle also transitions to near-vertical, which corresponds to a positive value of 90 *deg*, and the vehicle thrusts opposite the direction of velocity. The final value of η is 89.5 *deg*, which is 0.5 *deg* from vertical. This is expected as it is an extremal of the $\pm$ -0.5 *deg* allowable final attitude constraint. Making the vehicle any more vertical than necessary would require additional angular acceleration and contribute a small amount to the weighted cost. If it is desired to make the vehicle completely vertical, this additional cost would be negligible in the overall result. On the other hand, loosening this constraint will result in a decrease in the fuel used.

The propagation of the initial conditions with the interpolated DIDO determined control, matches relatively well with the DIDO solution. An altitude error of 181.8 m is calculated between the DIDO solution and the propagated state, which was also found to reduce with increasing nodes as in the cases with only translational motion. Next, the effect of the DOPH on the fuel used is investigated, analogous to the TM investigation. Thereafter, a vertical terminal descent phase is included in the analysis.

5.2.2 Descent Orbit Perilune Height Study (TMR)

A parametric study of the DOPH was performed to compare the results with previously obtained TM data in Section 5.1.3. The objective is to analyze the effect of rotational kinematics on the optimal trajectory. The 15 *km* TMR case, discussed in the previous section, is a subset of the study in this section. The set up is exactly as outlined in the previous section and includes attitude kinematics and constraints, as well as a near-zero terminal velocity constraint. The two throttle constraint scenarios examined are the continuous thrust case, $k_E \in [0.4, 1.0]$, and the maximum thrust case, $k_E = 1.0$. Both

of these throttle bounds are enforced during the de-orbit and braking thrust arcs. k_E is constrained to zero during the descent orbit coast. The first scenario was chosen because it does not allow an alteration of the perilune height to subsurface values before the final burn commences. Cases with maximum thrust were examined in order to compare to guidance algorithms that may assume a constant thrust profile.

For the TMR DOPH study, the number of knots (2), number of nodes in each phase (48), and the constraints (Equations (5.54) to (5.71)) are identical to those used in the +15 km perilune height case outlined in Section 5.2.1. The only value that varies in this parametric study is the desired DOPH, r_{pC}, in Equation (5.70). The TMR DOPH study was limited to targeted perilune heights from 30 km to -5 km, by increments of -5 km. Only the cases of positive perilune height are of real interest for operational consideration, therefore, the study was limited to positive values and one negative value was included for comparison. It was seen in the previous TM study that the negative perilune height cases had roughly equal fuel requirements.

A plot of the weighted fuel local optimal trajectories for the continuous thrust case, as a function of perilune height, is presented in Figure 5-36. Tabulated data for this case is listed in Table 5.7, while plots of altitude vs. range are presented in Figures 5-37 and 5-38 for the braking phase and final portion of the descent, respectively. All trajectories burn within 1.4 km of the perilune altitude or the surface (see Table 5.7, "Braking Altitude" column) and use a range of 1759 - 1783 m/s in total ΔV. The terminal central angle at landing varied from 149.39 to 173.12 deg. This corresponds to a range of 4530 to 5350 km in downrange distance traveled.

A graph of the fuel and ΔV usages for the continuous thrust case can be seen in Figures 5-43 and 5-44. To compare these results to the equivalent case for translational motion, the TM continuous thrust case that includes the non-zero terminal velocity constraint is also displayed in the graph. Including the rotational motion in the dynamics of the problem, enforcing terminal attitude constraints, and using a weighted minimum fuel cost to include the rotational motion in the minimization process, added an average 8.87 kg to the fuel requirement (28.9 m/s ΔV) for the continuous thrusting case (as compared to the TM continuous thrust case). This value should not be neglected when calculating

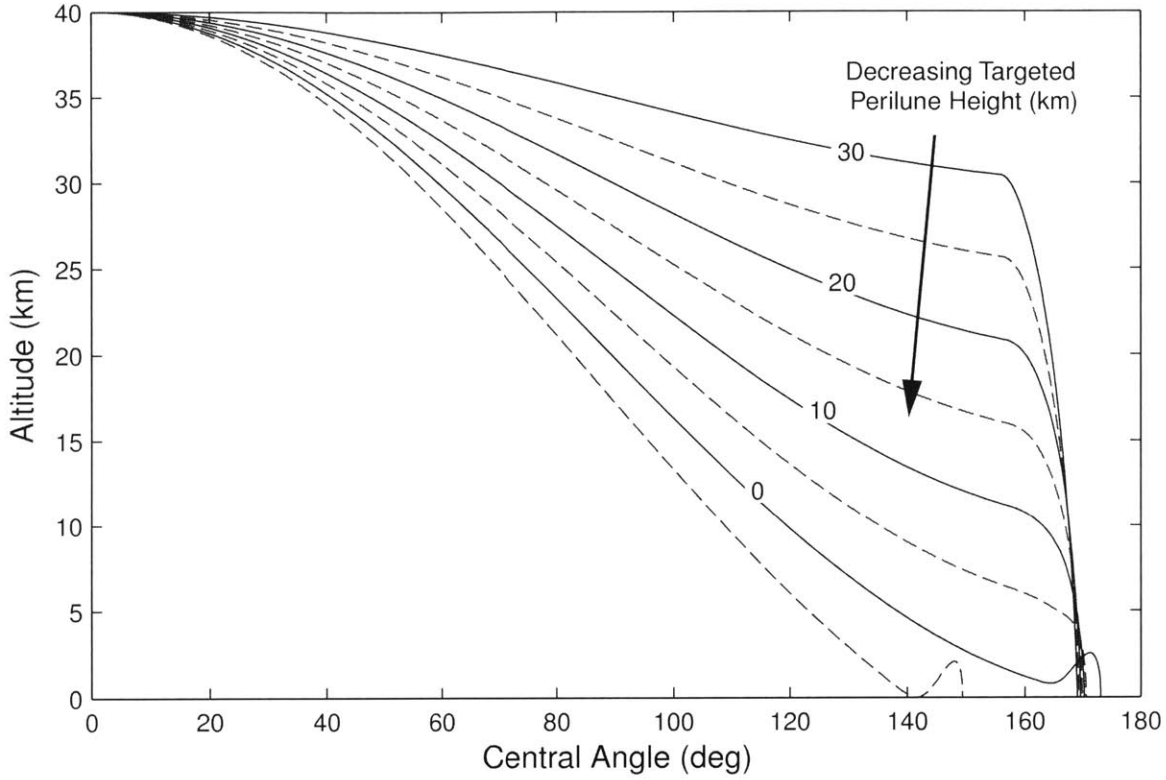

Figure 5-36: Continuous Thrust with Attitude Constraints

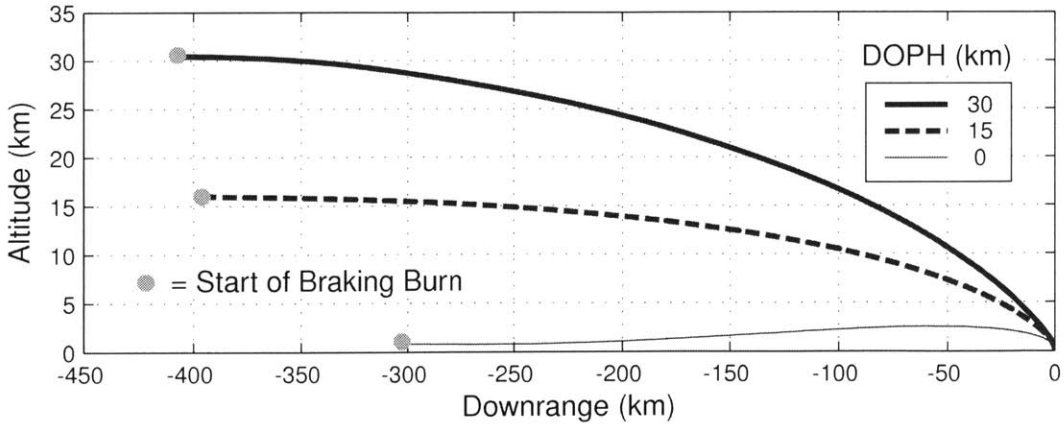

Figure 5-37: Continuous Thrust (TMR), Altitude vs. Downrange during Braking Phase

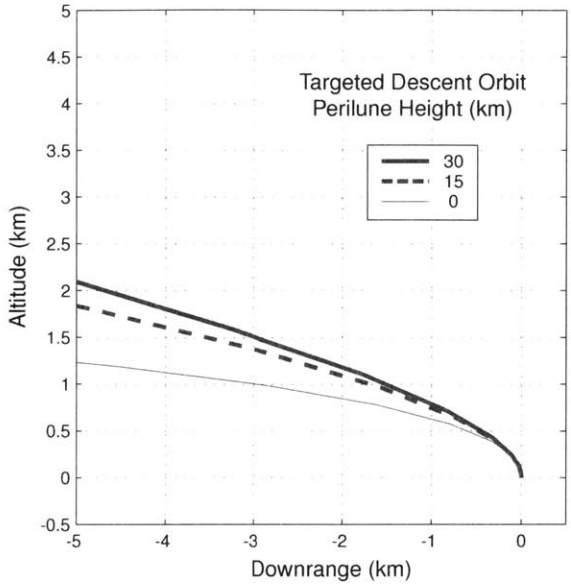

Figure 5-38: Continuous Thrust (TMR), Altitude vs. Downrange (Equally Scaled Axes)

fuel allotments for a mission.

Throttle and thrust direction angle profiles for the final braking burn of selected continuous TMR cases are displayed in Figure 5-39. They are presented separately for clarity, while maintaining the same time scale. Spikes are again seen in the throttle profiles at the initiation of the braking burn in all three cases, which becomes more pronounced with increasing DOPH. The 30 *km* case is seen to have two distinct impulse-like burns before settling at the lower 0.4 limit. The throttle profiles for all three cases then descend to the lower limit for a finite period of time before rising again to maximum throttle. The transition to maximum is ill-conditioned and could be rectified by adding more nodes or including an additional knot which would allow a control discontinuity at this point. In the current implementation, a discontinuity in the control is only allowed at the beginning of the braking burn. A reduction in the throttle to the lower limit for the final portion of the landing is seen in all three cases. During this time, the thrust direction angle, for all three selected cases, exhibits a steep ramp to 90 *deg* before landing. This suggests that the optimum solution is to pitch the vehicle up to a vertical attitude as late as possible, in combination with a significant throttling down of the thrust engine just enough to null gravity (and the residual velocity) as the vehicle prepares for the final landing.

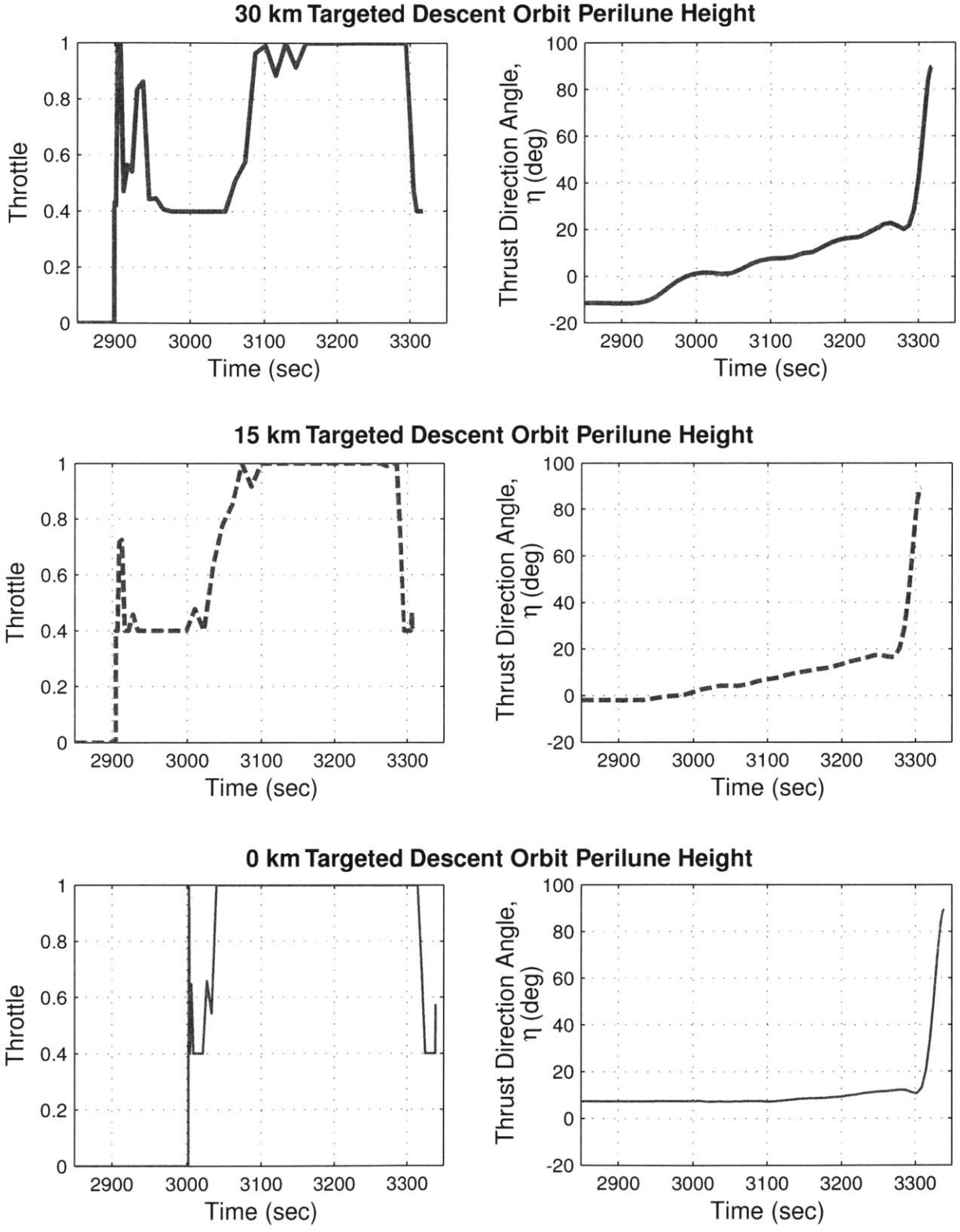

Figure 5-39: Continuous Thrust (TMR), Throttle and Thrust Direction Angle Profiles (Braking Phase)

Table 5.7: Continuous Thrust with Attitude Constraints, Tabulated Data

Perilune Altitude km	Normalized Cost -	De-orbit ΔV m/s	Braking ΔV m/s	De-orbit Duration s	Coast Duration s	Braking Duration s	Braking Altitude km
30	-1.079164	2.34	1780.62	0.53	2898.5	418.4	30.440
25	-1.080950	3.52	1773.73	0.79	2899.2	414.6	25.642
20	-1.082310	4.71	1768.11	1.06	2903.3	403.4	20.818
15	-1.083727	5.89	1762.23	1.32	2903.6	402.4	15.995
10	-1.084549	7.08	1758.13	1.59	2901.3	404.7	11.174
5	-1.084978	8.28	1755.63	1.86	2900.5	405.3	6.338
0	-1.086218	9.48	1750.37	2.13	3000.0	337.2	0.849
-5	-1.085828	10.68	1750.31	2.40	2566.7	339.3	0.348

The second thrust scenario examined, with rotational kinematics included, has maximum thrust during the thrusting arcs. The throttle constraints in Equations (5.62), (5.64), and (5.66) were changed to:

$$k_E(t) = \begin{cases} 1.0, & \textit{De-orbit Phase} \quad (t_0 \leq t \leq t_1) \\ 0.0, & \textit{Coast Phase} \quad (t_1 \leq t \leq t_2) \\ 1.0, & \textit{Braking Phase} \quad (t_2 \leq t \leq t_f) \end{cases} \tag{5.73}$$

A plot of the weighted fuel local optimal trajectories for the maximum thrust case, as a function of targeted perilune heights, is presented in Figure 5-40. Corresponding tabulated data is listed in Table 5.8. Altitude vs. downrange plots for the braking burn and final portion of the landing are displayed in Figures 5-41 and 5-42, respectively. Notice in the altitude vs. downrange plot of Figure 5-42, that the vehicle approaches the landing point with a much more desirable (steeper) profile. The altitude to downrange has a nearly one-to-one correlation. Also shown in Figure 5-42 are the thrust direction angle profiles during the final braking burn. Note that these are nearly unchanged from the thrust direction angle profiles seen in Figure 5-39. The throttle profiles for these cases are not shown, as they are constrained to stay at maximum for the duration of the braking burn. The time at which the switch from minimum to maximum throttle occurs

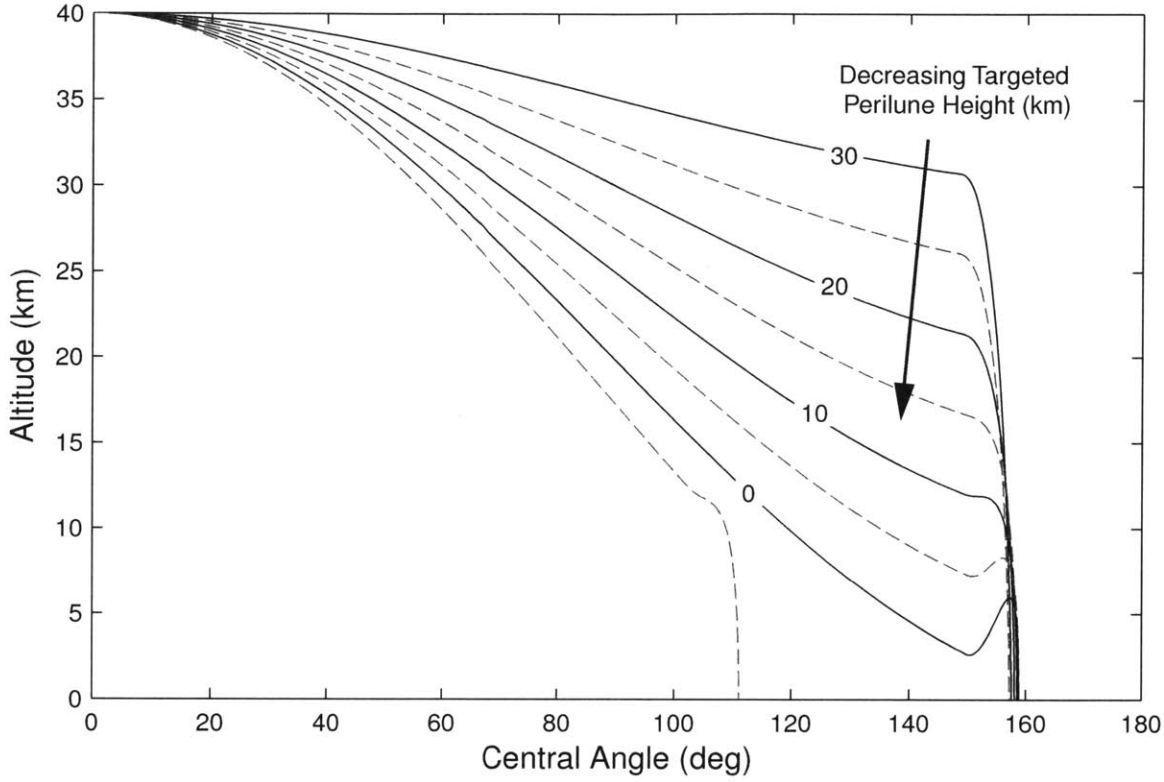

Figure 5-40: Maximum Thrust with Attitude Constraints

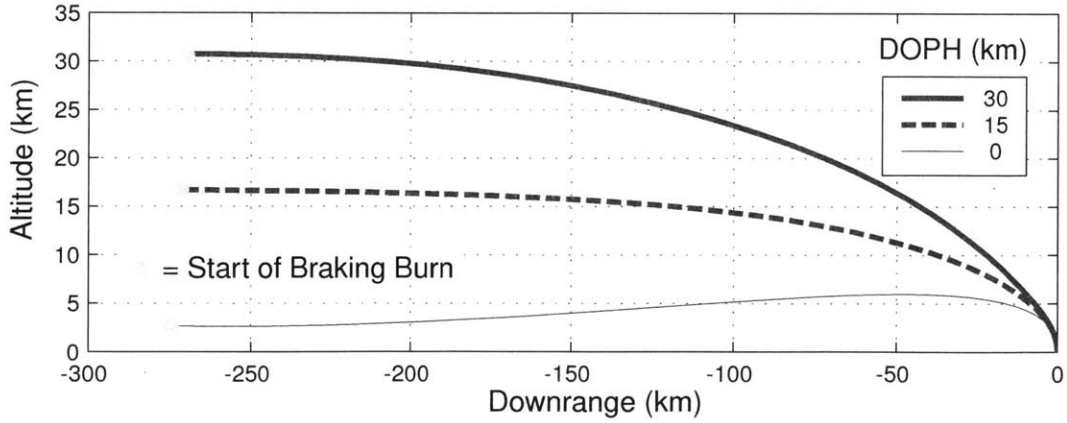

Figure 5-41: Maximum Thrust (TMR), Altitude vs. Downrange during Braking Phase

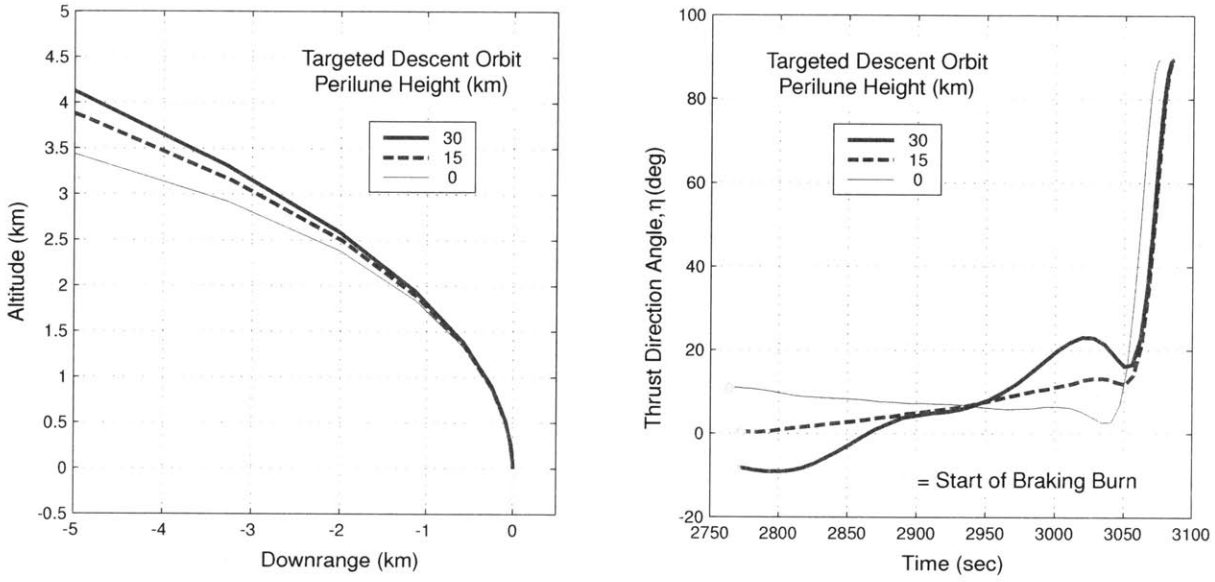

Figure 5-42: Maximum Thrust (TMR), Left Plot: Altitude vs. Downrange (Equally Scaled Axes), Right Plot: Thrust Direction Angle during Braking Phase

Table 5.8: Maximum Thrust with Attitude Constraints, Tabulated Data

Perilune Altitude km	Normalized Cost -	De-orbit ΔV m/s	Braking ΔV m/s	De-orbit Duration s	Coast Duration s	Braking Duration s	Braking Altitude km
30	-1.070106	2.34	1807.59	0.53	2767.1	317.4	30.727
25	-1.072374	3.52	1798.88	0.79	2756.2	316.2	26.112
20	-1.074532	4.71	1790.56	1.06	2768.0	314.9	21.399
15	-1.075721	5.89	1785.75	1.32	2770.2	314.2	16.704
10	-1.076222	7.08	1782.79	1.59	2766.1	313.7	12.037
5	-1.075949	8.28	1782.51	1.86	2766.0	313.5	7.331
0	-1.075254	9.48	1783.27	2.13	2759.8	313.5	2.672
-5	-1.075908	10.68	1780.30	2.40	1895.6	313.0	12.508

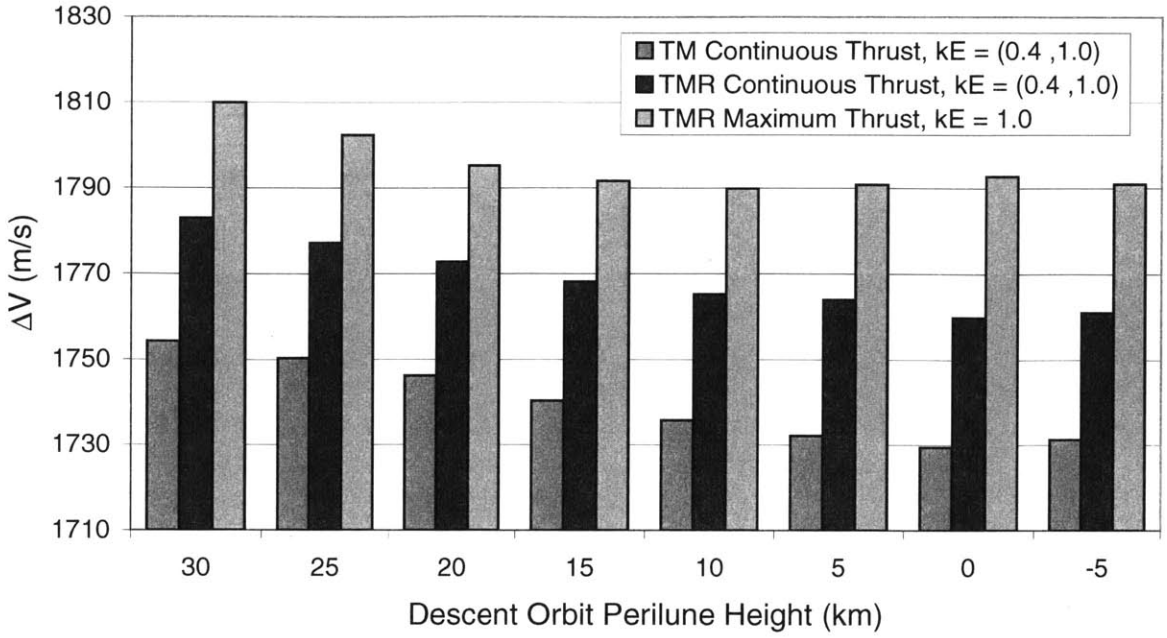

Figure 5-43: TMR Parametric Study ΔV Results and Comparison to TM Data

is represented by circles in the flight path angle plot.

The fuel usages for the maximum thrust case varied from 720.6 to 726.8 kg. This is an average of 8.1 kg more fuel (26.6 m/s ΔV) than the TMR continuous thrust case. The ΔV and fuel requirements for the maximum thrust cases are also included in Figures 5-43 and 5-44 for comparison to the continuous thrust cases. It is interesting to note that the minimum fuel perilune height for the maximum thrust cases occurred at 10 km. To verify this result, a case was run with maximum throttle during the thrusting arcs, with the DOPH unconstrained. The optimal perilune height using maximum thrust during the thrust arcs was found to be 8.7 km above the surface. This is a shift from previous values seen around -1.8 km, which occurs due to the attitude and throttle constraints imposed on the problem. The optimal perilune height is no longer subsurface because the vehicle cannot loft the trajectory and meet the final attitude and vertical velocity landing constraints.

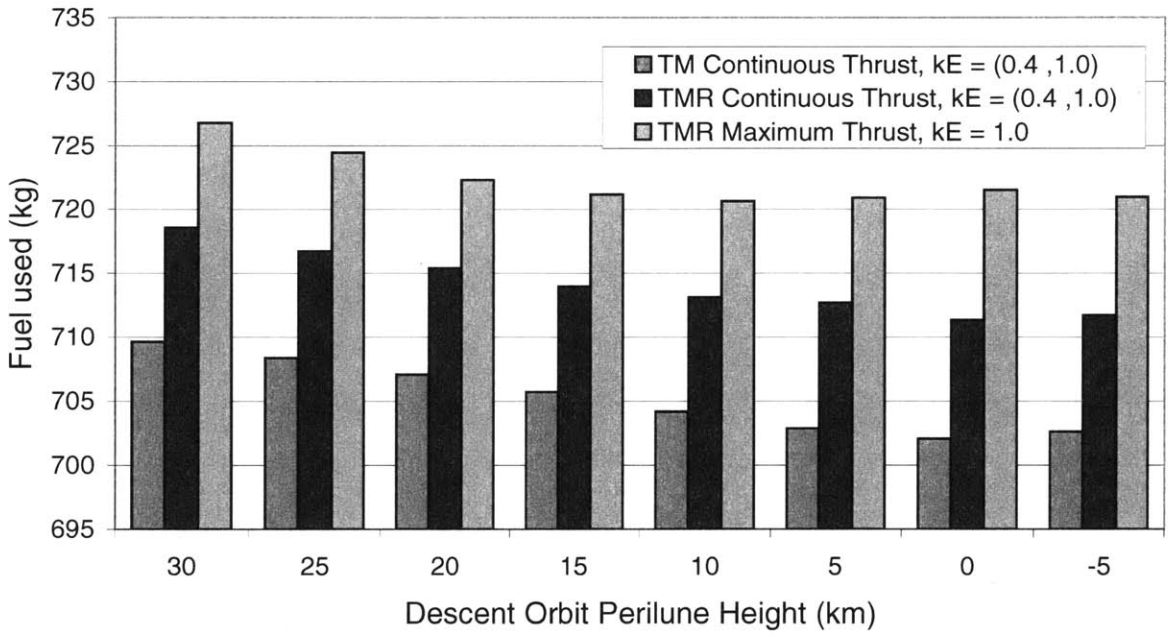

Figure 5-44: TMR Parametric Study Fuel Results and Comparison to TM Data

5.2.3 Terminal Vertical Descent Study (TMR)

In Section 5.2.1, it was observed that the thrust declines to the lower bound during the final few second of the trajectory when vertical landing is enforced. This result instigated an investigation into the inclusion of a terminal vertical descent phase in the problem. This trajectory profile is operationally desirable since a margin of safety is effectively included. It cannot be assumed that the vehicle will follow the optimal trajectory precisely during a real-time landing on the Moon. Errors from various sources, such as gravitational perturbations, off-nominal engine performance, incorrect measurements from navigational sensors, knowledge error in vehicle parameters such as mass inertia, etc, can cause the final position and velocity at touchdown to vary. To allow for this possible error, it is desired to bias the trajectory away from the surface to ensure the vehicle will not prematurely impact. It is also desired to have the vehicle descend with a vertical attitude during the final portion of the trajectory, which is the most crucial portion of the entire landing sequence. A vertical terminal descent will allow for accurate measurements of altitude and velocity, which are required by the onboard navigational equipment for a soft landing. The doppler radar and altimeter are typically placed on or near the bottom of the vehicle so that accurate measurements can be taken until touchdown.

A technique commonly used in guidance algorithms that only consider translational motion is to include an offset point in the trajectory. This offset point is directly above the desired landing site, at a predetermined altitude. This altitude is selected based on worst case navigational uncertainties, and to allow time for the vehicle to right itself before touchdown. The trajectory is designed to have the vehicle arrive at the offset point with a small vertical velocity and zero horizontal velocity. Because the trajectory is most likely horizontal until that point, the attitude of the vehicle at the offset point will be largely horizontal as well. The vehicle then descends to the ground and must right itself in order to null the remaining vertical velocity.

In this section of the thesis, a final terminal vertical descent phase was added to the trajectory. A DOPH perilune height of 15 km was chosen to provide adequate clearance of the mountainous lunar terrain, as discussed in Section 3.5. The altitude at which the

vertical phase begins was varied from 0.5 km to 4 km, by increments of 0.5 km. The previous analyses corresponded to the vertical phase beginning at 0.0 km (*i.e.*, no vertical phase). The throttle is continuous ($0.4 \leq k_E \leq 1.0$) during the de-orbit and braking phase, but has open throttle during the added vertical descent phase ($0.0 \leq k_E \leq 1.0$). The throttle was allowed to vary in the open throttle range during the vertical terminal descent to allow for free-fall trajectories, as seen in the vertical descent example problem in Section 2.2. The terminal soft landing conditions are to land with an attitude ± 0.5 deg of vertical and with a vertical velocity between -0.5 and -2.0 m/s. The horizontal velocity, v_θ, is constrained to zero during the entire vertical phase. By enforcing this constraint, the vehicle is forced to thrust along the one dimensional line defined by the radius vector. Because the engine is fixed to the vehicle, the vehicle must right itself to exactly vertical before any firing of the engine is initiated. Any thrusting in a direction other than vertical would cause the horizontal velocity to have a non-zero value, which violates the constraint. In essence, the vertical phase is the same as the vertical descent example problem given in Chapter 2. In both cases, the vehicle begins at a given altitude with a descending vertical velocity and descends to the surface. The minimum fuel solution found in the example problem was to let the vehicle free fall until the point where maximum thrust is applied. This is also expected in the vertical landing phase of this study.

For each offset altitude, the four constraint scenarios, illustrated in Figure 5-45, were investigated. The constraints being varied are the vertical velocity and attitude of the vehicle at the offset altitude. For each case, r_3 is specified and v_θ is constrained to zero. These cases are discussed next, starting with the most unconstrained case.

For the most unconstrained case, denoted Case N, neither the velocity or the attitude at the offset point are specified. Because of the largely horizontal trajectory, the vehicle would reach this point with a nearly horizontal attitude. The vehicle would then free fall during the vertical descent phase, while rotating the vehicle, until maximum thrust could be applied.

The second case, Case V, has no attitude constraint at the offset altitude, but is required to have a vertical velocity of -0.3 m/s at the offset. This small vertical velocity was chosen to ensure the vehicle comes to a rest and is given more time to assess the

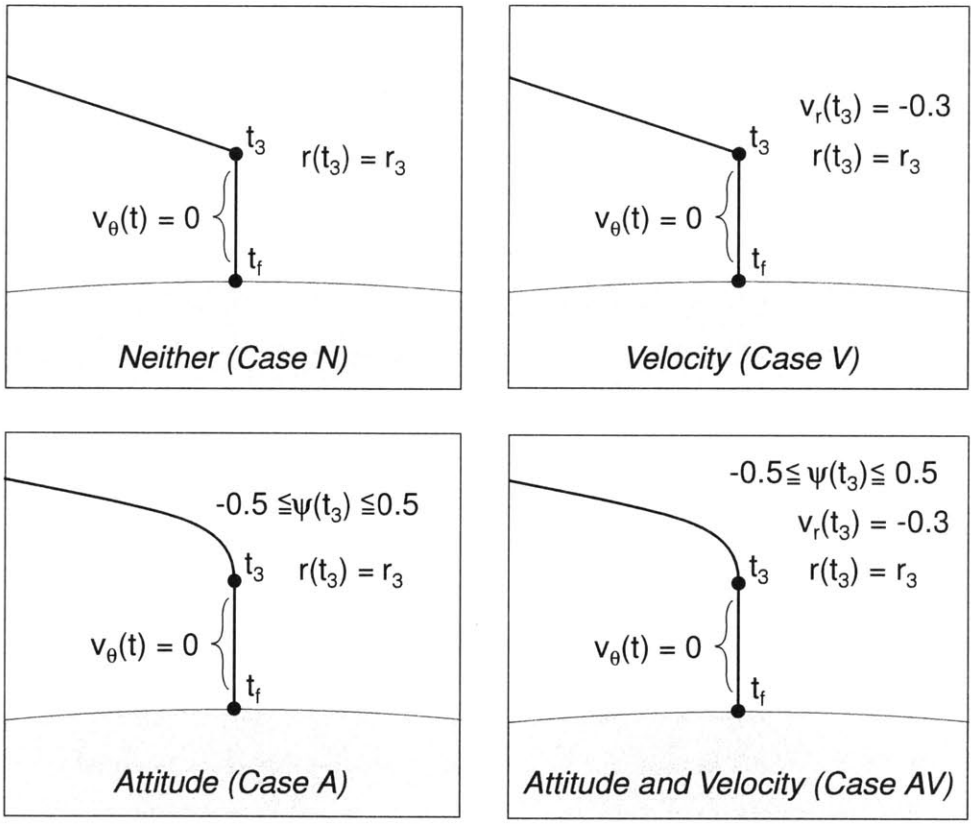

Figure 5-45: Vertical Descent Constraints

navigational error as it descends to the surface. This constraint imposes a safety factor that is not present in Case N. If the vehicle has an altitude error comparable to the offset altitude, the vehicle can right itself and land softly. The vehicle will land properly, provided it has enough time to rotate to a legs-down orientation and null any velocity growth due to gravity.

The third case, Case A, constrains the attitude of the vehicle at the offset altitude. The vehicle must arrive at the offset altitude with an attitude within 0.5 *deg* of vertical. The vehicle must orientate itself prior to this vertical phase, which uses more fuel because it must shape the trajectory away from the weighted minimum fuel solution. However, this allows for accurate measurements of altitude and velocity to begin at the start of the vertical phase and potentially a lower the offset altitude that can be considered "operationally safe". The vertical velocity is not constrained in this case.

The final case, Case AV, enforces both the attitude and velocity constraints at the offset altitude. This is the most constrained case and therefore will use the most fuel, but also includes the most safety margin. If the vehicle was to arrive at the offset point and find that the altitude measurements were completely inaccurate, the vehicle could immediately perform a soft landing, assuming it has met the constraints of the problem at the offset altitude.

The fuel usage and required ΔV of the weighted minimum fuel solutions for each of these constraint scenarios over the range of offset altitudes are plotted in Figures 5-46 and 5-47. Tabulated data is given in Tables 5.9 - 5.10. In all cases, the de-orbit phase had a duration of 1.32 s and required a ΔV of 5.89 m/s. These values are included in the calculation of the total flight time and total ΔV requirements. The ΔV trends and fuel requirements in Figures 5-46 and 5-47 are smooth and consistent, both with each individual case at different offset altitudes, and between the cases. The addition of the vertical velocity constraint is seen to add, on average, 1.8 kg to the fuel requirement (ΔV of 5.8 m/s), while the attitude constraint adds an average value of 8.1 kg (ΔV of 26.4 m/s). When the vertical velocity is not constrained, the vehicle reaches the offset altitude with a vertical velocity that is a function of the offset altitude. This can be seen in the far right column of Table 5.10.

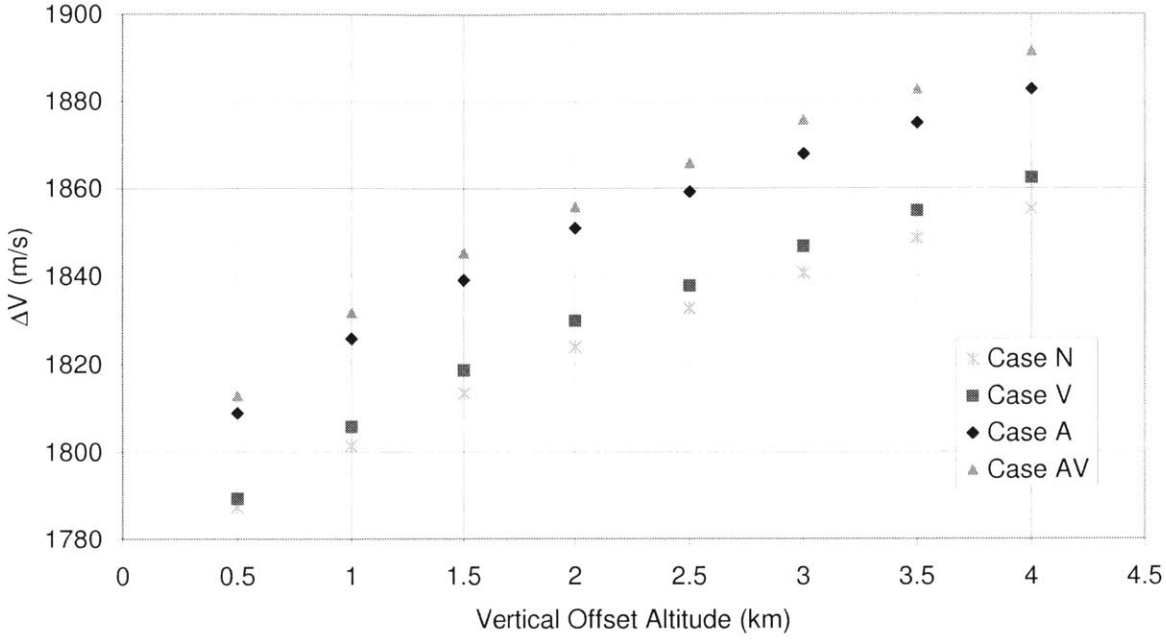

Figure 5-46: Vertical Descent Study ΔV Requirements (TMR)

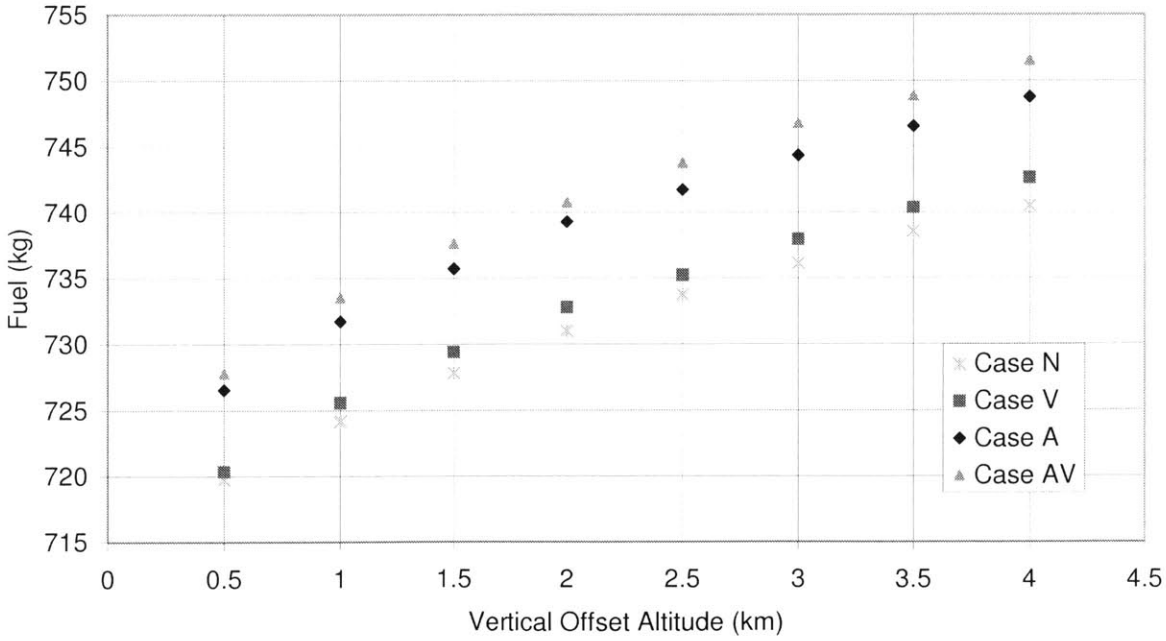

Figure 5-47: Vertical Descent Study Fuel Usage (TMR)

Table 5.9: Fuel and ΔV Usages for Vertical Descent Study

Case	Offset Alt. km	Normalized Cost -	Total Fuel kg	Braking ΔV s	Vertical D. ΔV s	Total ΔV s
N	0.5	-1.078994	719.79	1737.30	44.12	1787.31
	1.0	-1.057288	724.17	1730.06	65.44	1801.39
	1.5	-1.057288	727.85	1725.92	81.63	1813.44
	2.0	-1.057288	731.01	1722.91	95.05	1823.85
	2.5	-1.057288	733.70	1720.12	106.68	1832.70
	3.0	-1.057288	736.15	1717.84	117.00	1840.74
	3.5	-1.060797	738.52	1712.18	130.49	1848.56
	4.0	-1.058947	740.55	1713.78	135.59	1855.27
V	0.5	-1.078333	720.35	1735.22	48.24	1789.35
	1.0	-1.072634	725.56	1736.40	63.50	1805.79
	1.5	-1.068965	729.41	1734.42	78.34	1818.66
	2.0	-1.065541	732.79	1733.47	90.50	1829.86
	2.5	-1.064035	735.24	1730.06	101.88	1837.83
	3.0	-1.061552	737.95	1729.08	111.81	1846.78
	3.5	-1.059211	740.38	1727.99	120.93	1854.81
	4.0	-1.057030	742.65	1727.06	129.41	1862.35
A	0.5	-1.071211	726.55	1756.80	46.24	1808.93
	1.0	-1.057288	731.71	1753.67	66.30	1825.86
	1.5	-1.057288	735.73	1751.80	81.43	1839.12
	2.0	-1.057288	739.30	1750.83	94.22	1850.94
	2.5	-1.057288	741.75	1747.60	105.66	1859.15
	3.0	-1.057288	744.36	1746.07	115.87	1867.83
	3.5	-1.051035	746.57	1743.83	125.29	1875.01
	4.0	-1.048880	748.76	1742.81	134.09	1882.79
AV	0.5	-1.069916	727.79	1762.95	44.01	1812.85
	1.0	-1.064153	733.51	1762.53	63.25	1831.67
	1.5	-1.059989	737.64	1761.10	78.24	1845.23
	2.0	-1.056764	740.79	1757.89	91.89	1855.67
	2.5	-1.053886	743.79	1758.37	101.42	1865.69
	3.0	-1.050781	746.80	1758.41	111.32	1875.62
	3.5	-1.048512	748.86	1756.41	120.41	1882.71
	4.0	-1.046007	751.54	1756.71	128.90	1891.50

Table 5.10: Flight Times and Vertical Velocity for Vertical Descent Study

Case	Offset Alt. km	Coast Duration s	Braking Duration s	Vertical D. Duration s	Total Duration s	Vertical Vel. at Offset Alt. m/s
N	0.5	2722.6	409.0	29.6	3162.5	2.0
	1.0	2717.9	388.3	32.7	3140.2	-14.3
	1.5	2702.0	385.7	38.3	3127.3	-21.3
	2.0	2672.7	366.6	43.5	3084.1	-26.2
	2.5	2728.0	369.8	48.5	3147.7	-29.8
	3.0	2739.2	369.4	53.0	3162.9	-32.8
	3.5	2739.8	368.5	53.1	3162.7	-46.2
	4.0	2810.9	340.5	61.0	3213.8	-38.4
V	0.5	3180.2	404.5	30.5	3616.5	-0.3
	1.0	3193.7	401.3	40.1	3636.4	-0.3
	1.5	3267.8	389.2	49.2	3707.5	-0.3
	2.0	3265.4	389.1	56.6	3712.5	-0.3
	2.5	3266.5	384.0	63.7	3715.5	-0.3
	3.0	3261.3	388.7	69.8	3721.1	-0.3
	3.5	3259.2	388.4	75.5	3724.5	-0.3
	4.0	3241.5	383.6	80.7	3707.2	-0.3
A	0.5	2870.5	377.6	21.1	3270.6	-13.8
	1.0	2851.0	377.1	30.2	3259.6	-19.2
	1.5	2749.8	379.9	37.3	3168.3	-22.6
	2.0	2610.0	369.4	43.3	3024.0	-25.7
	2.5	2861.7	366.3	48.4	3277.6	-28.8
	3.0	2860.9	365.6	53.1	3280.9	-31.4
	3.5	2881.8	344.5	57.4	3285.1	-33.8
	4.0	2898.8	341.9	61.4	3303.4	-36.2
AV	0.5	2678.3	394.7	28.1	3102.4	-0.3
	1.0	2733.9	394.6	39.9	3169.7	-0.3
	1.5	2670.9	390.9	49.1	3112.3	-0.3
	2.0	2774.8	396.7	57.7	3230.5	-0.3
	2.5	2898.8	383.7	63.4	3347.3	-0.3
	3.0	2665.5	389.2	69.5	3125.5	-0.3
	3.5	3169.3	368.0	75.2	3613.8	-0.3
	4.0	2662.7	388.1	80.4	3132.5	-0.3

Variations in the trajectories due to the four constraint scenarios are further investigated by analyzing the altitude vs. downrange, throttle, and thrust direction angle profiles at a given offset altitude. An offset altitude of 2 km was chosen as a representative case because it lies in the middle of the offset altitude parametric range. Altitude vs. downrange profiles for the final braking burn are presented in Figure 5-48, with a zoomed in look at the trajectories at the offset altitude given in Figure 5-49. In Figure 5-48, the case which constrained only the vertical velocity had the shallowest trajectory, while the case which constrained only attitude had the steepest approach to the offset point. In the zoomed in plot, Figure 5-49, both these characteristics remained when the vehicle's reached the 2 km offset point.

The throttle and thrust direction angle histories obtained when targeting to an offset altitude of 2 km with the four different constraint scenarios are seen in Figures 5-50 and 5-51, with the first figure showing constraint scenarios N and V and the second displaying constraint scenarios A and AV. The offset altitude is reached between the times of 350 - 400 s for each case, and in each case a drop to minimum throttle is seen. Therefore, the vehicle follows a vertical free-fall trajectory before maximum throttle is commanded, which is consistent with the vertical descent example given in Section 2.2. The thrust direction angle profiles are consistent with those previously seen, except for Case AV which does not exhibit an initial linear trend.

In conclusion, the addition of a terminal vertical descent phase increased the fuel requirements, but may be a necessity from an operations point of view. Increasing the offset height increases the safety margin, but also increases the fuel used. Adding an attitude constraint at this offset point increases the fuel required by 8.1 kg (26.4 m/s), but has the advantage that the navigational equipment can be used immediately since the vehicle has the correct orientation. This could potentially lower the required offset height. Constraining the vertical velocity results in an increase in time for error correction as the vehicle is descending at a slower rate, which is similar to increasing the offset height in terms of time allotted for altitude and velocity measurements. The fuel penalties due to the attitude and vertical velocity constraints, must be weighed against operational benefits of obtaining site relative measurements or descending at a slower rate.

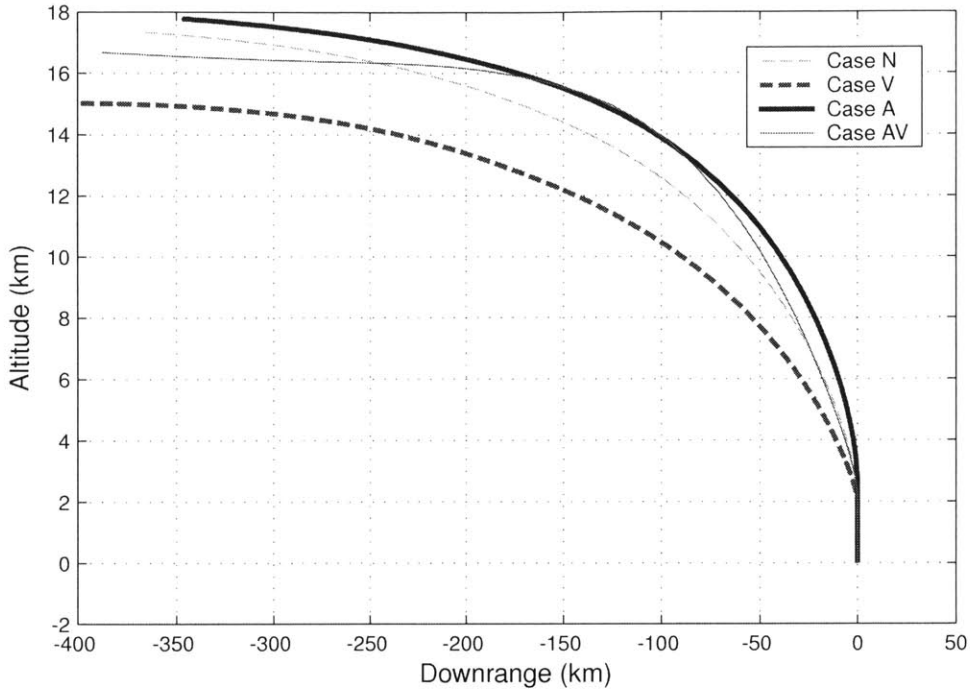

Figure 5-48: Altitude vs. Downrange (during Final Braking Phase) for Cases Targeting 2 km Offset Altitude, (TMR)

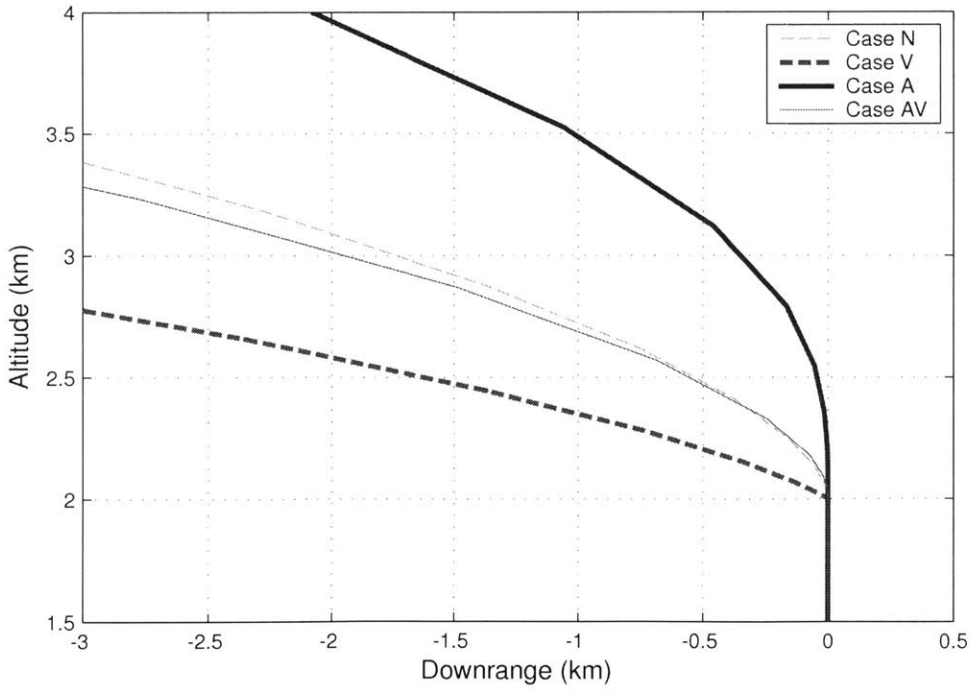

Figure 5-49: Zoomed Altitude vs. Downrange for Cases Targeting 2 km Offset Altitude (TMR)

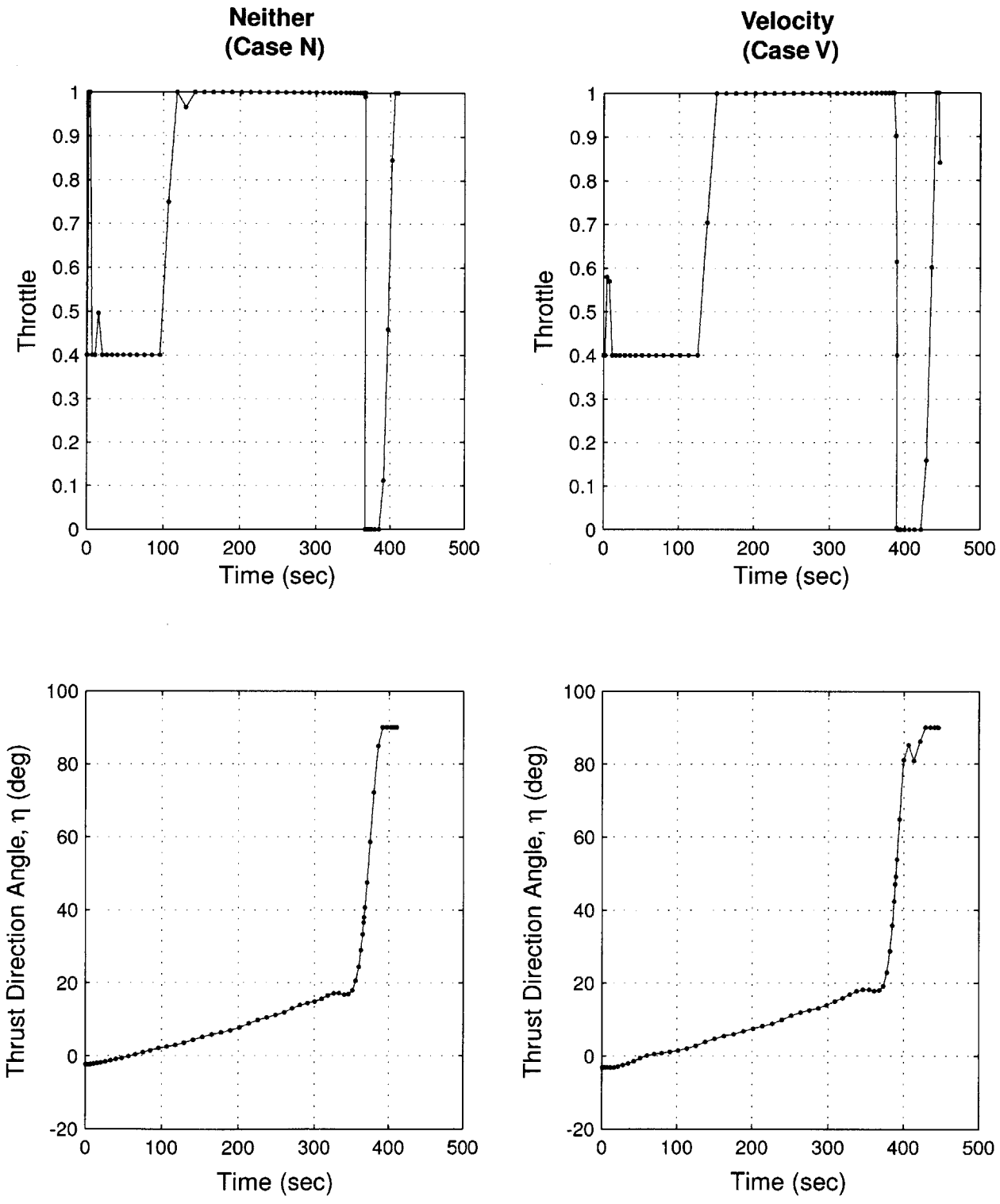

Figure 5-50: Throttle and Thrust Direction Angle, Case N and V (TMR)

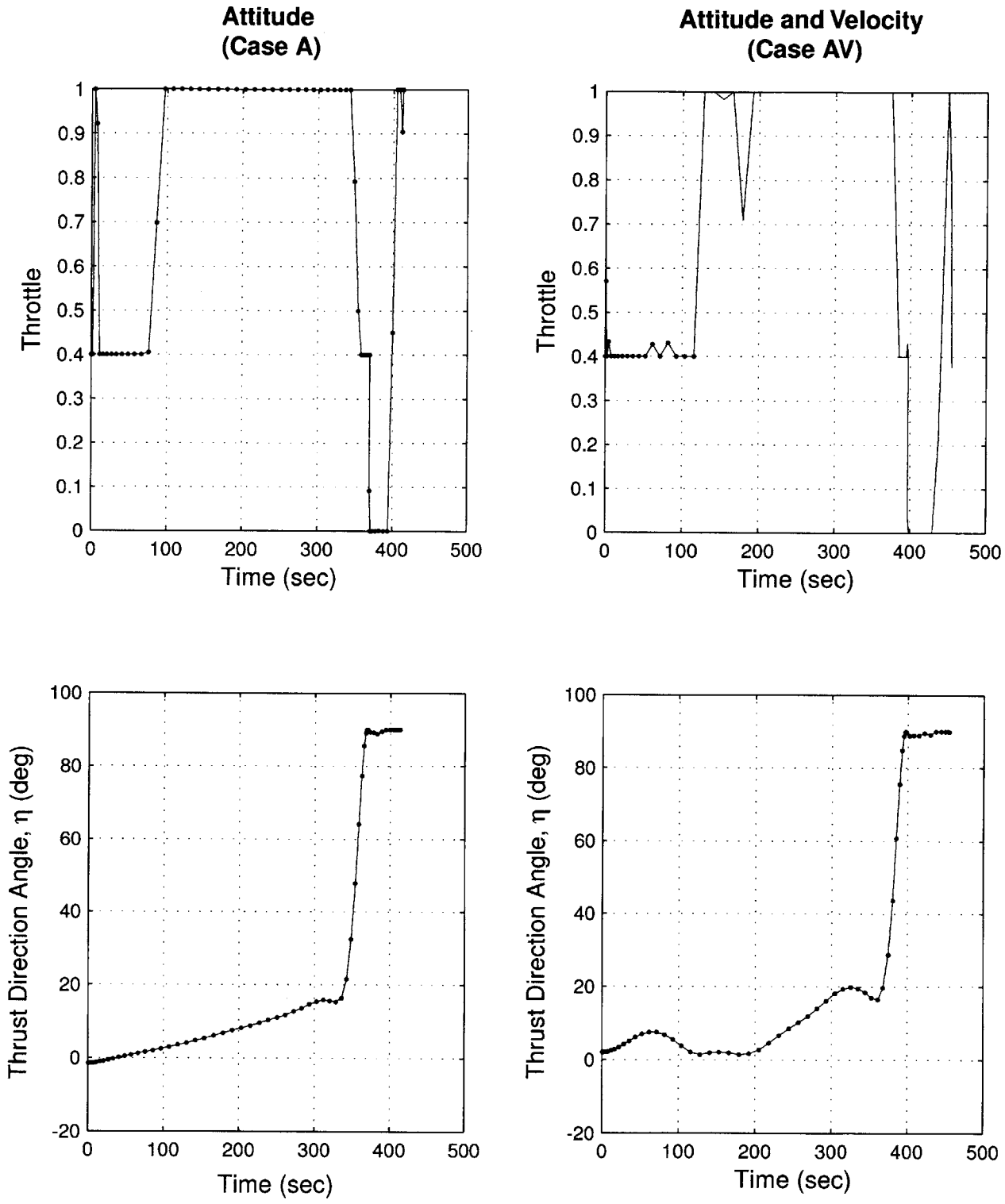

Figure 5-51: Throttle and Thrust Direction Angle, Case A and AV (TMR)

Chapter 6

Conclusion

This chapter summarizes the significant results and conclusions obtained during trajectory optimization analysis of the Moon landing problem. Possible areas for future investigation are also presented.

6.1 Summary of Analysis

A detailed investigation of the constrained trajectory optimization of the Moon landing problem has been presented. Assumptions made include a spherical, homogeneous, and non-rotating Moon, a vehicle with one throttlable fixed main engine with a constant exhaust velocity, and a purely Newtonian gravity model. The trajectory was examined from an initial circular parking orbit of 40 km and descended to a soft-landing on the surface. Constraints were progressively added to mitigate the operationally undesirable characteristics of the obtained solutions. The resulting trajectories were analyzed based on state and control histories, effect on fuel and ΔV usages, operational feasibility, etc..

First, analysis was performed considering only two-dimensional translational motion (TM). The baseline trajectory, which represented a minimally constrained landing trajectory, was found to be operationally infeasible. Operational constraints were imposed to obtain a more viable solution. A parametric study was performed varying the perilune height of the descent orbit and an impulse-like burn was observed in cases that targeted a positive descent orbit perilune height (DOPH). This intermediary burn altered the per-

ilune height to subsurface values prior to the start of the final braking burn. Motivated to preserve a positive perilune height prior to the final braking burn, which provides a passive "failure-to-ignite" abort, the throttle during the braking phase was constrained to be continuous, yet throttlable. The final vehicle attitude and landing approach of the vehicle were found to be very shallow (horizontal), which motivated the inclusion of rotational kinematics in the equations of motion in order to constrain the attitude characteristics of the vehicle.

Attitude kinematics were included in the equations of motion and a constant scaling of the angular acceleration command appended to the cost function in order to minimize the rotational motion of the vehicle during the flight. The vehicle was constrained to land at a near vertical attitude (within 0.5 *deg*) with zero angular rate. This ensured that the vehicle landed in legs-down orientation and would not continue rotate after impact. A parametric study was performed on the DOPH to compare with previously obtained TM fuel usage results. Fuel penalty metrics were obtained for both the terminal attitude and attitude rate constraints, as well as further constraining the throttle to maximum thrust. It was found that the fuel usage increased by further limiting the throttle bound to maximum thrust. During the final portion of the trajectory, the final throttle profile was observed to decrease to a specified lower bound as the vehicle rotated to a vertical orientation, which suggested the optimum was a minimal, or possibly zero, engine thrust during this interval. To investigate this, and to provide for navigational error margin, a terminal vertical descent phase was included in the trajectory. A total of four constraint scenarios were examined, while also perimetrically varying the offset altitude. A linear trend was seen as the offset altitude was increased and variations due to the individual constraints were reported. As a result of this research, viable solutions were obtained that included all of the operational issues considered in this thesis.

6.2 Significant Findings

The conclusions listed below were obtained during the trajectory optimization analysis of a soft landing on the Moon.

1. The minimally constrained fuel optimal trajectory, which included only two-dimensional translational motion directly to the surface, was operationally infeasible due an extremely shallow profile and a skimming of the surface before final touchdown.

2. By further constraining the permissable throttle region during the de-orbit and braking phases, which avoided engine restart failure during the final braking maneuver, fuel usage increased by a range of 0.3 to 5.6 kg, depending on the targeted perilune height. The ΔV differential was also seen to increase with increasing targeted perilune height at a rate of 3.5 $\frac{m/s}{km}$, which is apparent in Figure 5-23.

3. The most efficient method of steepening the landing approach and eliminating skimming of the surface, when including only translational motion, is to constrain the descent orbit perilune height to a positive value. The descent orbit perilune height should set as low as possible, while adhering to safety considerations and accounting for lunar mountainous terrain.

4. The addition of a terminal velocity descent phase increased fuel requirements, but may be a necessity from an operations point of view to account for navigational error. Increasing the offset altitude increased the fuel requirement at a rate of approximately 6 kg/km (ΔV rate of 20 $\frac{m/s}{km}$). Adding a vertical velocity constraint at the offset altitude required an average of 1.8 kg more fuel (5.8 m/s ΔV), as compared to the case where neither the attitude or the vertical velocity were constrained. An attitude constraint added 8.1 kg (ΔV of 26.4 m/s) to either of these cases. The fuel penalties due to the inclusion of attitude and vertical velocity constraints at the offset altitude, must be weighed against operational benefits of obtaining site relative measurements or descending at a slower rate.

5. In all cases that included rotational motion, the thrust direction (pitch) angle during the braking burn remained relatively constant until quickly ramping to vertical, which suggests a 2-phase pitch profile during braking. Also, when rotational motion and a continuous throttle bound was consider, the throttle was found to ride the lower throttle bound while the vehicle righted itself. This suggests that a near-

optimal guidance algorithm would produce a trajectory that pitched the vehicle up to a vertical attitude as late as possible, combined with a significant throttling down of the thrust engine just enough to null gravity (and the residual velocity) as the vehicle prepares for the final landing.

6.3 Recommendations of Future Work

During this research, several topics were identified as possible areas of future work and are given below.

1. The performance impact of certain parameters that were held fixed in this research could be explored. This includes parameters of the initial parking orbit, as well as vehicle thrust-to-weight ratios and engine exhaust velocities.

2. In this thesis, the motion of the vehicle was assumed to be planar. Further exploration into full six degree-of-freedom motion should be taken.

3. Including attitude constraints during intermediate portions of the trajectory (*e.g.*, to ensure correct viewing of the landing site on approach) may be necessary depending on the mission. Including these constraints would be straightforward based on the current setup of the problem.

4. The final landing site was not constrained in this research, which could be an area of further investigation. Determining how the trajectory and control histories change with respect to variations in the desired landing site, at various points along the descent trajectory, would be a useful analysis. This would lead to other important analyses, such as inclined orbits, cross-range capability, divert capability, hazard avoidance, etc.. A study done on the ability/performance impact to correct for dispersions and navigational error could also be performed.

5. In this research, a lower engine throttle limit of 0.4, corresponding to approximately 1.1 lunar g's at the initiation of the final braking burn, was chosen to enforce a continuous braking burn. This constraint generally increased the fuel requirements.

There was insufficient time to explore the implications of using lower bounds, while still preserving a continuous braking burn. An investigation into the effects on the trajectory and performance with respect to these limits would be a useful study.

6. A spike in the throttle profile for the continuous thrust cases at the beginning of the braking burn was a persistent, but unexplained, feature. It is postulated that this spike is commanded to quickly alter the perilune height of the trajectory, but this was not proven. An analysis to explain the effects on the trajectory due to this small impulse-like burn is an additional area of study.

7. In some cases, spikes were introduced into the thrust direction angle when knots were included in the problem, such as seen in Figure 5-14. The reason for this should be examined in more detail. It is believed that the spikes are not features of the optimal solution, but are instead artifacts of the optimization process.

8. Minor inconsistencies seen in the results, which have not been investigated, should be examined. This includes a discontinuity in the ΔV usage trend for the open throttle TM DOPH parametric study in Figure 5-23, as well as the inconsistent thrust direction angle profile of Case AV in Figure 5-51.

9. The propagation errors seen between the DIDO solution and the propagated state was investigated briefly, but an adequate conclusion was not obtained. Future investigation into the propagation error would be a useful study.

10. A procedure was outlined in the example problem of Section 2.2 to further investigated the optimality of the DIDO solution by computing the switching function based on the DIDO estimated costate and the analytically derived Hamiltonian. The implementation of DIDO used in this thesis did not include costate and Hamiltonian information when knots are included in the implementation. All trajectory optimization analysis performed during this research (except for the initial baseline case) included knots and therefore this information was not available. Once this capability has been included, performing this type of analysis for selected critical cases would support the optimality of the obtained results.

[This page intentionally left blank.]

Bibliography

[1] Akridge, C. M. and Harlin, S. H., "Parametric Performance Analysis of Lunar Missions, Part II. Lunar Descent," Tech. Rep. MTP-P&VE-F-63-8, NASA, George C. Marshall Space Flight Center, Huntsville, AL, May 1963.

[2] Cavoti, C. R., "Minimum-Fuel, Two-Impulse, Soft Lunar Landing Orbits," Tech. rep., Space Sciences Laboratory, General Electric Company, September 1966, NASA-CR-65554.

[3] Bennett, F. V. and Price, T. G., "Study of Powered Descent Trajectories for Manned Lunar Landings," Project Apollo Working Paper 1084, NASA Manned Spacecraft Center, Houston, TX, August 1963.

[4] Cheng, R. K., "Surveyor Terminal Guidance," *IFAC Symposium on Automatic Control in the Peaceful Uses of Space*, Stavanger, Norway, 1965, pp. 499–514.

[5] "Surveyor Project Final Report, Part 1. Project Description and Performace," Tech. Rep. JPL-TR-32-1265, NASA, Pasadena, CA, July 1969.

[6] Cherry, G. W., "E Guidance - A General Explicit, Optimizing Guidance Law for Rocket-Propelled Spacecraft," Tech. Rep. R-456, MIT Instrumentation Laboratory, Cambridge, MA, 1964.

[7] Klumpp, A. R., "Apollo Lunar Descent Guidance," *Automatica*, Vol. 10, 1974, pp. 133–146.

[8] Hall, B. A., Dietrich, R. G., and Tiernan, K. E., "A Minimum Fuel Vertical Touchdown Lunar Landing Guidance Technique," *AIAA Guidance and Control Conference*, Cambridge, MA, 1963.

[9] Kriegsman, B. A. and Reiss, M. H., "Terminal Guidance and Control Techniques for Soft Lunar Landings," *ARS Journal*, March 1962.

[10] Ueno, S. and Yamaguchi, Y., "3-Dimensional Near-Minimum Fuel Guidance Law of a Lunar Landing Module," *AIAA Guidance, Navigation, and Control Conference and Exhibit*, Portland, OR, 1999, pp. 248–257, AIAA Paper 99-3983.

[11] Meditch, J. S., "On the Problem of Optimal Thrust Programming for a Lunar Soft Landing," *IEEE Transactions on Automatic Control*, Vol. AC-9, No. 4, 1964, pp. 484.

[12] Teng, L. and Kumar, K. S. P., "Optimum Control for Lunar Soft Landing," *Astronautica Acta*, Vol. 13, No. 5-6, 1968, pp. 545.

[13] Shi, Y. Y. and Eckstein, M. C., "An Exact Solution For Optimum Controlled Soft Lunar Landing," Vol. 16, No. 1, 1971, pp. 18.

[14] Vasile, M. and Floberghagen, R., "Optimal Trajectories for Lunar Landing Missions," *AAS/GSFC International Symposium*, Advances in the Astronautical Sciences, Greenbelt, MD, 1998, pp. 281–295.

[15] Ross, I. M., "How to Find Minimum-Fuel Controllers," *AIAA Guidance, Navigation, and Control Conference and Exhibit*, American Institute of Aeronautics and Astronautics, Inc., Providence, RI, 2004, pp. 1–10, AIAA Paper 2004-5346.

[16] Rea, J. R., *A Legendre Pseudospectral Method for Rapid Optimization of Launch Vehicle Trajectories*, Master's thesis, Massachusetts Institute of Technology, Cambridge, MA, May 2001.

[17] Infeld, S. I., Josselyn, S. B., Murray, W., and Ross, I. M., "Design and Control of Libration Point Spacecraft Formations," *AIAA Guidance, Navigation, and Control Conference and Exhibit*, Providence, RI, 2004, pp. 1–14, AIAA Paper 2004-4786.

[18] Stanton, S. A., *Optimal Orbital Transfer using a Legendre Pseudospectral Method*, Master's thesis, Massachusetts Institute of Technology, 2003.

[19] Ross, I. M., "User's Manual for DIDO (Ver. PR.1β): A MATLAB Application Package for Solving Optimal Control Problems," Technical Report 04-01.0, Naval Postgraduate School, Monterey, CA, February 2004.

[20] Bertsekas, D. P., *Nonlinear Programming: Second Edition*, Athena Scientific, Belmont, MA, 1999.

[21] Hull, D., *Optimal Control Theory for Applications*, Mechanical Engineering Series, Springer-Verlag New York, Inc., New York, NY, 2003.

[22] Bryson, A. and Ho, Y. C., *Applied Optimal Control - Optimization, Estimation and Control*, Hemisphere Publishing Company, 1975.

[23] Ross, I. M. and Fahroo, F., "Legendre Pseudospectral Approximations of Optimal Control Problems," *Lecture Notes in Control and Information Sciences*, Vol. 295, Springer-Verlag, Berlin Heidelberg, 2003.

[24] Betts, J. T., "Survey of Numerical Methods for Trajectory Optimization," *Journal of Guidance, Control, and Dynamics*, Vol. 21, No. 2, 1998, pp. 193.

[25] Kirk, D. E., *Optimal Control Theory - An Introduction*, Prentice-Hall Networks Series, Prentice-Hall, Inc., Englewood Cliffs, NJ, 1970.

[26] *The Astronomical Almanac: 2004*, Nautical Almanac Office, Washington, DC, 2004.

[27] Battin, R., *An Introduction to the Mathematics and Methods of Astrodynamics*, AIAA Education Series, American Institute of Aeronautics and Astronautics, Reston, VA, 1987.

[28] Orloff, R. W., *Apollo by the Numbers: A Statistical Reference*, NASA History Series, NASA History Division, Office of Policy and Plans, NASA Headquarters, Washington, D.C., 2000.

[29] Ellion, M. E., DiCristina, H., Maffei, A. R., and Briglio, A., "Development of the Surveyor Vernier Propulsion System (VPS)," *AIAA Second Propulsion Joint Specialist Conference*, Colorado Springs, CO, 1966.

[30] Wertz, J. R., *Spacecraft Attitude Determination and Control*, Kluewer Academic Publishers, Dordrecht, Boston, London, 1978.

[31] Gill, P. E., Murray, W., and Saunders, M. A., *User's Guide for Snopt Version 6, A Fortran Package for Large-Scale Nonlinear Programming*, Systems Optimization Laboratory, Stanford University, CA, December 2002.

[32] "Surveyor I Mission Report, Part 1. Mission Description and Performance," Tech. Rep. JPL-TR-32-1023, NASA, Pasadena, CA, August 1966.